Title

THE ROLE OF MICROSTRUCTURAL INHOMOGENEITIES ON HIGH TEMPERATURE FAILURE IN CERAMICS

Author

Johnson, S.M.

Publication Date

1982-09-01

LBL-14588

Lawrence Berkeley Laboratory
UNIVERSITY OF CALIFORNIA

Materials & Molecular
Research Division

THE ROLE OF MICROSTRUCTURAL INHOMOGENEITIES ON HIGH TEMPERATURE FAILURE IN CERAMICS

Sylvia M. Johnson
(Ph.D. Thesis)

September 1982

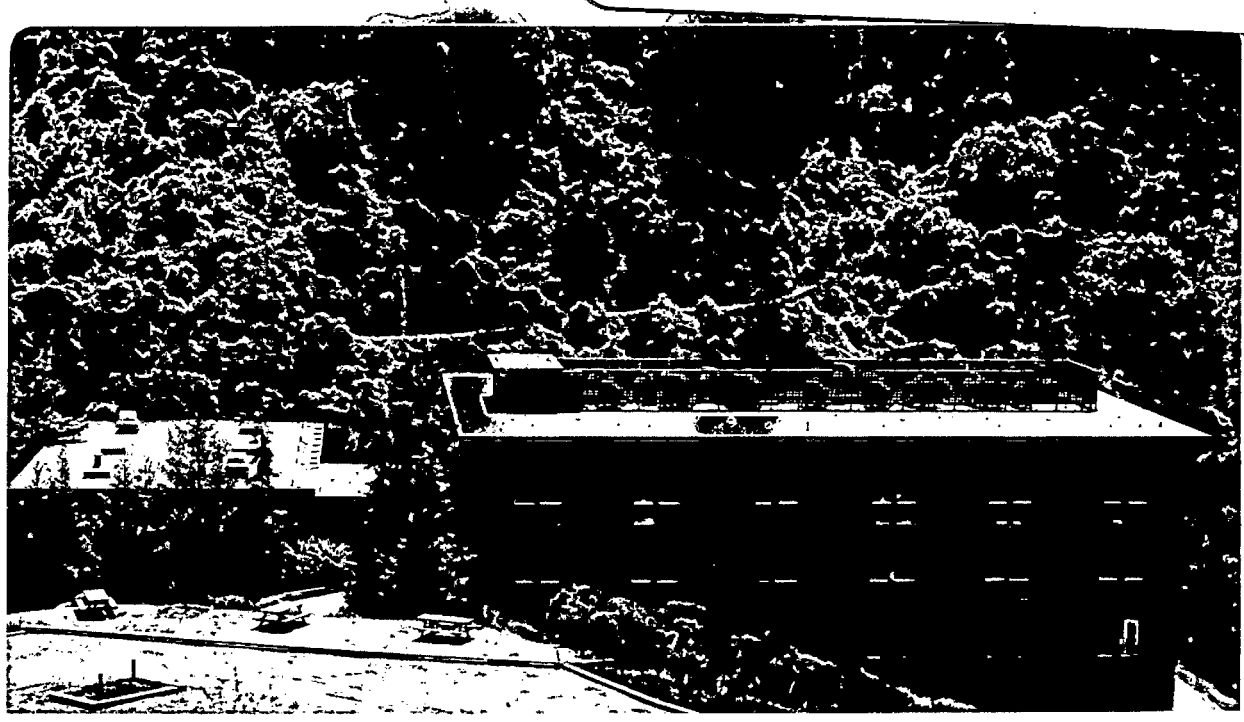

Prepared for the U.S. Department of Energy under Contract DE-AC03-76SF00098

DISCLAIMER

LBL-14588

THE ROLE OF MICROSTRUCTURAL INHOMOGENEITIES ON HIGH TEMPERATURE FAILURE IN CERAMICS

Sylvia M. Johnson

(Ph.D. Thesis)

Materials and Molecular Research Division
Lawrence Berkeley Laboratory
University of California
Berkeley, California 94720

September 1982

This work was supported by the Director, Office of Energy Research, Office of Basic Energy Sciences, Materials Science Division of the U.S. Department of Energy under Contract No. DE-AC03-76SF00098.

TABLE OF CONTENTS

THE ROLE OF MICROSTRUCTURAL INHOMOGENEITIES
ON HIGH TEMPERATURE FAILURE IN CERAMICS

Sylvia M. Johnson

Ph.D

Department of Materials
Science and Mineral Engineering

.....
A. G. Evans
Chairman of Committee

ABSTRACT

Inhomogeneous regions such as zones of atypical grain size, poorly sintered areas and inclusions have been observed to be crack initiation sites and thus failure origins. An analysis of the stresses associated with microstructurally inhomogeneous regions in a creeping ceramic polycrystal indicates that the stress within such regions and in the peripheral matrix is enhanced by a factor of two.

Creep rupture experiments performed on a fine grained (1 - 3 μm) alumina indicated that the failure time, t_f, is proportional to the applied stress, σ_∞, as $t_f \propto \sigma_\infty^{-5}$. The experimental data can be most easily reconciled with crack propagation models. Cavity morphology was observed by the use of high resolution scanning electron microscopy and was found to be dependent on the applied stress. Triple point cavities predominated at high stresses, many closely spaced arrays of two grain boundary cavities predominated at intermediate stresses, and more widely spaced arrays at low stresses.

Calculated cavity nucleation stresses are higher than the applied stess, even when locally enhanced by inhomogeneities, and it is

postulated that grain boundary sliding transients at wavy grain boundaries may enhance local stresses to the level of the critical nucleation stress.

1. INTRODUCTION

The role of ceramics in increasing the energy efficiency of many processes is expanding; greater economy can be realized at high temperatures and thus ceramics are ideally suited for these applications. The high temperature properties of ceramics and their associated advantages over metals are thus particularly important.

The creep rates of metals, their relatively low melting temperatures and corrosion susceptibilities preclude their use in very high temperature operations. Although ceramics are corrosion resistant and have high melting temperatures, they are subject to creep deformation and rupture at high temperatures. Thus the understanding of creep processes and failure in ceramics is of great importance. Alumina constitutes a good material for such studies; it has high strength, toughness, hardness, is readily available and may be sintered or hot pressed to near theoretical density without a liquid phase which is extremely detrimental to high temperature properties. Typical fracture stress behavior as a function of temperature is summarized as follows. The failure stress is virtually independent of temperature up to $T/T_m \sim 0.5$ (T_m is the melting temperature in Kelvin). In this regime, fracture is brittle and usually originates from pre-existing flaws, such as surface cracks (caused by surface finishing) or large voids and inclusions (introduced during processing).[1] At elevated temperatures the fracture stress decreases and is accompanied by creep deformation and, in materials of uniform microstructure, initiates in zones characterized by a low dihedral angle or a low surface diffusivity.[2] The preceeding description of high temperature behavior is based on theoretical work by Hsueh and Evans.[2] Cavities have been

observed to form preferentially in certain areas[2] in materials of uniform microstructure and although theory and experiment have not yet been fully correlated, the work of Hsueh and Evans[2] which ascribes cavitation susceptibility to locally low values of Ψ and D_s is the best explanation available.

The purpose of the present study is to investigate, more comprehensively than previous studies, the failure origins and the cavitation process in alumina with primary emphasis on inhomogeneous areas and microstructural defects. The first part of the study comprises the initial observation of defects (in particular, zones of large grains, poorly sintered areas and inclusions in uniform matrices of fine grain size) and an experimental determination of failure time/stress relationships. A subsequent high resolution scanning electron microscopy study of various aspects of the failure process and a theoretical stress analysis of the inhomogeneities was necessary to understand the processes involved.

2. PREVIOUS INVESTIGATIONS OF CAVITATION AND CREEP MECHANISMS

2.1 General Considerations

Creep in ceramics takes place by diffusional processes (dislocation creep is discounted for this class of materials);[3] the diffusion path can be either through the lattice (Nabarro[4]-Herring[5] creep) or along the grain boundaries (Coble[6] creep). Diffusional creep must necessarily be accompanied by grain boundary sliding.[7,8,9] Cannon et al.[10] observed that in Al_2O_3 diffusional creep dominates over the temperature range 1200-1750° and at stresses up to 310 MPa.

Raj and Ashby[11] treated a creeping polycrystal as having a Newtonian viscosity, η, where the shear strain rate is given by

$$\dot{\gamma} = \tau_a/\eta \tag{2.1}$$

where τ_a is the applied shear stress. The viscosity can be expressed as

$$\eta_v = \frac{1}{42} \frac{d^2 kT}{D_v \Omega} \tag{2.2a}$$

for volume diffusion and as

$$\eta_b = \frac{1}{132} \frac{d^3 kT}{\delta D_b \Omega_b} \tag{2.2b}$$

for grain boundary diffusion, where d is the grain size, Ω is the atomic volume, D_v and D_b are diffusion coefficients and δ_b is the grain boundary width. Diffusion coefficients for volume, surface and boundary diffusion during sintering of Al_2O_3 have been determined by Dynys et al.[12] A more general expression for D_b has been developed by Cannon and Coble.[13]

2.2 Microstructural Defects

Prior analyses of stress perturbations related to grain size and shape differences[11,14-16] have been restricted to grain arrays consisting of equiaxed[9,12] or elongated grains,[9] equispaced grains of different size[13] and bimodal grain size distributions[14] and cannot be applied to isolated zones.* A method of analyzing the stresses associated with inhomogeneous zones in a linearly elastic material has been developed by Eshelby.[19] The Eshelby method consists of cutting out the inclusion and allowing it to transform freely under the influence of the applied stress. Surface tractions can then be applied to return the transformed zone to its original size and shape whence it is replaced in the matrix. Equal and opposite forces then develop in the surrounding matrix. The method can be applied to linearly viscous materials by recognizing the analogous roles of the shear modulus, μ_m, in linear elasticity and the viscosity, η, in linearly viscous circumstances.

2.3 Cavitation

2.3.1 Cavity Nucleation

Cavities in metals are usually associated with grain boundary particles[20,21] where dihedral angles are sufficiently small to allow nucleation at low stress levels.[22] Grain boundary particles are not observed in ceramics to the same extent as in metals. Grain boundary particles were not observed in the present aluminas by TEM.[23]

---

* Defect-initiated fracture in silicon nitride at room temperature[17] has been studied. Evans et al.[18] have studied the effect of cavities on fracture of ceramics.

Classical heterogeneous nucleation theory has been used by a number of authors[21,22] to describe the nucleation of cavities at grain boundaries. Classical nucleation theory is presumed to apply and the analysis in this work is based on that presumption.

In the nucleation of cavities by a classical process[21,22] it is necessary to form a vacancy cluster of a critical size (which may be of the order of 50 Å).[21] The time taken for vacancy clusters to reach the critical size for viable cavity nuclei is known as the "incubation time".[21] The cavity nucleation rate increases during this time and reaches a steady state at the end of the incubation period. The origin of the delay in reaching steady state nucleation is the time taken for vacancy diffusion. The incubation time is therefore dependent on the size of the nuclei or the number of vacancies which must gather, and the diffusion rate. The net vacancy flux is[8]

$$J_v \simeq \frac{2D}{L\Omega} \sinh\left[\frac{\Omega\sigma}{kT}\right] \qquad (2.3)$$

where L is the mean distance through which vacancies must migrate and D is the diffusion coefficient. The incubation time, which is directly related to the vacancy flux, is dependent on temperature, stress, grain size and diffusion coefficient. Furthermore, the stress dominates the incubation time such that incubation can be effectively characterized by a critical incubation stress. Raj[21] has found the incubation time in a number of materials to vary from a few seconds to many hours.

The thermodynamic barrier to cavity nucleation is related to the change in Gibb's free energy caused by the creation of new surface area for the cavity, the loss of grain boundary area which is consumed

by the cavity and the work done in creating the new volume occupied by the cavity. The volume of the critical-sized cavity is dependent on the nucleation site and the dihedral angle, Ψ, which determine the cavity shape and therefore the nucleation stress. Specifically, sites with lower values of dihedral angle, and therefore smaller volumes for critical size nuclei, such as particles, experience preferential cavity nucleation. For constant dihedral angle the lower grain boundary energy (for particle/grain interfaces) and difference in grain boundary area lost and surface area gained (cavities at three or four grain boundaries consume more grain boundary area, and create less surface area than two grain interface cavities) means that the critical nucleation stress is lowest for cavities formed at particles, followed by cavities at triple points, with two grain interface cavities having the highest nucleation stresses. The nucleation stress in Al_2O_3 as functions of cavity type and dihedral angle are shown in Fig. 2.1.[22] The critical stresses for typical cavity sites and dihedral angles in Al_2O_3 are much greater than the stresses commonly applied during creep tests. Therefore either the cavity nucleation stress must be reduced, or the applied stress enhanced in some manner to allow cavity nucleation in the present experiments. Grain boundary sliding, which has been observed to accompany cavity nucleation in metals,[24-26] is presented as one possible source of local stress enhancement in the present work. Cavity nucleation in metals has been observed to be associated with grain boundary sliding by a number of workers.[24-26]

2.3.2 Cavity Morphology, Occurrence and Growth

Cavities in ceramics may occur at three or four grain corners[2,22,27] or in arrays on two grain boundaries.[14] During creep, failure occurs by the growth and coalescence of cavities.[22,27-29] Cavities initially grow in "quasi-equilibrium" shapes which eventually become crack-like as the cavities grow.[30,32] Chuang et al.[31] and Pharr and Nix[32] both modelled the change in cavity morphology. Both surface diffusion and grain boundary diffusion must be included in models which describe the transition in cavity shapes. The Pharr and Nix [32] model is a modification of a model presented by Chuang and Rice[30] in which the growth of crack-like cavities by surface diffusion was treated. The shape change from equilibrium to crack-like was allowed by the development of a 'nose' or elongation of the equilibrium cavity.

Hsueh and Evans[2] extended the analyses to consider the effect on local variation in dihedral angles, and surface diffusivities. Hsueh and Evans[2] developed refined expressions for the cavity growth rates for both cavity morphologies. Analysis of the transition from equilibrium to crack-like shape indicated that Ψ and D_s were the important parameters in determining the transition. The crack-like cavity growth rate increases with cavity size and thus failure occurs prematurely from regions with locally reduced values of Ψ and D_s, which cause the transition to occur at lower values of a/b. As previously discussed, lower values of Ψ lead to increased cavitation susceptibility.

The Hsueh and Evans[2] model contains one major difference from the Pharr and Nix model.[32] Grain boundary diffusion is assumed to be

rapid in the Pharr and Nix model and thus only surface diffusion was deemed to be important. The Hsueh and Evans[2] model takes into account the ratio between the surface and grain boundary diffusivities, $\Delta = \frac{D_s \delta_s}{D_b \delta_b}$. The smaller the value of Δ, i.e., the lower the surface diffusivity, the sooner the transition will occur. As the cavity volume increases so does the surface area. Eventually, surface diffusion cannot manage to distribute the vacancies removed from the grain boundary by the boundary diffusion over the surface rapidly enough and the cavity elongates.

Many analyses have been based on the assumption that growth occurs freely, i.e., that there are no constraints on the system and that the growth rate is unaffected by the presence of other cavities. Dyson[36] introduced the concept of constraint to take into account the effect of the number and distribution of other cavities on growth rates. A constrained situation is one in which a cavitated grain boundary is isolated in uncavitated material. In order for the cavities on the grain boundary to grow at the calculated rates, it is necessary for the adjoining grains to deform to accommodate the increase in volume. If the boundaries are uncavitated and are not free to slide the necessary extent, then the cavity growth cannot be accommodated, and the growth rate must necessarily decrease. An unconstrained situation arises when many grain boundaries are cavitated, or the grain boundaries can slide freely. Inhomogeneous distributions of cavities result in a constraint being imposed on the cavitated area. The constrained area need not necessarily be one isolated grain boundary; larger zones with a high cavitation

susceptibility may be constrained by the surrounding less rapidly creeping matrix despite the zone being highly cavitated.

2.4 Stress-Strain Rate-Failure Time Relationships

The growth of grain boundary and triple point cavities in metals and ceramics has been modelled by numerous workers[28,29,31,35,37,45,47] with varying results. Growth models generally try to predict the dependence of the growth rate, v, on the stress σ or on the stress intensity factor K. The results are usually expressed in the form $v \propto \sigma^n$ or $v/v_{min} \propto (K/K_{th})^n$ where v_{min} is the velocity at the threshold stress intensity factor K_{th}. At $K < K_{th}$ cracks do not grow. The exponent 'n' is the most important factor, and it is here that the models differ. The exponent n is only valid at $K \gg K_{th}$; at $K \sim K_{th}$ the v-K curve is asymptotic and n may assume large values.

The prediction of failure time as a function of stress is an alternative method to determining v-K curves. Failure time predictions are, of course, the most practically useful and the most easily correlated with experimental results as is done in the present study. Failure may be controlled either by crack nucleation or by crack propagation. Crack propagation occurs by the coalescence of cavities ahead of a crack, thus extending it; crack nucleation occurs by the coalescence of cavities to form a crack. If failure is crack propagation controlled, i.e., if crack nucleation is fast and the majority of the time to failure can be accounted for by crack growth then it would be expected that failure times will be inversely proportional to growth rates and that the failure times may be expressed as $t_f \propto 1/\sigma^n$ where the exponent 'n' will have the same value as predicted by the v-K or v-σ models. Failure or rupture times for crack

nucleation models may still be expressed as a function of stress although care must be taken in assigning the value of the exponent n. Crack nucleation models can still be based on cavity growth rates as cavities must grow and coalesce to form a crack. Models which consider coalescence of cavities on one boundary to form a full facet cavity or crack are essentially crack nucleation models and failure times based on cavity growth rates for these circumstances will have a value of n related to that for cavity growth.

The models result in varying values of the exponent depending upon the various assumptions made concerning cavity morphology, distribution, growth mechanisms, i.e., the relative importance of surface and grain boundary diffusion and material parameters. Certain models, particularly those which assume plastic deformation or a power law component of creep are really only applicable to metals as are those which require creep to proceed by dislocation movement.

None of the models proposed fits the experimental results generated in this study. The value of n determined in the present work is ~5. Some studies take simplified cases which do not adequately describe the observations. Many models have assumed a fully unconstrained situation, i.e, the occurrence of many cracks and cavities on neighboring boundaries. Models which treat isolated cavitated boundaries or cracks often make other assumptions regarding the crack or cavity shape which do not reflect the general case. None of the models incorporate all the features necessary to describe the present work. The various models, their assumptions and applicability to the present study will be discussed according to the value of the exponent predicted.

The earliest work in this field was performed by Hull and Rimmer.[14] The model is based on a square array of spherical cavities situated on the grain boundary of a bicrystal which is subjected to a normally applied tensile stress. In this, and in many models, the grains are assumed to be rigid or to show linearly elastic behavior. The cavity growth rate was found to be linearly dependent on stress. As only one grain boundary is considered, this model can be viewed as a crack nucleation model and the failure time is the time taken for cavity coalescence and thus $t_f \propto 1/\sigma$.

Numerous authors[29,31,43,44] have obtained an exponent equal to 1; the common assumption is that cavities are of equilibrium or quasi-equilibrium shapes. It should be noted that this situation is presented only as a limiting case in later theories. Surface diffusion is assumed to be rapid and non-rate limiting in these models and grain boundary diffusion is thus the important parameter in determining growth rates.

Raj et al.[43] have presented a corrected expression for the growth rate of an array of lenticular or equilibrium cavities. The assumptions are similar to the Hull and Rimmer[14] model although the effect of an internal gas pressure in the cavities is included. As the model only considers one grain boundary, the coalescence of the cavities can be assumed to constitute crack nucleation, and the fracture time derived is inversely linearly dependent on the stress (if the internal gas pressure is taken as zero), i.e., $t_f \propto 1/\sigma_\infty$. The cavity growth rate can also be expressed as $v \propto \sigma_\infty$.

Chuang et al.[31] have also presented expressions for the limiting case of quasi-equilibrium growth. The growth rate expression is

dependent only on D_b and not on D_s and is linearly dependent on σ_∞. Again, the failure time can be derived from the growth rate expression if the coalescence of cavities on a facet is considered and $t_f \propto 1/\sigma_\infty$. This expression only holds when $\Delta = D_s \delta_s / D_b \delta_b$ is large, i.e., grain boundary diffusion is rate controlling, and is thus only applicable to growth of equilibrium cavities.

Takasugi and Vitek[44] also considered cavity growth controlled by grain boundary diffusion and obtained similar results for equilibrium cavities, i.e., $v \propto \sigma_\infty$. It was noted in this model that the velocity reached a steady state value as a result of interaction of neighboring cavities, i.e., the diffusional fluxes interact to cause a constant rate of material deposition between the cavities.

The above theories could all be classed as crack nucleation models. A crack propagation model involving the growth of equilibrium cavities ahead of a crack has been developed by Wilkinson.[29] The exponent is still one, i.e., $v \propto K$ where v is the crack velocity in this case. The v-K dependence is the same whether or not the number of equilibrium cavities ahead of the crack is constant. If all cavity nucleation is assumed to have occurred simultaneously and early, then the model can be used to predict the time for a crack to advance across one facet. This time, t_N is $\propto 1/K$ or $\propto 1/\sigma_\infty$. The failure time will thus be some multiple of this t_N and thus $t_f \propto 1/\sigma_\infty$.

A common factor in all the models which give a value of n=1 is the cavity shape assumed. No experimental results fit these models as cavities do not retain an equilibrium shape and thus models which require such a shape will underestimate cavity and crack growth rates and over-estimate failure times. The reason for the value of n being

one is that growth is only dependent on grain boundary diffusion (and geometrical factors) which is linearly dependent on stress. Some of the n=1 models[29,44] assume a constant rate of material deposition between the cavities. This may be correct for small cavities; however as the cavities grow the ligament size decreases and the cavity morphology changes (i.e., less material per unit extension is removed) and the rate of material deposition does not remain constant. This situation was taken into account by Hsueh and Evans.[2]

Models which include the contribution of the cavity nucleation stress (i.e., the formation of new cavities increases the growth rate) to the growth rate involving equilibrium cavities result in a stress exponent of 2. Raj and Baik[38] present a model in which new cavities nucleate at the far end of the damage zone ahead of the crack tip. The crack propagates by growth of the cavity ahead of the crack to coalesce with the crack. Wilkinson[29] obtained a similar expression. Both of these models allow cavity nucleation to occur at grain boundary particles, a situation not applicable to the present case. The extra stress dependence comes directly as a result of the nucleation of new cavities. These models are not applicable as they assume equilibrium cavity shapes and nucleation as a result of the crack growth. The present study indicates that all the cavities nucleate simultaneously early in the creep process and not at grain boundary particles.

While cavities may initially assume an equilibrium shape, they eventually become crack-like. Surface diffusion becomes important in crack-like cavity growth and the ratio Δ is important in determining the morphology transition.[2,30,31] Chuang and Rice[30] analyzed the case

of growth controlled by surface diffusion, a model later modified by Pharr and Nix.[32] If grain boundary diffusion is assumed to be fast and only surface diffusion is important then the value of the exponent obtained is 3. The above are both crack nucleation models as fracture is assumed to occur when the cavities coalesce. The failure time is thus $\propto \sigma^{-3}$. Similar approaches by Miller and Pilkington[28] and Wilkinson[29] based on these models but extended to crack propagation by cavity coalescence also result in an exponent of 3, i.e., $v \propto K^3$. The failure time according to this model should also be inversely proportional to K^3. Chuang et al.[31] also obtain a σ^{-3} dependence of the rupture time if only surface diffusion is considered although this relationship only applies for small values of Δ, i.e., $\delta_s D_s \ll \delta_b D_b$.

The above models which give an exponent of 3 all assume that surface diffusion is rate controlling, i.e., the opposite case to the n=1 models. Chuang et al.[31] have taken the ratio Δ into account in determining the limiting crack-like velocity of certain void shapes with the result that $v \propto \sigma^{3/2}$. Wilkinson[29] obtains a similar expression by assuming that the surface curvature at the tip of the crack is not an important parameter. However, as a cavity or crack becomes more crack-like the radius of curvature at the tip decreases and thus becomes important.

As noted previously, cavity morphology changes and thus growth only in a crack-like mode does not adequately describe actual conditions. The Chuang et al.[31] model describes the transition between the two morphologies. However, this is based on stress relaxation times for the surface diffusion which indicate that surface diffusion is the dominant cavity growth mechanism. These relaxation times are obtained

from data for metals; the model is strictly only applicable to diffusive cavity growth in metals.

Vitek's[40] crack growth model, in which $v \propto K^4$, is not applicable to the present case as crack growth by cavity coalescence is not considered. Also, the crack is considered to maintain a constant thickness regardless of stress which is not accurate and the void tip shape is not completely described.

Chuang[39] has developed a model describing crack growth by a coupled surface diffusion and grain boundary diffusion process. The crack is a cavity which has assumed a long crack like shape and which is not influenced by neighboring cavities. The velocity is assumed to reach a steady state value. A universal v-K relationship is derived with an exponent which varies from 12 to ∞. This model only describes a limiting case; there is no interaction with other cavities and there is no allowance for change in cavity morphology. As this model only describes part of the failure process, a failure time relationship cannot be obtained from it. The model is applies to a bicrystal and not to a polycrystal; the effects of degree of constraint are not considered. It is also assumed that the grains may undergo large elastic distortions, a situation unlikely in a polycrystal. It is interesting to note that a third power dependence of the velocity on the stress at the crack tip, σ_{tip}, arises as one of the boundary conditions at the crack tip and the equation does not contain the grain boundary diffusion parameter.

The presence of a possible constraint arising from inhomogeneous nucleation is not considered in the above models. A crack nucleation model which includes failure time expressions for both constrained and

unconstrained growth has been developed by Rice.[37] The situation is similar to that previously discussed in which an array of equilibrium cavities is growing. The failure time in unconstrained circumstances is

$$t_f \propto b^3/\sigma_\infty$$

where b is the cavity spacing in accord with previous theories. Only grain boundary diffusion terms are important in the unconstrained case. The failure time in constrained circumstances is expressed in terms of the Monkman-Grant product $t_f\dot{\varepsilon}_\infty$ where $\dot{\varepsilon}_\infty$ is the applied strain rate. Monkman and Grant[47] derived an empirical relationship indicating that $t_f\dot{\varepsilon}_\infty$ is constant for many materials. The constrained Rice equation is

$$\dot{\varepsilon}_\infty t_f \propto b/d \qquad (2.4)$$

where d is the grain size. The rupture time under constrained circumstances is much greater than the unconstrained time, particularly at small stresses. However, again the above only models the growth of equilibrium cavities.

To summarize the above models: - an exponent of 1 is obtained for equilibrium cavities where grain boundary diffusion is limiting, an exponent of 2 is obtained when the effect of the nucleation of new cavities is added, an exponent of 3 is obtained for crack-like cavity growth when only surface diffusion is important, and an exponent of 12 is obtained for the coupled grain boundary and surface diffusion growth of an isolated crack-like cavity. Other exponents have been obtained for crack growth not by cavity coalescence (n=4) and for cavity growth in metals by models which do not apply to ceramics.

None of the models describes the observed behavior because all models really only present limiting cases and make assumptions which are too restrictive. The effect of constraint has not been included in crack-like growth models. Failure time predictions need to take into account the change in growth rate experienced by a cavity of changing morphology.

Experimental data for ceramics are scarce. The experimental evaluation of the exponent n for SiC and Al_2O_3 fibers gives values of 3-6.[22] Sintered SiC yields an exponent of ~50 when failure is crack propagation controlled.[51] The exponent obtained in the present work is 5.

3. EXPERIMENTAL METHOD

3.1 Material

Two nominally identical dense high purity aluminas* were used for this study. The aluminas contained 0.25% MgO and had grain sizes of 1-3 μm. The materials were hot pressed in vacuum to near theoretical density in graphite dies. Material #1 was uniformly black while material #2 was light grey. The color is probably a result of non-stoichiometry in the alumina. Similar color changes in other aluminas have been observed by the author. Most tests were performed on material #2.

3.2 Sample Preparation

Three point bend bars approximately 31 mm by 3.2 mm x 3.2 mm were cut from the as received billet. The faces were ground by means of a surface grinder to achieve the final dimensions and parallel faces. Final polishing** of one face was conducted using a 15 μm diamond wheel and 6 and 1 μm diamond paste. The long edges of the polished face were bevelled using a 6 μm diamond wheel in order to remove corner cracks. The samples were measured to ±0.005 mm after polishing.

3.3 Sample Mounting

The samples were mounted on sapphire rods (0.175 mm diameter) on a Lucalox three point bend holder using epoxy resin (see Fig. 3.1).

---

* AVCO Corp.
** Pedepin, Struers, OH

The polished face became the tensile face. The span length was 25 mm. A Lucalox disc was attached to the middle rod to provide a contact area for the rams.

3.4 Test Equipment

A floor model Instron* with a controlled cross head displacement rate was used for the creep tests. The large grain creep resistant alumina rams were water cooled at top and bottom.

An air furnace capable of attaining 1600°C by means of molybdenum disilicide elements was placed around the test apparatus. The temperature was measured using at Pt6%Rh-Pt30%Rh thermocouple and could be measured to ±2°C. The temperature variation during a test was $\leq$ ±1°C. A schematic drawing of the testing apparatus is shown in Fig. 3.1.

3.5 Test Method

The testing machine was calibrated using a strain gauge. The sample holder assembly was then placed between the rams and an initial load of ~4.5 N was applied. The purpose of the preload was to allow the sample holder assembly to remain intact when the epoxy dissociated at ~300°C. The furnace was gradually heated to ~500-600°C and then heated more rapidly up to the test temperature (usually 1350°C). An automatic load control was used to maintain the preload by balancing the thermal expansion of the system. The temperature was allowed to

---

* Instron, Canton, MA

equilibrate for 45 mins at the test temperature. The preload was reduced to 2-2.5 N during this time. Before testing began the preload was removed.

The tests were conducted using a constant displacement rate and the variation in load with time was recorded. Most tests were continued to failure which was signaled by a sudden drop in the load. Interrupted tests were performed by reducing the load after the required time and cooling under a load of 4-5 N, maintained in the same manner as the preload. This load was applied to inhibit sintering of the creep damage. The furnace was cooled at 1°C/sec until the temperature was below 1000°C, and was then allowed to cool more rapidly.

Bars used for interrupted tests were remounted and tested in the same way after microscopic examination.

3.6 Microscopy

3.6.1 Sample Preparation

The fracture surfaces were inspected in an optical microscope to determine obvious visible causes of fracture. The fractured ends of the bars were then cut to a length of 5 mm to facilitate SEM inspection, using an Isomet saw.† The samples were then thoroughly cleaned in acetone and alcohol in an ultrasonic cleaner.

The samples were gold coated* for 1-1/2 - 2 mins. Care was needed at this stage to ensure that a fine, uniform coating was achieved. It was therefore necessary to vary the coating times. The

† Buehler, IL
* Polaron

gold coating is also subject to deterioration and some samples needed to be recoated (gold coatings may be partially removed using Micro† (~2%) solution). Usually one fracture surface and one tensile surface of each sample pair were coated.

3.2.6 Scanning Electron Microscopy

Three different scanning electron microscopes were used.†† High resolution SEM was performed on the ISI microscope which has a resolution of ~30 Å in the upper stage and ~60 Å in the lower stage. Conventional resolutions were achieved on an AMR instrument equipped with an analytical X-ray unit.* Samples were examined mainly on the ISI and AMR microscopes. Both the tensile and fracture surfaces were studied.

3.6.3 Auger and Secondary Ion Mass Spectroscopy

A scanning microprobe** was used to investigate various inhomogeneous regions. It was necessary to lightly carbon coat the samples to prevent charging. Gold coating was not successful because the gold Auger peaks overlap with silicon peaks, precluding the possibility of identifying glassy areas. Standards of as-received alumina, sapphire and Lucalox were also subjected to Auger analysis. Additionally, SIMS*** was used to identify light elements.

---

† Micro, Industrial Products
†† ISI DS 130, AMR 1000, JEOL
* KEVEX, CA
** SAM, Physical Electronics, Inc., CA
*** SIMS, Physical Electronics, Inc., CA

4. RESULTS

4.1 Creep Rupture Tests

4.1.1 General Considerations

The load was determined as a function of time for four different displacement rates. A typical creep rupture curve is shown in Fig. 4.1. A primary creep regime, in which load increases rapidly with time, is followed by a short secondary creep regime and an extended tertiary creep regime in which a slow decrease in applied load occurs with time. Cavity and crack nucleation and propagation occur during this period. Castastrophic failure eventually occurs at the failure load, P_f, and time t_f. The peak load, $\hat{P}$, which occurs in the secondary creep regime, is the maximum load applied to the sample. At low displacement rates, ($\dot{D}$= 6.35 x 10^{-6}, 1.60 x 10^{-5} m/s), $P_f < \hat{P}$. At higher displacement rates ($\dot{D}$= 3.18 x 10^{-5}, 6.35 x 10^{-5} m/s) there is no tertiary creep and $\hat{P} = P_f$.

For a three point bend test configuration, the peak stress $\hat{\sigma}$ can be related to the applied peak load, $\hat{P}$ by[27]

$$\hat{\sigma} = \frac{(2n + 1)\, L\hat{P}}{2nbh^2} \qquad (4.1)$$

where L is the span length, b is the specimen width, h is the specimen height, and n is the steady state creep exponent. The value of n for material #1 was determined by Blumenthal[27] as 1.7 for comparable displacement rates and temperatures. The deflection, D, of a beam is given by[52]

$$D = \frac{PL^3}{4bh^3E} \qquad (4.2)$$

where E is Young's modulus. Hence, the strain rate, $\dot{\varepsilon}$, can be derived from Eqns. (4.1) and (4.2) as

$$\dot{\varepsilon} = \frac{L(2n + 1)}{nL^2} h\dot{D} \qquad (4.3)$$

Creep tests were performed at four displacement rates: 6.35×10^{-6} (series A), 1.60×10^{-5} (series B), 3.18×10^{-5} (series C) and 6.35×10^{-5} (series D) m/s. Most tests were performed on material #2 (see Section 3.1) at 1350°C. Table 4.1 details the various test conditions and results.

4.1.2 Stress-Strain Rate-Failure Time Relationships

The experimental failure time data are plotted as a function of peak stress in Fig. 4.2. The data suggest a stress exponent, n, of 5, i.e., $t_f \propto \sigma^{-5}$. Possible explanations for the observed stress exponent will be discussed in Section 6. Another conventional method of expressing the data is given in Fig. 4.3 where the dimensionless failure time (or Monkman-Grant product) $t_f \dot{\varepsilon}_\infty$, is shown as a function of peak stress. Again, the relationship is nonlinear. Some of the low values of $t_f \dot{\varepsilon}_\infty$ signify premature failure, which can be traced to microstructural defects at the origins of failure. (Section 4.2). For example, an inclusion was located at the fracture origin of sample EE (Fig. 4.4), which exhibited premature failure.

4.2 Microstructural Defects

Various microstructural defects were observed on both the fracture and tensile surfaces. The two aluminas exhibited different inhomogeneous regions.

The major defects in alumina #1 were zones of abnormal grain size. Some examples are shown in Figs. 4.5 and 4.6. Typically, these

large grained zones are spherical with a diameter of 80-100 μm. The grain size is at least ten times that of the matrix (i.e., the grain size ratio $\zeta = d_p/d_m$ is 10). In a number of instances voids were observed at the centers of the zones (Fig. 4.5). Quantitative X-ray analysis revealed no compositional differences between the zones of large grains and the matrix. At best, the sensitivity of such methods is ± 1%. A zone of large grains was observed to be the source of failure in at least one instance (Fig. 4.5). Matching large grain regions were found on both fracture surfaces, indicating that cracks propagated through the zones. No estimate has been made of the frequency of occurrence of these zones, but they were observed on most alumina #1 fracture samples. Subsequent investigation by Blumenthal[41] has also revealed the presence of many such zones on tensile surfaces.

Many poorly sintered areas and voids were observed in material #2. Figure 4.7 shows these regions on a tensile surface. Similar areas were also observed as planar zones, orthogonal to the hot pressing direction (Fig. 4.8). Holes or missing grains were often associated with these areas (Fig. 4.9A). A more substantial void, possibly the result of an inclusion, is shown in Fig. 4.9B. Small cracks can be seen radiating from this particular defect. Further discussion of the cracks emanating from, and passing through, these regions will be presented in Section 6.

Areas which contain a second, amorphous phase were observed in a number of cases. Figure 4.10 shows one such area, containing holes. Figure 4.11 shows another area, this time associated with a region of large grains wherein the remains of a glassy phase, in the form of ligaments, can be identified. Crack-like surface defects were present

in one sample (Figs. 4.12, 4.13); while an internal void, or unsintered surface was detected (Fig. 4.14) and an inclusion (Fig. 14.14) was present at the fracture origin of another sample.

4.3 Fracture Origins and Crack Growth

Failures typically originated from the subsurface and could be identified by the appearance of radial lines (Fig. 4.15). These lines are due to surface roughness associated with the zone of damage initiation and propagation. Areas through which cracks have propagated rapidly tend to be relatively smooth.

Fracture origins are not always readily visible on the fracture surface. Crack nucleation and growth can often be better observed on the tensile surface. Although the critical cracks (those which caused failure) cannot be observed, subcritical cracks and defects in various stages of growth can be identified near the fracture surface.

Cracks are observed to nucleate at various defects. Some examples of cracks which are nucleated from the crack-like defects discussed in Section 4.2 are depicted in Figs. 4.12 and 4.13. The cracks emanate both from the ends of the defect and from intermediate locations (Fig. 4.13). These cracks are very large and the damage associated with them also extends over a large area, with many grain boundaries in the vicinity of the main crack being completely cavitated.

Further examples of crack nucleation and propagation from defects were obtained in samples subjected to interrupted creep tests in which creep was stopped after five minutes at $D = 1.60 \times 10^{-5}$ m/s, and the sample examined. The sample was caused to creep for a further five minutes, 30% of the failure time in order to observe the growth of

cracks. Cracks were only observed to nucleate in the vicinity of unsintered areas. Cracks can be seen initiating from and within these areas in Figs. 4.16. The poorly sintered areas extend diagonally across the tensile surface and thus the cracks do not follow these areas but extend into the matrix prependicular to the direction of maximum stress. The theoretical basis for the effect of defects on crack nucleation is discussed in Section 5. Figure 4.6 shows the extent of crack growth during the first creep period.

Upon further deformation the cracks exhibited appreciable extension (Figs. 4.17 and 4.18). The damage is more extensive after the second creep period, (cf. Figs. 4.16 and 4.17) although the cracks are still associated with microstructural defects. Figure 4.19 shows a crack nucleated in the matrix at the poles of a spherical inhomogeneity while Fig. 4.20 shows a crack which has nucleated within a spherical inhomogeneity. The failure origin in this case could not be detected on the fracture surface; examination of the tensile surface, however, revealed a probable failure origin (Figs. 4.20A and B). Other interrupted tests displayed similar crack nucleation and propagation behavior.

A crack system which does not appear to be associated with a defect is shown in Fig. 4.21; however, a subsurface defect may, of course, be present. The extent of damage and crack branching around the crack tip can be clearly seen.

The preceeding examples in this section are all from samples in Series B. Extensive but more uniform damage was observed at a lower strain rate (Fig. 4.22A). No large cracks were present, but a network of small cracks covered much of the tensile surface near the fracture

surface. Coalescence of small cracks can also be discerned. Cracking was also observed at the higher strain rates.

4.4 Cavitation

Cavities at either three grain junctions or at two grain interfaces were observed in all samples. Two grain boundary cavities tend to form in arrays, with equilibrium initial shapes. Such an array in a large grained region is shown in Fig. 4.23. Cavities with crack-like shapes are also occasionally observed (Fig. 4.24). At low strain rates (Fig. 4.25) two grain boundary cavities were observed, although the cavity spacing is larger than that in higher strain rate samples. A number of highly cavitated grain boundaries can be seen in Fig. 4.26 from which it is apparent that grain facet size is not important in determining cavitation suseptibility. The cavity density varies between faces of the same grain and Fig. 4.27 is an example; many grain faces with similar orientations to the principal stress were observed to have differing cavity densities. The cavities eventually coalese leaving ligaments (Figs. 4.28) which then fracture. Grain boundary cavities can also be observed on the sides of cracks when viewed from the tensile surface (Figs. 4.29).

At high strain rates the cavity spacing decreases and lines of cavities tend to form (Fig. 4.30). An approximate measure of average cavity spacings on two grain interfaces is plotted in Fig. 4.31. The scatter can be ascribed to grain orientation effects. The cavity spacing, b, is approximately inversely proportional to stress. Triple point cavities increase in importance at high strain rates, eventually predominating at the highest strain rate (Fig. 4.37). The general trends in cavitation behavior are summarized in Fig. 4.33.

Cavities start to form early in the creep process, as evidenced by an interrupted test in which the specimen was broken at room temperature after ~30-50% of its expected life (Fig. 4.34).

A low spatial density of cavities appears in the compressive region of the fracture surfaces of each test specimen (Fig. 4.35). Similarly, two grain boundary cavities were not observed in low stress regions of the samples, i.e., at the ends (Fig. 4.36), confirming that the cavities are stress induced and are not produced as a direct result of the heat treatment.

Grain boundary sliding was generally observed to accompany creep deformation (Fig. 4.37). Surface ledges formed by grain boundary sliding are apparent in Fig. 4.37B.

4.5 Auger and SIMS

The peak ratio, Al:O was measured in various samples and positions, but was found to be inconclusive in determining the cause of the color change shown in Fig. 4.38. Silicon was detected in a glassy area. The color of the samples is thought to be either a result of non-stoichiometric Al_2O_3 or diffused carbon. Auger analysis was not sensitive enough to determine an Al:O ratio difference between white and gray areas. It was not possible to test for varying carbon contents.

5. STRESS ANALYSIS

5.1 Method of Solution

The material subjected to stress at elevated temperatures is considered to be deforming by diffusive creep as dislocation creep is discounted for this class of materials.[1] The viscosity of inhomeogeneous regions differ from that of the matrix. Such regions may be regarded as zones of high or low viscosity. As an example, viscosity exhibits a strong dependence on the grain size, increasing as the grain size increases. Thus, large grained zones are regions of high viscosity embedded in a less viscous matrix as shown schematically in Fig. 5.1. An enhanced tension can be expected to develop within a high viscosity region, as manifested in the analogous elastic problem of an inclusion of high shear stiffness contained in a compliant matrix.[19] In fact, the stress analysis is conducted by first obtaining the stress distribution for an elastic inclusion in an elastic matrix and then applying the correlation between linearly viscous and linearly elastic solids. The stresses within the inhomogeneity and within the surrounding matrix can then be calculated.

5.2 Stresses Within the Inhomogeneity

The stresses that developed within an elastic inclusion of ellipsoidal symmetry are spatially uniform and for constant volume deformation, i.e., Poisson's ratio, $\nu = 1/2$, can be obtained from Eshelby[19] as;

$$P_1^p = \sigma_\infty \left[\frac{\mu_m + 4\mu_p}{3\mu_m + 2\mu_p} \right],$$

$$P_2^p = P_3^p = \sigma_\infty \left[\frac{\mu_m - \mu_p}{3\mu_m + 2\mu_p} \right], \qquad (5.1a)$$

where $P^{p}_{1,2,3}$, are the principal tensile stresses (Fig. 5.1), μ is the shear modulus, σ_∞ is the remote stress and the superscripts p and m refer to the particle and matrix, respectively. This solution is rigorously applicable when $\mu_p > \mu_m$. For $\mu_p < \mu_m$, the direct application of the Eshelby analysis does not allow $P_1^P \to 0$ as $\mu_p \to 0$ (i.e., for a hole), when $\nu = 1/2$, because the transformation strain $e^T \to \infty$ as $\mu_p \to 0$. A working result for small μ_p/μ_m can thus be obtained by setting $\nu \approx 0.49$; for this choice of ν, the desired limit $P_1^P \to 0$ as $\mu_p \to 0$ obtains, as given by;

$$P_1^P = \frac{\sigma_\infty}{3}\left[\frac{2\,\mu_p}{0.6\,\mu_m + 0.4\,\mu_p}\right] + \left(\frac{\mu_m}{\mu_p + 0.025\,\mu_m}\right)] \qquad (5.1b)$$

The stresses within a linearly viscous solid can be determined from Eq. (5.1) by invoking the direct equivalence between the shear modulus μ and the viscosity, η (for stress controlled boundary conditions). The stresses thus become, for example,

$$P_1^P = \sigma_\infty \left[\frac{\eta_m + 4\,\eta_p}{3\eta_m + 2\eta_p}\right], \eta_p > \eta_m \,. \qquad (5.2)$$

As a specific example, the particular form of the stresses within a zone of atypical grain size can be derived. The magnitude of the viscosity in this case depends upon the operative modes of diffusive deformation. In general, for coupled grain boundary and lattice diffusion;

$$\eta = \frac{d^3 kT}{42\Omega(dD_v + \pi\delta D_b)} \,, \qquad (5.3)$$

where D_v is the lattice diffusivity, δD_b is the boundary diffusivity, d is the grain size and Ω is the atomic volume. Hence, replacing μ in Eq. (5.1) by η from Eq. (5.3), the stresses become (for $\zeta > 1$);

$$P_1^P = \sigma_\infty \left[\frac{4\zeta^3 D_c + 1}{3 + 2\zeta^3 D_c} \right] ,$$

$$P_2^P = P_3^P = \sigma_\infty \left[\frac{1 - \zeta^3 D_c}{3 + 2\zeta^3 D_c} \right] . \qquad (5.4a)$$

and (for $\zeta < 1$);

$$P_1^P \approx \frac{\sigma_\infty}{3} \left[\left(\frac{2\zeta^3 D_c}{0.6 + 0.4\zeta^3 D_c} \right) + \left(\frac{\zeta^3 D_c}{0.025 + \zeta^3 D_c} \right) \right] , \qquad (5.4b)$$

where,

$$D_c = \left[\left(d_m D_v + \pi\rho D_b \right) / \left(\zeta d_m D_v + \pi\rho D_b \right) \right] \text{ and } \zeta = d_p / d_m .$$

The dependence of the maximum principal stress, P_1^P, on the grain size ratio*, ζ, is shown in Fig. 5.2 for $d_m D_v \ll \zeta D_b$ (typical of fine grained ceramics) such that $D_c = 1$. The stress varies rapidly with grain size ratio for $0 < \zeta < 2$, attains an approxiately constant level ($P_1^P \approx 2\sigma_\infty$) when $\zeta > 5$, and becomes zero when $\zeta = 0$. It should be noted that the internal stresses are position independent, i.e., uniform throughout the inclusion.

5.3 The Matrix Stresses

The position dependent matrix stresses can also be determined from the Eshelby solution and converted into the equivalent results for a linearly viscous solid. The stress outside an ellipsoidal inhomogeneity in a linearly viscous solid can be derived directly from Eshelby[19] as (for $\eta_p > \eta_m$)

---

* The grain size ratio is equivalent to viscosity and thus Fig. 5.2 is general and applicable to all inclusions of varying viscosities.

$$'P_{il} = (1 + 2B/5)\ 'P^A_{il} - B\ ('P^A_{ik}\ n_k\ n_l + 'P^A_{lk} n_k\ n_l) + 2B'P^A_{jk} n_j n_k n_i n_l \tag{5.5a}$$

where

$$B = \frac{n_p - \eta_m}{(\eta_m - \eta_p)\beta - \eta_m} \text{ and } \beta = \frac{2}{15}\frac{4 - 5\nu}{1 - \nu},$$

and,

$$p = p^A - (3B/2)'P^A_{ij} n_i n_j \tag{5.5b}$$

where,

$$'P_{ij} = P_{ij} - (1/3)\ p\ \delta_{ij} \tag{5.6}$$

where $P_{ij}{}^A$ is the applied stress, δ_{ij} is the Kronecker delta and n_{ij} is the direction cosine. For a uniaxially applied tension, σ_∞:

$$'P^A_{11} = 2\sigma_\infty/3\ ,$$

$$'P^A_{22} = 'P^A_{33} = \sigma_\infty/3 \tag{5.7}$$

and $$'P^A_{12} = 'P^A_{33} = 0\ ,$$

and for a spherical zone:

$$n_1 = \cos\theta,\ n_2 = \sin\theta \text{ and } n_3 = 0\ ,$$

when θ is the orientation with respect to the applied stress. Hence,

$$p = \sigma_\infty \left[1 - B(3\cos^2\theta - 1) \right]$$

$$'P_{11} = (2\sigma_\infty/3) \left\{ 1 + B \left[(2/5 - (3/4)\sin^2 2\theta) \right] \right\}$$

$$'P_{22} = -(\sigma_\infty/3) \left\{ 1 + 2B \left[(1/5) - (3/4)\sin^2 2\theta \right] \right\} \qquad (5.8)$$

$$'P_{33} = -(\sigma_\infty\ 3)\ (1 + 2B/5)$$

$$'P_{12} = (\sigma_\infty/2)\ B \sin 2\theta\ (1-2\sin^2\theta)$$

$$'P_{13} = 0\ .$$

The combined relations for stresses (Eq. 5.8) permit the determination of the three orthogonal stresses,

$$P_{11} = \sigma_\infty \left\{1 + B \left[(3/5) - \cos^2\theta\ (3-2\cos^2\theta) \right]\right\}$$

$$P_{22} = \sigma_\infty B \left[(1/5) + \cos^2\theta\ (2\sin^2\theta - 1) \right] \qquad (5.9)$$

$$P_{33} = -(\sigma_\infty/3)\ (1 + 2B/5)\ .$$

Using the relationship,[53]

$$P_{1,2} = \frac{P_{11} + P_{22}}{2} \pm \sqrt{\frac{(P_{11}-P_{22})^2}{2} + p_{12}^2} \qquad (5.10)$$

the principal stresses are then given by;

$$p_1^m = (\sigma_\infty/2) \left[1 + 2B\ (2/5-\cos^2\theta) + \left\{ [1 + B(2/5) - \sin^2 2\theta\ ]^2 \right.\right.$$

$$\left.\left. - B^2 \sin^2 2\theta\ (1-2\sin^2\theta)^2 \right\}^{1/2} \right] \qquad (5.11)$$

$$p_2^m = (\sigma_\infty/2) \left[1 + 2B(2/5-\cos^2\theta) - \left\{ 1 + B\ (2/5-\sin^2 2\theta\ (1-2\sin^2\theta)^2 \right\}^{1/2} \right]$$

$$p_3^m = \sigma_\infty\ B \left[1/5 - \cos^2\theta \right]$$

The peripheral matrix stress for the case of a hole or very low viscosity ($\eta_p << \eta_m$) inclusion can be obtained from the Eshelby solution (eqn. 5.5) by including an extra term,

$$- \frac{1 - 2\nu}{3(1 - \nu)} A \, p^A (n_i n_i - 1/3 \, \delta_{il})$$

where

$$A = \frac{K_p - K_m}{(K_m - K_p)\alpha - K} ,$$

K is the bulk elastic constant and $\alpha = 1/3 \ (1 + \nu)/ \ (1 - \nu)$. Allowing $K_p \to 0$, then $\left((1-2\nu)/3(1-\nu)\right) A \to 1/2$. Setting B = 5/3, the principal stresses are

$$p^m_{1,2} = \frac{\sigma_\infty}{3} \{ [5 \sin^2\theta - 7/4] \pm [[7/4 + \sin^2\theta (3/2 + 5 \cos^2\theta)]^2 + [25 \cos^2\theta \sin^2\theta (\cos^2\theta - 13/20)^2)] \} \qquad (5.12)$$

$$p^m_3 = \sigma_\infty \ [1/2 - 5/3 \cos^2\theta]$$

This result can also be obtained from the Eshelby solution for a spherical cavity. The variation in the magnitude of the stresses, over one quadrant of the zone surface, is plotted in Figs. 5.3 and 5.4 for both large and small values of η_p. For large η_p (or, for a large value of ζ), the tensile stress maximum occurs around the poles* so that $p_1^m \approx 2\sigma_\infty$; whereas for small η_p, the tensile stress exhibits a maximum at the equator, but again $p_1^m \approx 2 \sigma_\infty$. The principal matrix

---

* Note that the maximum principal tensile stress does not occur at the poles ($\theta = 0$) when $\nu = 1/2$, but at $\theta = \pi /6$; a result that is not widely appreciated. It should also be noted that a state of hydrostatic tension exists at the poles.

stresses, P_1^m and P_2^m for the case of a hole do not act together; p_1^m is zero from $\theta = 0 \rightarrow \pi/5$ and P_2^m is zero from $\theta = \pi/5 \rightarrow \pi/2$.

The relationships between grain size and the matrix stresses can be obtained from the above using,

$$B = 5 \left[\frac{1 - \zeta^3}{3 + 2\zeta^3} \right] . \qquad (5.13)$$

6. DISCUSSION

6.1 Cavity Formation

Examination of the fracture surfaces in Section 4.4 indicates that the type and spacing of cavities formed during the creep process may depend on one or both of two factors: stress and time. The predominant cavity morphology as a function of applied stress is shown in Fig. 4.33. At high strain rates (and therefore high stresses (~200 MPa) and short failure times (~1 - 30 s)) triple point cavities predominate and very few arrays of two grain boundary cavities are observed. Under these conditions, where two grain boundary cavities exist, they are small and closely spaced (Fig. 4.30). With decreasing stresses (failure times from ~400-1000 s) arrays of two grain boundary cavities are more commonly observed and the cavity spacing increases with increase in failure time.

The variety of cavity forms observed and their apparent dependence on the applied stress (and possibly on failure time) can be addressed by first considering the cavity nucleation stresses. Standard nucleation theory predicts that a critical stress is necessary for cavity nucleation. The critical nucleation stress for cavities on two grain interfaces exceeds that for cavitation at three or four grain corners and to an extent is dependent on the dihedral angle, Ψ (Fig. 2.1) Specifically, at 1623 K and for dihedral angles 90°-120°, the critical stress for two grain boundary cavities in Al_2O_3 range from ~600 to 1650 MPa; whereas, for four grain corner cavities the critical stresses range from ~0 for Ψ = 70° to 1580 MPa for Ψ = 120°. These critical stresses compare with applied stresses in the present experiments ranging between 100 and 300 MPa. Hence the

applied stresses are only large enough to nucleate cavities at four grain corners with small Ψ ($< 90°$, at least, in accord with standard nucleation concepts). Nucleation on two grain interfaces is thus most probably associated with either an enhanced local stress or a locally reduced critical stress.

Very small local dihedral angles can cause an appreciable reduction in the critical nucleation stress. Grain boundary located inclusions have small dihedral angles and may constitute sites for preferential nucleation. Grain boundary inclusions or precipitates and their associated cavities have often been observed in metals. However, no grain boundary particles have been detected in the present alumina using high resolution TEM.[23] This source of critical stress reduction can thus be discounted in this instance.

Stress enhancement associated with an inhomogeneous area or microstructural defect has been discussed in Section 5. It is sufficient to note that the maximum possible stress enhancement is approximately a factor of two. This increased stress occurs within the vicinity of inclusions of either high or low viscosity. The formation of cracks at defects has been observed (Figs. 4.16 - 18). and is discussed in greater detail in Section 4.3. A stress enhancement factor of 2 is still insufficient to satisfy the nucleation stress requirements for the observed two grain boundary cavities.

A second source of stress enhancement may be grain boundary sliding. Grain boundary sliding and creep are simultaneous and complementary processes. Evidence of grain boundary sliding can be seen in Fig. 4.37. One grain in Fig. 4.37B has experienced out of plane sliding and ledges can be observed along one edge. Steady state

grain boundary sliding exerts no significant influence on the local stress. However, if sliding occurs intermittently, then a considerable tensile stress normal to the sliding boundary may develop. Alternate grain boundary sliding and migration, with accompanying grain boundary waviness, has been observed in metals.[54,55] All grain boundaries are in fact wavy although of widely differing wavelength.

In a sliding transient, the applied shear stress τ_∞ (as dictated by the applied tensile load) initially prevails at the boundary, but the stress relaxes with time during sliding to ~0. These shear stresses are the only stresses that exist along straight boundaries. However, a wavy boundary subject to transient sliding at a local shear stress τ, develops normal tensile and compressive stresses (Fig. 6.11) of magnitude

$$\sigma_n = \pm 2\ \tau\lambda/\eta h \qquad (6.1)$$

where λ is the wavelength and h is the amplitude. Equating σ_n to the critical nucleation stress gives

$$\lambda_c = \pi\sigma_c h/2\tau \qquad (6.2)$$

where λ_c is the critical wavelength (of a small amplitude boundary) that must be exceeded if the normal stress is to attain the nucleation stress during the sliding transient. When the transient is complete the normal stress reduces to

$$\sigma_n = \frac{kT\dot{u}}{4\Omega}\ D_v[1 + \pi D_b\delta_b/\lambda]$$

where $\dot{u}$ is the steady state grain boundary sliding rate. In contrast to Eq. (6.1), small amplitude waviness will, in this instance, result in small sliding related normal stresses.

If this mode of cavity nucleation prevails the cavity spacing should be of the order of the dominant wavelength of the grain boundary. A wavy boundary in a two grain boundary cavitated specimen but within a large grained region, can be seen in Fig. 4.24. The wavelength in fine grained areas is small and difficult to discern. It is also noted from Eq. (6.1) that the critical wavelength (and hence the cavity spacing) is inversely related to the stress, in approximate accord with present observations (Fig. 4.31).

Not all grain boundaries cavitate, because grain boundaries are not invevitably subjected to the transient sliding described above. In order that transient sliding can occur, favorable orientations of the adjacent grains, e.g., a low angle boundary containing glissile dislocations* must be assumed. Grains have been observed to rotate during creep to assume such positions. Grain rotation is necessary for this theory. However, grain rotation under constrained circumstances is poorly understood and is an area which requires further research. A possible time dependent cavity nucleation process may be associated with such grain boundary structure changes. Consequently, the time required for a significant number of grains to become realigned may exceed the failure times at high strain rates, thus preventing the full scale nucleation of two grain boundary cavities. Some grain boundaries will experience sliding immediately, thus accounting for the few arrays of cavities in high strain rate samples.

---

* Facetting has been observed on low angle grain boundaries.[57] Such boundaries therefore fulfill the waviness condition required for nucleation.

6.2 Crack Nucleation, Propagation and Failure

The growth of cavities has been discussed by Hsueh and Evans.[2] Initially, equilibrium shaped cavities form (Fig. 4.24) and eventually become crack-like (Fig. 4.25). Coalescence of cavities results in a full facet cavity or cracked grain boundary.

Failure time is composed of the crack nucleation time and the crack propagation time; one of these may be dominant. The interrupted creep experiments (Figs. 4.16-18) indicate that the major portion of failure time can be attributed to crack propagation.

Cracks should form in cavity-prone areas, or areas of locally enhanced stress. Possible causes of stress enhancement have been discussed in Sections 5 and 6.1. It is predicted in Section 5 that cracks should form either in the matrix, at the poles of high viscosity inclusions and the equator of low viscosity inclusions, or within high viscosity inclusions.

Cracks through, and near, microstructural defects were observed; in fact, the vast majority of cracks are associated with such areas (Figs. 4.16-19). Cracks can also nucleate within the matrix remote from a defect (Fig. 4.21) in an area which cavitates preferentially. Hsueh and Evans[2] predicted that areas with low values of dihedral angle, Ψ , or low surface diffusivity, D_s, would cavitate preferentially and that subsequent cavity growth is accelerated as the transition to crack-like growth occurs at smaller values of the cavity size to spacing ratio. Blumenthal[27] observed inhomogeneous cavitation in alumina #1 with a uniform microstructure.

Cracks tend to propagate by the coalescence of cavities on a grain boundary ahead of the crack which results in a decohered

boundary and thus crack extension. Cavities on both sides of cracked boundaries can be seen in Fig. 4.29.

Upon reaching a certain critical size a crack propagates rapidly, and failure occurs almost instantaneously. Subsurface failure origins in Figs. 4.14 and 4.15 show roughly circular regions with radial ridges indicating the area of slow crack growth and the critical crack size.

Examples of failure origins are shown in Section 4.3. The failure origins that could be identified were microstructural defects, indicating that these defects do indeed exert a prominent influence on premature failure.

6.3 Stress-Strain Rate-Failure Time Relationships

The various methods of predicting failure times are based on either crack nucleation or crack propagation concepts. Comparison of predicted failure times obtained from a number of sources with observed failure times permits invaluable insights into the possible origins of the stress exponent ($n \approx 5$) and reveals parameters which relate uniquely to failure time predictions.

Rice[37] has developed constrained and unconstrained expressions for crack nucleation times when crack nucleation is assumed to be coincident with full facet cavity formation. The unconstrained time is given by;

$$t_n = \frac{16b^3 F(f_i) h(\Psi)}{315 D_1 \sigma_\infty} \qquad (6.4)$$

where $D_1 = D_b \delta_b \Omega / kT$, f is the fraction of grain boundary area cavitated, f_i is the initial cavitated area, and

$$F(f_i) = \left[1 - \frac{105}{16} f_i^{3/2} \ln(1/f_i) - \frac{1}{8} f_i^{3/2} \left(63 f_i^{1/2} - \frac{175}{4} - \frac{45}{4} f_i \right) \right.$$

and $h(\Psi) \sim 0.6$. Substituting the observed cavity spacing-stress relationship, $b \propto \sigma_\infty^{-1}$, yields

$$t_n \propto \sigma_\infty^{-4} \tag{6.5}$$

The stress exponent of Eq. (6.5) is thus similar to the observed stress dependence of the failure time. However, the specific crack nucleation times predicted from Eq. (6.5) are appreciably less than the observed failure times. This result is consistent with the observation that crack nucleation occurs well before final failure.

The equivalent constrained crack nucleation time is given by,

$$\dot{\varepsilon}_\infty t_n \approx (4h/3\alpha)\ (b/d)\ (1 - f_i^{3/2}) \tag{6.6}$$

where α is a constant ($\alpha = 2/\pi$ for a linearly viscous material). This expression yields crack nucleation times much greater than the observed failure times. It is thus concluded that the material cannot be experiencing fully constrained cavitation. Many grain boundaries, Fig. 4.26, are observed to be cavitated, indicating that cavitation has occurred under relatively unconstrained conditions.

As the nucleation based predictions appear inadequate, failure times based on crack propagation demand investigation. A preliminary investigation by Blumenthal[41] of crack growth in the current alumina yields a growth rate

$$\frac{v}{v_o} \propto \left(\frac{K}{K_c}\right)^5 \tag{6.7}$$

where v_o is the crack velocity at $K = K_c$, the critical stress intensity factor. The crack propagation time is derived from Eq. (6.7) as:

$$t_p = \frac{2a_i^{-3/2}}{3v_o} \frac{K_c^5}{\sigma_\infty Y} \qquad (6.9)$$

where a_i is the initial crack size and Y is a geometrical factor $\sim 2.24\sqrt{\pi}$ for a surface crack. The prediction is very sensitive to a_i and v_o, and reasonable choices of $a_i = 20\,\mu m$ taken as a typical defect size, and $v_o = 5 \times 10^{-5}$ m/s as determined by Blumenthal,[41] yield propagation times coincident with the measured failure times (Fig. 6.2).

More precise comparisons of crack propagation behavior are predicted upon measurements of the crack size, a, that emanates from an initial defect, a_i, (Fig. 4.19, 6.3) after exposure to a stress σ for time t (see Appendix). Two cracks originating at defects may be compared (Figs. 4.18 and 6.3). Figure 4.18 shows a crack extending through an elongated defect, while Fig. 6.3 shows a crack initiated at a spherical defect. The predicted crack length (Appendix 1) is considerably less than the measured length in the first instance, but larger in the second. The first crack has propagated through a poorly sintered area after initiation; presumably crack propagation is faster through such an area.

7. CONCLUSIONS

Analysis of microstructural defects as areas of high or low viscosity has revealed that the associated stress enhancement is of the order of a factor of two. The stress within an inhomogeneity is position independent. The principal stress, P_1^m, in the peripheral matrix is at a maximum around the poles of a high viscosity inclusion and at the equator of a low viscosity inclusion.

The prediction that cracks should initiate within or near defects as a result of stress enhancement has been substantiated; nearly all cracks observed were associated with defects. Cracks in the matrix may be associated with either subsurface defects or areas of low dihedral angle or surface diffusivity as described by Hsueh and Evans.[2] Identifiable fracture origins were found to be large grained regions, poorly sintered areas or inclusions. Glassy regions were not identified as sources of failure.

Cracks nucleate rapidly under the present conditions so that most of the failure time can be attributed to crack propagation. However, further study of crack nucleation and propagation is required.

The stresses required for cavity nucleation, in particular two grain boundary cavity nucleation, are much larger than the applied stresses and thus stress enhancement or critical stress reduction is required. The defect associated enhancement is not sufficient, and it is postulated that grain boundary sliding transients on wavy grain boundaries may generate the requisite stress. A possible time dependence may result from the grain rotation necessary to permit sliding.

The cavity morphologies observed are dependent on the applied stress. At high stresses (short t_f) triple point cavities

predominate. Few arrays of two grain boundaries are observed; those present are small and closely spaced. At intermediate stresses arrays of two grain boundary cavities are prevalent. The cavities grow until only easily fractured ligaments of material remain. At lower stresses (and long t_f) arrays of more widely spaced cavities are observed.

Crack growth occurs by coalescence of cavities on grain facets ahead of the crack. The damage zone ahead of the crack is extensive and crack branching often occurs.

The observed stress exponent, $n \approx 5$, is best accounted for by models based on crack propagation. The range of failure times predicted by the crack propagation model embraces the measured values. However, the strong dependence on initial crack length, a_i and the crack propagation constant, v_o and the accompanying lack of accurate values for these parameters does not permit a more precise comparison of theory and experiment. Crack lengths may be more accurately predicted; however, the effect of microstructural defects on crack propagation needs to be more fully addressed. Thus, none of the current failure time models are fully adequate under the present conditions.

8. FURTHER RESEARCH

The research effort involved in understanding the high temperature mechanical properties of ceramics, i.e., the mechanisms of creep and creep rupture has not been extensive and thus many problems remain to be addressed. Some recommendations for further research in this area arising from the current project follow.

The nature and cause of the inhomogeneous regions in these aluminas as well as in other materials need to be investigated. These defects are undoubtedly a result of the processing techniques, specifically the processing of the powder. A concurrent study of processing and high temperatue mechanical properties could be of great use in determining the cause of the defects and in preventing them. More applicable to the present study would be the use of sensitive analytical tools such as EELS and EDS for microchemical analysis of the inhomogeneities and matrix.

The effect of the heat treatment received during the test on the occurrence and appearance of inhomogeneous regions should also be investigated. Samples should be examined before and after testing to chart the changes, if any, in inhomogeneity number and appearance.

Further creep experiments at other temperatures would reveal the temperature dependence of cavitation. The strain rates at which the cavity type changes from triple point to two-grain interface will be temperature dependent because the nucleation stresses are temperature dependent and non-linear.

In order for the theory, advanced in section 6, explaining the source of the required enhanced nucleation stress to be applicable, it is necessary for the grain boundaries to be wavy and for grains to be

able to rotate. Grain boundaries are rarely straight and evidence of waviness is apparent in nearly all high resolution microscope studies. However, waviness of the order of a 0.1 μm wavelength is difficult to discern using present techniques. Very high resolution SEM or TEM may be necessary to observe such wavelengths. Grain rotation, while observed, is not yet fully understood. A theoretical study of grain rotation under constrained circumstances could help in further correlation of theory and experiment. A concurrent study of variations in grain boundary compositions and diffusivities by TEM could be undertaken.

The present study clearly indicates that the value of the exponent n is 5. Further investigations at other temperatures would confirm this. The exponent in the v-K relationship should be the same and further work in this area should also be performed.

Extension of the Eshelby analysis in Section 5 to non-spherical geometries could provide insights into the reason for crack initiation within inhomogeneities but growth outside such areas. Further understanding of crack paths and the competing effects of fracture resistance and maximum stress is desirable.

The above are some of the possible areas for further research. Obviously, cavitation and creep in other materials are of interest and comparisons could provide even more understanding of this extremely interesting and technologically important area.

ACKNOWLEDGMENT

I should like to thank Prof. A. G. Evans for his guidance in this work and the time and encouragement that he devoted to it. Others who deserve thanks are Professors I. Finnie and A. W. Searcy for reading the manuscript and Joyce Murphy and Mary Besser for typing. The support staff at MMRL, LBL, in particular Gloria Pelatonski, Ken Gangler, Erlene Fong, Glenn Baum and Walt Toutolmin and the Photo Lab deserve special thanks as do my fellow students, Phil Flaitz, Carolyn Rossington and Bill Blumenthal.

This work was supported by the Director, Office of Energy Research, Office of Basic Energy Sciences, Materials Science Division of the U.S. Department of Energy under contract No. DE-AC03-76SF00098.

REFERENCES

1. A. G. Evans, "Structural Reliability of Ceramics; A Processing Dependent Phenomenon," J. Am. Ceram. Soc. 65 [3] 127 (1982).
2. C. H. Hsueh and A. G. Evans, "Creep Fracture in Ceramic Polycrystals II. Effects of Inhomogeneities on Creep Rupture," Acta Met. 29 (1981) 1907.
3. A. H. Heuer, N. J. Tighe and R. M. Cannon, "Plastic Deformation of Fine-Grained Alumina (Al_2O_3): II. Basal Slip and Non-accommodated Grain-Boundary Sliding," J. Am. Ceram. Soc., 63 [1-2] 53 (1980).
4. F. R. N. Nabarro, Bristol Conference on Strength of Solids, Phys. Society, London (1948) 75.
5. C. Herring, J. Appl. Phys. 21 (1950) 437.
6. R. L. Coble, J. Appl. Phys. 34 (1963) 1979.
7. L. M. Lifshitz, Soviet Physics, JETP, 17 (1963) 909.
8. J. Gittus, "Creep Viscoelasticity and Creep Fracture in Solids," Wiley, 1975.
9. W. R. Cannon, "The Contribution of Grain-Boundary Sliding to Axial Strain during Diffusion Creep," Phil. Mag. 25 (1972) 1489-97.
10. R. M. Cannon, W. M. Rhodes, A. H. Heuer, "Plastic Deformation of Fine-Grained Alumina (Al_2O_3): I. Interface Controlled Diffusional Creep," J. Am. Ceram. Soc. 63 [1-2] (1980) 46-53.
11. R. Raj and M. F. Ashby, "On Grain Boundary Sliding and Diffusional Creep," Met. Trans. A, 2 (1971) 1113-1127.

12. J. M. Dynys, R. L. Coble, W. S. Coblenz and R. M. Cannon, "Mechanisms of Atom Transport During Initial Stage Sintering of Al_2O_3," 'Sintering Processes', Materials Science Research, 13, ed. K. Kuczynski (1979).

13. R. M. Cannon and R. L. Coble, "Review of Diffusional Creep of Al_2O_3," in 'Deformation of Ceramic Materials', R. C. Bradt and R. E. Tressler (eds.) Plenum, (1974).

14. D. Hull and D. E. Rimmer, "The Growth of Grain Boundary Voids under Stress," Phil. Mag., 4 (1959) 673.

15. J. M. Scheibel, R. L. Coble, and R. M. Cannon, "The Role of Grain Size Distributions in Diffusional Creep," to be published.

16. R. Raj and A. K. Ghosh, "Micromechanical Modeling of Creep Using Distributed Parameters," Acta Met., 29 [2] (1981) 283-292.

17. A. G. Evans, M. E. Meyer, K. W. Fertig, B. I. Davis, and H. R. Baumgartner, "Probabilistic Models for Defect Initiated Fracture in Ceramics," J. Nondestructive Evaluation 1 [2] (1980) 111-121.

18. A. G. Evans, D. R. Biswas and R. M. Fulrath, "Some Effects of Cavities on the Fracture of Ceramics: II. Spherical Cavities," J. Am. Ceram. Soc. 62 [1-2] (1979) 101-100.

19. J. D. Eshelby, "The Determination of the Elastic Field of an Ellipsoidal Inclusion, and Related Problems," Proc. Roy. Soc., London, 241A (1957) 370-96.

20. R. G. Fleck, D. M. R. Taplin and C. J. Beevers, "An Investigation of the Nucleation of Creep Cavities by 1 MV Electron Microscopy," Acta Met. 23 [4] (1975) 415-424.

21. R. Raj, "Nucleation of Cavities at Second Phase Particles in Grain Boundaries," Acta Met. 26 (1978) 995-1006.

22. A. G. Evans, "The High Temperature Failure of Ceramics," in Creep and Fracture of Engineering Materials, Pineridge Press, Swansea, United Kingdom.

23. J. R. Porter, W. R. Blumenthal and A. G. Evans, "Creep Fracture in Ceramic Polycrystals: I. Creep Cavitation Effects in Polycrystalline Alumina," Acta Met. 29 (1981) 1899.

24. J. Intrater and E. S. Machlin, "Grain Boundary Sliding and Intercrystalline Cracking," Acta Met. 7 (1959), 140-143.

25. A. L. Wingrove and D. M. R. Taplin, "The Morphology and Growth of Creep Cavities in α-Iron," J. Mat. Sci. 4 (1969) 789-796.

26. T. Chandra, J. J. Jonas and D. M. R. Taplin, "Grain-Boundary Sliding and Intergranular Cavitation During Superplastic Deformation of α/β Brass," J. Mat. Sci., 13 (1978) 2380-2384.

27. W. R. Blumenthal, "Cavitational Effects During Creep in Polycrystalline Alumina," M.S. Thesis, U.C. Berkeley (1980).

28. D. A. Miller and R. Pilkington, "Diffusional Deformation Controlled Creep Crack Growth," Met. Trans. A, 11A [13] (1980) 177-180.

29. D. S. Wilkinson, "A Model for Creep Cracking by Diffusion-Controlled Void Growth," Mat. Sci. and Eng. 49 (1981) 31-39.

30. T.-J. Chuang and J. R. Rice, "The Shape of Intergranular Creep Cracks Growing by Surface Diffusion," Acta Met. 21 (1973) 1625-1628.

31. T. -J. Chuang, K. I. Kagawa, J. R. Rice and L. B. Sills, "Overview No. 2: Non-Equilibrium Models for Diffusive Cavitation of Grain Interfaces," Acta Met. 27 (1979) 265-284.

32. G. M. Pharr and W. D. Nix, "A Numerical Study of Cavity Growth Controlled by Surface Diffusion," Acta Met. 27 (1979) 1615-1631.

33. A. Needleman and J. R. Rice, "Overview No. 9: Plastic Creep Flow Effects in the Diffusive Cavitation of Grain Bounardies," Acta Met. 28 (1980) 1315-1332.

34. I.-W. Chen and A. S. Argon, "Diffusive Growth of Grain-Boundary Cavities," Acta Met. 29 (1981) 1759-1768.

35. G. H. Edward and M. F. Ashby, "Intergranular Fracture During Power-Law Creep," Acta Met. 27 (1979) 1505-1518.

36. B. F. Dyson, "Constraints on Diffusional Cavity Growth Rates," Met. Sci. 10 (1976) 349-353.

37. J. R. Rice, "Constraints on the Diffusive Cavitation of Isolated Grain Boundary Facets in Creeping Polycrystals," Acta Met. 29 (1981) 675-81.

38. R. Raj and S. Baik, "Creep Crack Propagation by Cavitation Near Crack Tips," Met. Sci. 14 (1980) 385-394.

39. T.-J. Chuang, "A Diffusive Crack Growth Model for Creep Fracture," J. Am. Ceram. Soc., 65 [2] (1982) 93-103.

40. V. Vitek, "A Theory of Diffusion Controlled Intergranular Creep Crack Growth," Acta Met. 26 (1978) 1345-1356.

41. W. R. Blumenthal and A. G. Evans, unpublished work.

42. R. F. Cocks and M. F. Ashby, "The Growth of a Dominant Crack in a Creeping Material," Scripta Met. 16 (1982) 109-114.

43. R. Raj, H.M. Shih and H. H. Johnson, Correction to: "Intergranular Fracture at Elevated Temperature," Scripta Met. 11 (1977) 839-842.

44. T. Takasugi and V. Vitek, "Effect of Surface Diffusion on Creep Fracture," Met. Trans. A. 12A [4] (1981) 659-667.

45. S. M. Goods and W. D. Nix, "The Kinetics of Cavity Growth and Creep Fracture in Silver Containing Implanted Grain Boundary Cavities," Acta Met. 26 (1978) 739-752.

46. S. M. Goods and W. P. Nix, "The Coalescence of Large Grain Boundary Cavities in Silver During Tension Creep," Acta Met. 20 (1978) 753-758.

47. F. C. Monkman and N. J. Grant, "An Empirical Relationship Between Rupture Life and Minimum Creep Rate in Creep-Rupture Tests," Proc. ASTM 56 (1956) 593-620.

48. W. D. Nix, D. K. Matlock and R. J. Dimelfi, "A Model for Creep Fracture Based on the Plastic Growth of Cavities at the Tips of Grain Boundary Wedge Cracks," Acta Met. 25 (1977) 495-503.

49. L.-E. Svensson and G. L. Dunlap, "Growth of Intergranular Creep Cavities," Int. Met. Rev. [2] (1981) 109-131.

50. W. Beeré and M. V. Speight, "Creep Cavitation by Vacancy Diffusion in a Plastically Deforming Solid, "Met. Sci., 12 [4] (1978) 172-176.

51. G. G. Trantina and C. A. Johnson, "Subcritical Crack Growth in Boron-Doped SiC," J. Am. Ceram. Soc. 58 (1975) 344.

52. G. W. Hollenberg G. R. Terwillinger and R. S. Gordon, "Calculation of Stresss and Strains in Four-Point Bending Creep Tests," J. Am. Ceram. Soc. 54 [4] (1971) 196-199.

53. S. P. Timoshenko and J. W. Goodier, Theory of Elasticity, McGraw Hill, New York, 1951.

54. H. C. Chang and N. J. Grant, "Observations of Creep of the Grain Boundary in High Purity Aluminum," Trans. AIME 44 (1952) 619-625.

55. H. C. Chang and N. J. Grant, "Grain Boundary Sliding and Migration and Intercrystalline Failure Under Creep Conditions," Trans. AIME 197 305-312.

56. R. M. Fulrath, unpublished work.

57. J. E. Marion and A. G. Evans, private communication.

TABLE 4.1

Sample	Failure Time t_f secs	Peak Stress σ, MPa	Strain Rate $\dot{\varepsilon}_\infty$	Monkman-Grant Product $t_f \dot{\varepsilon}_\infty$
Series A		$\dot{D} = 6.35 \times 10^{-6}$ m/s		
BB	3300	103	1.00×10^{-6}	3.31×10^{-3}
CC	5580	92	1.00×10^{-6}	5.59×10^{-3}
PP	4580	103	1.05×10^{-6}	4.60×10^{-3}
Series B		$\dot{D} = 1.60 \times 10^{-5}$ m/s		
U	840	163	2.48×10^{-6}	2.08×10^{-3}
Y	534	163	2.49×10^{-6}	1.33×10^{-3}
AA	1221	123	2.49×10^{-6}	3.04×10^{-3}
EE	540	129	2.52×10^{-6}	1.30×10^{-3}
FF	816	149	2.52×10^{-6}	2.00×10^{-3}
GG	366	188	2.52×10^{-6}	9.19×10^{-3}
HH	450	151	2.48×10^{-6}	1.12×10^{-3}
KK	468	134	2.55×10^{-6}	1.19×10^{-3}
MM	567	158	2.48×10^{-6}	1.40×10^{-3}
NN	930	148	2.62×10^{-6}	2.43×10^{-3}
OO	666	171	2.65×10^{-6}	1.76×10^{-3}
Series C		$\dot{D} = 3.18 \times 10^{-5}$ m/s		
S	71	210	4.94×10^{-6}	3.50×10^{-4}
T	98	217	4.96×10^{-6}	4.80×10^{-4}
X	115.5	205	5.04×10^{-6}	5.82×10^{-4}
Series D		$\dot{D} = 6.35 \times 10^{-5}$ m/s		
V	23	257	9.93×10^{-6}	2.28×10^{-4}
W	37.5	246	9.90×10^{-6}	3.71×10^{-4}
Z	29.5	276	9.98×10^{-6}	2.94×10^{-4}

FIGURE CAPTIONS

Fig. 2.1 Nucleation stress as a function of temperature for two grain boundary and four grain corner cavities (after Evans, Ref. 1).

Fig. 3.1 Schematic of three-point bending fixture and testing apparatus.

Fig. 4.1 Schematic of typical load vs. time curve for creep rupture experiment.

Fig. 4.2 Experimental data -- peak stress as a function of failure time, $t_f \propto \hat{\sigma}^{-5}$.

Fig. 4.3 Experimental data -- normalized failure time $t_f \dot{\varepsilon}_\infty$ as a function of peak stress.

Fig. 4.4 Inclusion located at the failure origin.

Fig. 4.5 Large grained region in Al_2O_3 #1, showing approximate position.

Fig. 4.6 Large grained region with internal void in Al_2O_3 #1 - SEM.

Fig. 4.7 Tensile surface showing extent of poorly sintered regions (Al_2O_3 #2).

Fig. 4.8 Tensile surface showing lines of poorly sintered areas (Al_2O_3 #2).

Fig. 4.9 A) Poorly sintered area.

B) Void at site of inclusion.

C) Poorly sintered area, showing surface patterning of grains, as a result of thermal etching.

Fig. 4.10 Fracture surface -- glassy area - note holes formed in glass (Al_2O_3 #1).

Fig. 4.11 Fracture surface -- glassy ligaments on large grained area (Al_3O_3 #1).

Fig. 4.12 Crack-like defect parallel to tensile direction on tensile surface. Note cracks emanating from ends and along defect (Al_2O_3 #2).

Fig. 4.13 Crack-like defect on tensile surface with cracks originating along the length. Damage around cracks is extensive (Al_2O_3 #2).

Fig. 4.14 Internal void on fracture surface (Al_3O_3 #2).

Fig. 4.15 Fracture origin showing characteristic radial lines (Al_2O_3 #2).

Fig. 4.16 Crack running through poorly sintered area after ~30% t_f (Al_2O_3 #2).

Fig. 4.17 Tensile surface after ~66% t_f -- extensive cracking associated with defect (Al_2O_3 #2).

Fig. 4.18 Tensile surface after ~66% t_f -- defective areas and associated cracks (Al_2O_3 #2).

Fig. 4.19 Tensile surface -- cracks forming in matrix at poles of spherical defect (Al_2O_3 #2).

Fig. 4.20 A) Fracture origin on tensile surface.

B) Fracture surface — fracture origin is only visible on tensile surface (Al_2O_3 #2).

Fig. 4.21 Tensile surface — crack system not associated with any visible defects. Note damage around crack tips and crack branching (Al_2O_3 #2).

Fig. 4.22 A) Tensile surface -- Series A - extensive overall damage.

B) Fracture surface -- crack branching.

Fig. 4.23 Fracture surface -- array of equilibrium shaped two grain boundary cavities in a large grained area. (Note pore in lower right corner) (Al_2O_3 #2). Short wavelength boundary can be seen in upper left corner.

Fig. 4.24 Arrays of crack-like and equilibrium two grain boundary cavities in large grained region on fracture surface (Al_2O_3 #1).

Fig. 4.25 Array of cavities on two grain interface on fracture surface (Al_2O_3 #2).

Fig. 4.26 Arrays of highly facetted two grain boundary cavities on fracture surface. Cavities are present on both large and small grains. Cavity size on one grain is not constant. (Series B, Al_2O_3 #2).

Fig. 4.27 Two grain boundary cavities -- cavities on different faces of one grain are of different sizes. Only certain faces of some grains are cavitated. (Series B, Al_2O_3 #2).

Fig. 4.28 Arrays of two grain boundary cavities showing ligaments. Triple point cavities are also present. (Series B, Al_2O_3 #2).

Fig. 4.29 Tensile surface -- arrays of two grain boundary cavities on either side of a crack. (Series B, Al_2O_3 #2).

Fig. 4.30 Array of two grain boundary cavities on fracture surface -- cavities are small, very closely spaced, and form lines. (Series C, Al_2O_3 #2).

Fig. 4.31 Cavity spacing, b, as a function of peak stress, $b \sim \alpha\sigma^{-1}$.

Fig. 4.32 Triple point cavities on fracture surface. (Series D, Al_2O_3 #2.)

Fig. 4.33 Schematic of cavity morphology as a function of peak stress and failure time.

Fig. 4.34 Partially crept sample broken at room temperature showing formation of cavities at an early stage. Transgranular fracture is also apparent. (Series B, $t \sim 30\% t_f$, Al_2O_3 #2).

Fig. 4.35 Fracture surface in compressive area. Note absence of two grain boundary cavities. (Series B, Al_2O_3 #2).

Fig. 4.36 Room temperature fracture surface of low stress region — note absence of two grain boundary cavities.

Fig.4.37 A) Tensile surface showing grain boundary sliding. (Series B, Al_2O_3 #2).

B) Tensile surface — large grain has slid outwards. Note grain boundary ledges (white lines). (Series A, Al_2O_3 #2).

Fig. 4.38 Optical micrograph of fracture sample showing color change from grey to white associated with tensile surface.

Fig. 5.1 Schematic of inclusion (large grained region) showing principal directions.

Fig. 5.2 Normalized stress, P_1^p/σ_∞ as a function of grain size ration, ζ. Increasing ζ is equivalent to increasing viscosity.

Fig. 5.3 Normalized peripheral stresses, p^m/σ_∞ as a function of Θ, for $\eta_p > \eta_m$.

Fig. 5.4 Normalized peripheral stresses, p^m/σ_∞ as a function of θ, for $\eta_p = 0$.

Fig. 6.1 Stresses arising from sliding of wavy grain boundary (after Raj and Ashby, Ref. 11).

Fig. 6.2 Comparison of predicted and experimental results, $\hat{P}$ vs. t_f.

Fig. 6.3 Crack through poorly sintered area after ~66% t_f.

APPENDIX I

A crack propagation model has been developed by Evans[22] in which the crack propagation time at constant stress is given by

$$t = \frac{2K_c^n}{\sigma_\infty^2 Y^2 v_o (n-2)} \left[\frac{1}{K_i^{n-2}} - \frac{1}{K_f^{n-2}} \right] \qquad (A1)$$

Crack sizes are easily measured and thus it is preferrable to express Eq. (A1) in terms of initial and final crack sizes in order to determine the applicability of the crack propagation model to the present problem.

The stress intensity factor $K = \sigma Y \sqrt{a}$ and so:

$$\frac{t\sigma_\infty^n Y^n v_o (n-2)}{2K_c^n} = \frac{1}{a_i^{(n-2)/2}} - \frac{1}{a_f^{(n-2)/2}} \qquad (A2)$$

The final crack size is therefore;

$$a_f = \frac{1}{a_i^{(n-2)/2}} + \frac{tv_o(n-2)}{2} \frac{\sigma_\infty Y}{K_c}^{n^{-2/(n-2)}} \qquad (A3)$$

It is thus possible to compare experimental observations of crack growth with Eq. (A3).

As previously noted there is considerable uncertainty in the choice of a value for v_o and results will be presented for two choices of v_o; 5×10^{-5} m/s and 10^{-5} m/s. The value of the exponent n is 5.

The crack in Fig. 6.3 is assumed to have been nucleated at the circular defect and to have propagated through the matrix under a stress $\sigma_\infty \sim 140$ MPa for the entire failure time of 789 s. The initial defect size is thus ~ 13 μm; a_i is half the defect size, i.e.,

a_i ~6.5 μm. The final crack size, a_{f_p}, can then be calculated to be ~8.5 μm when $v_o = 5 \times 10^{-5}$ m/s and ~65 μm when $v_o = 10^{-5}$ m/s. The measured value of a_f is ~32 μm.

The crack in Fig. 4.18, has nucleated at the spherical defect and propagated through a further unsintered area. In this case, $\hat{\sigma}$ ~170 - MPa, t = 600 s, a_i ~16 μm and a_{f_p} ~28 μm when $v_o = 10^{-5}$m/s (Eq. (A3) cannot be used in this case if $v_o = 5 \times 10^{-5}$ m/s). The measured value of a_f is ~65 μm.

The predicted a_f in the first case is thus conservative i.e., $a_{f_{predicted}}$ (65 μm) > $a_{f_{measured}}$ (32 μm) compared to the underestimation of crack size ($a_{f_{predicted}}$ = 28 μm, $a_{f_{measured}}$ = 65 μm) in the second case where the crack has propagated through a defective area.

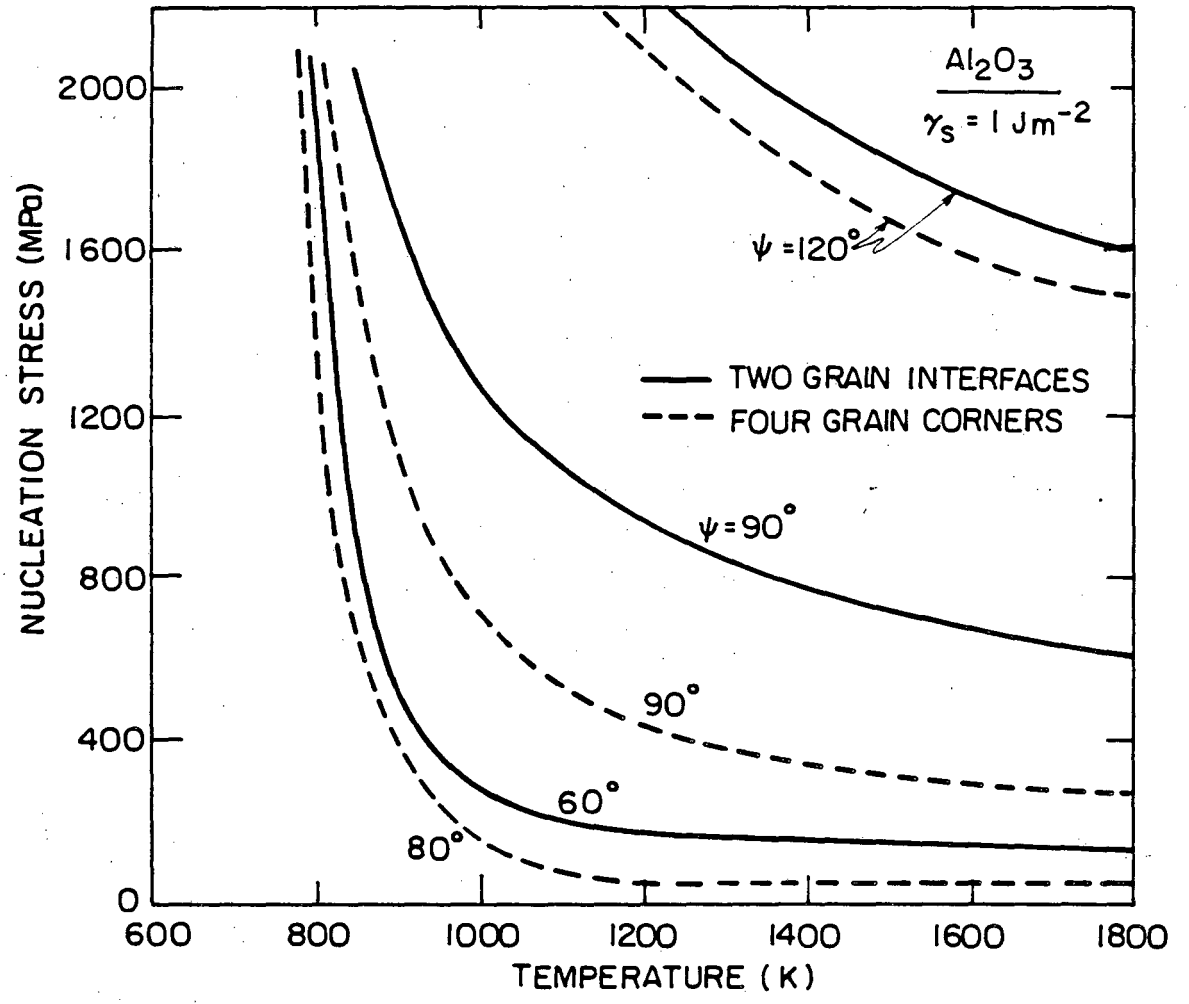
Al_2O_3
$\gamma_s = 1\ Jm^{-2}$
$\psi = 120°$
TWO GRAIN INTERFACES
FOUR GRAIN CORNERS
$\psi = 90°$
90°
60°
80°
NUCLEATION STRESS (MPa)
TEMPERATURE (K)
0
400
800
1200
1600
2000
600
800
1000
1200
1400
1600
1800
XBL822-5275

Fig. 2.1

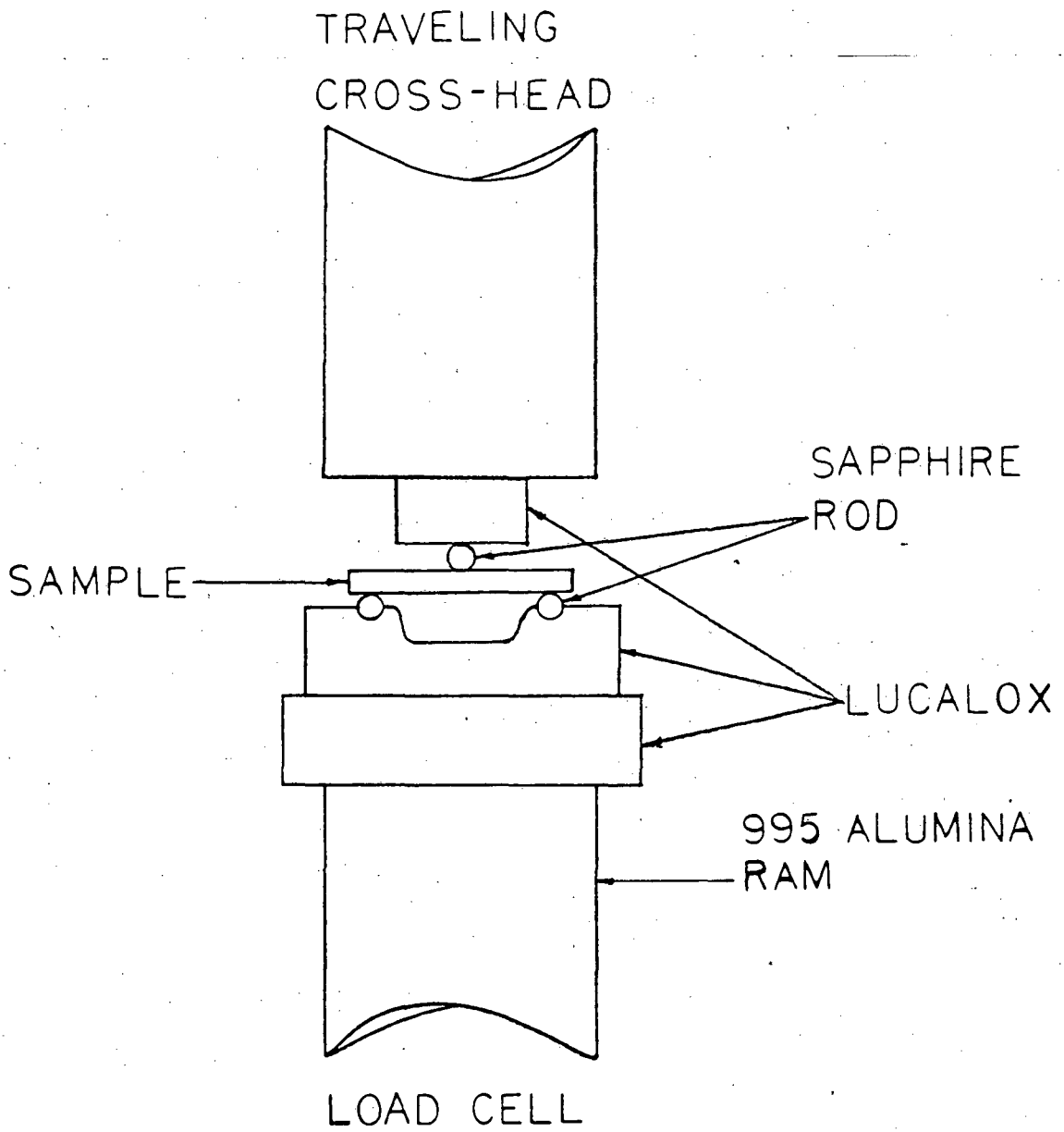
TRAVELING
CROSS-HEAD
SAPPHIRE
ROD
SAMPLE
LUCALOX
995 ALUMINA
RAM
LOAD CELL
XBL 805-5202

Fig. 3.1

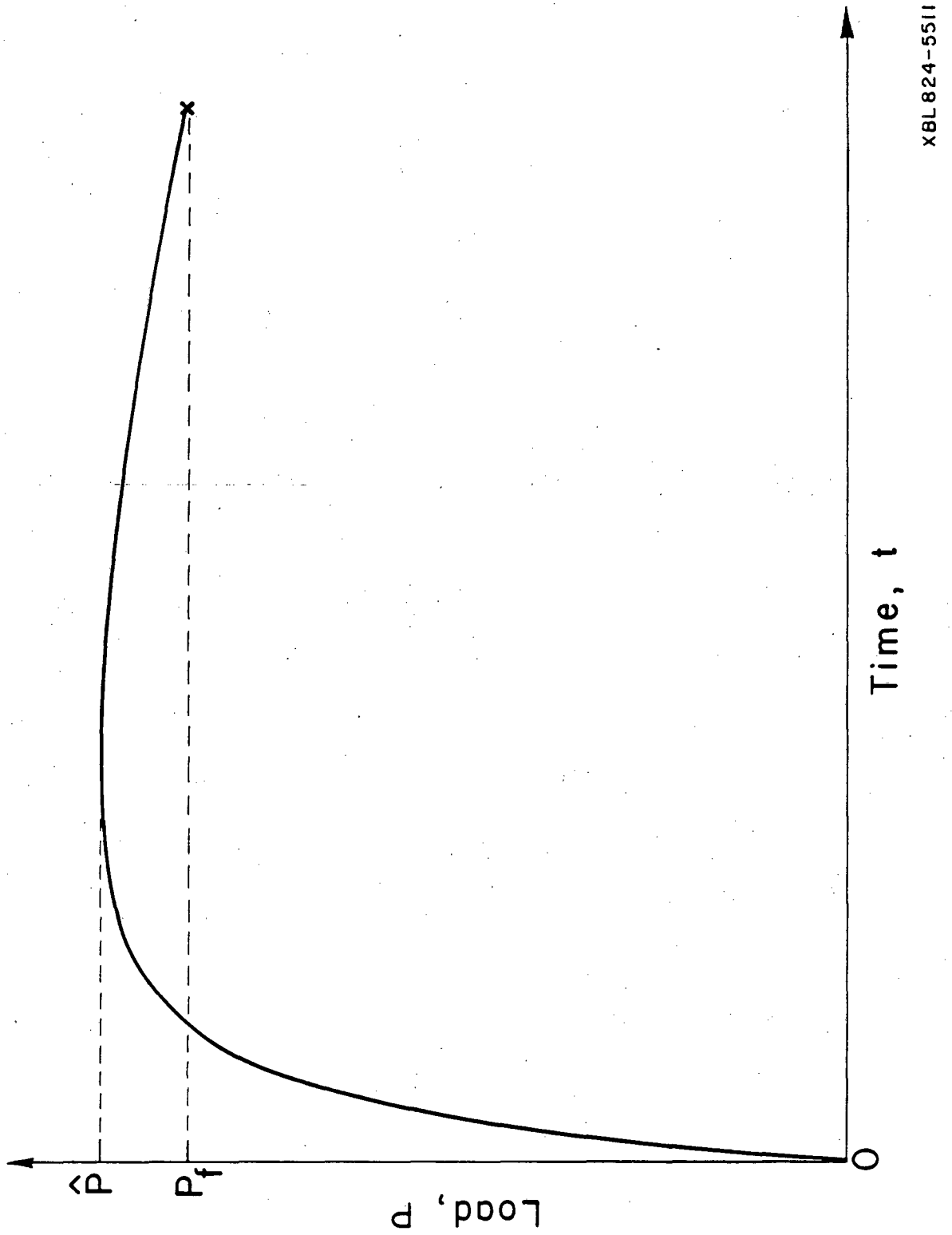

Fig. 4.1

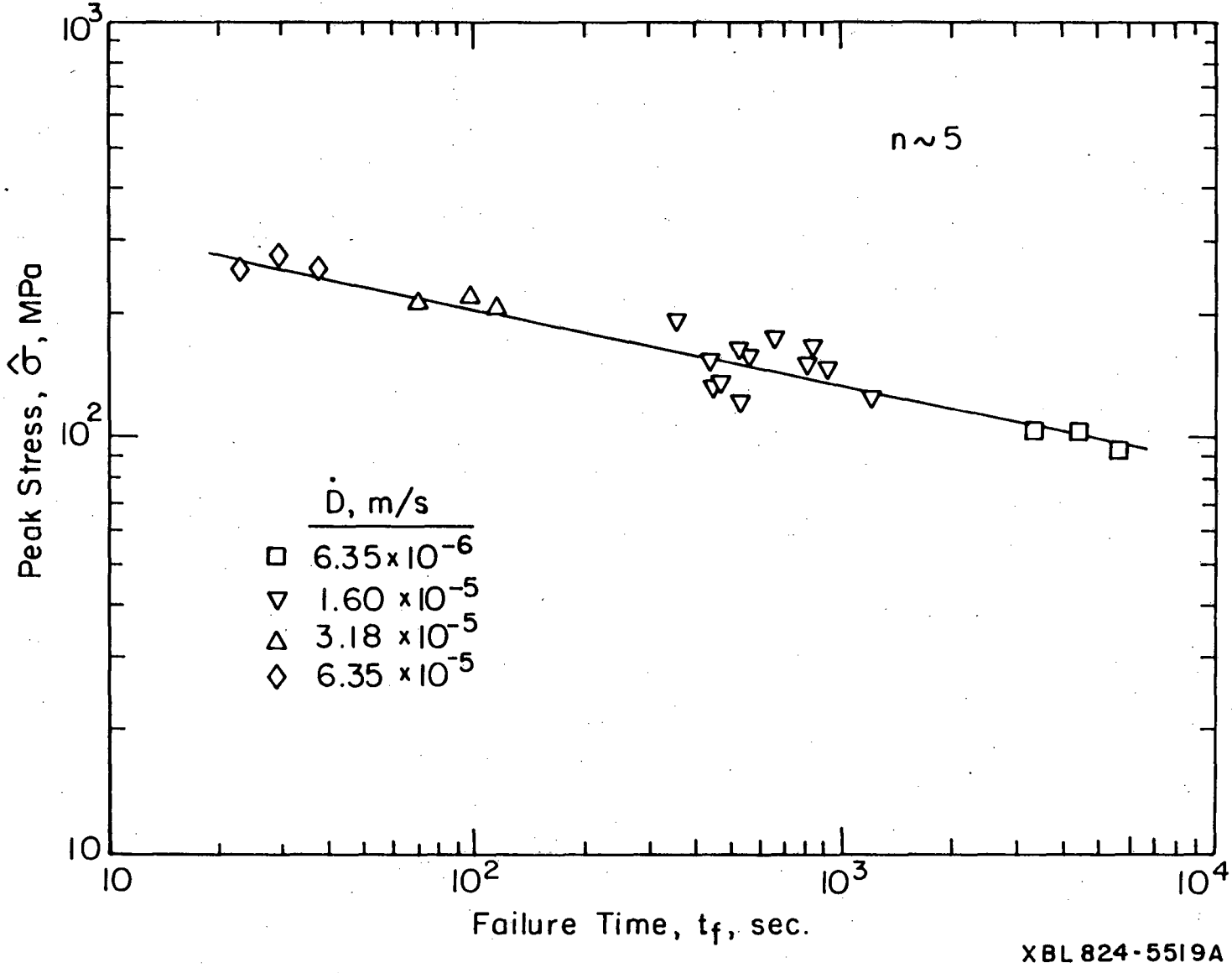
10^3
10^2
10
10
10^2
10^3
10^4
n ~ 5
Peak Stress, $\hat{\sigma}$, MPa
Failure Time, t_f, sec.
$\dot{D}$, m/s
□ 6.35×10^{-6}
▽ 1.60×10^{-5}
△ 3.18×10^{-5}
◇ 6.35×10^{-5}
XBL 824-5519A

Fig. 4.2

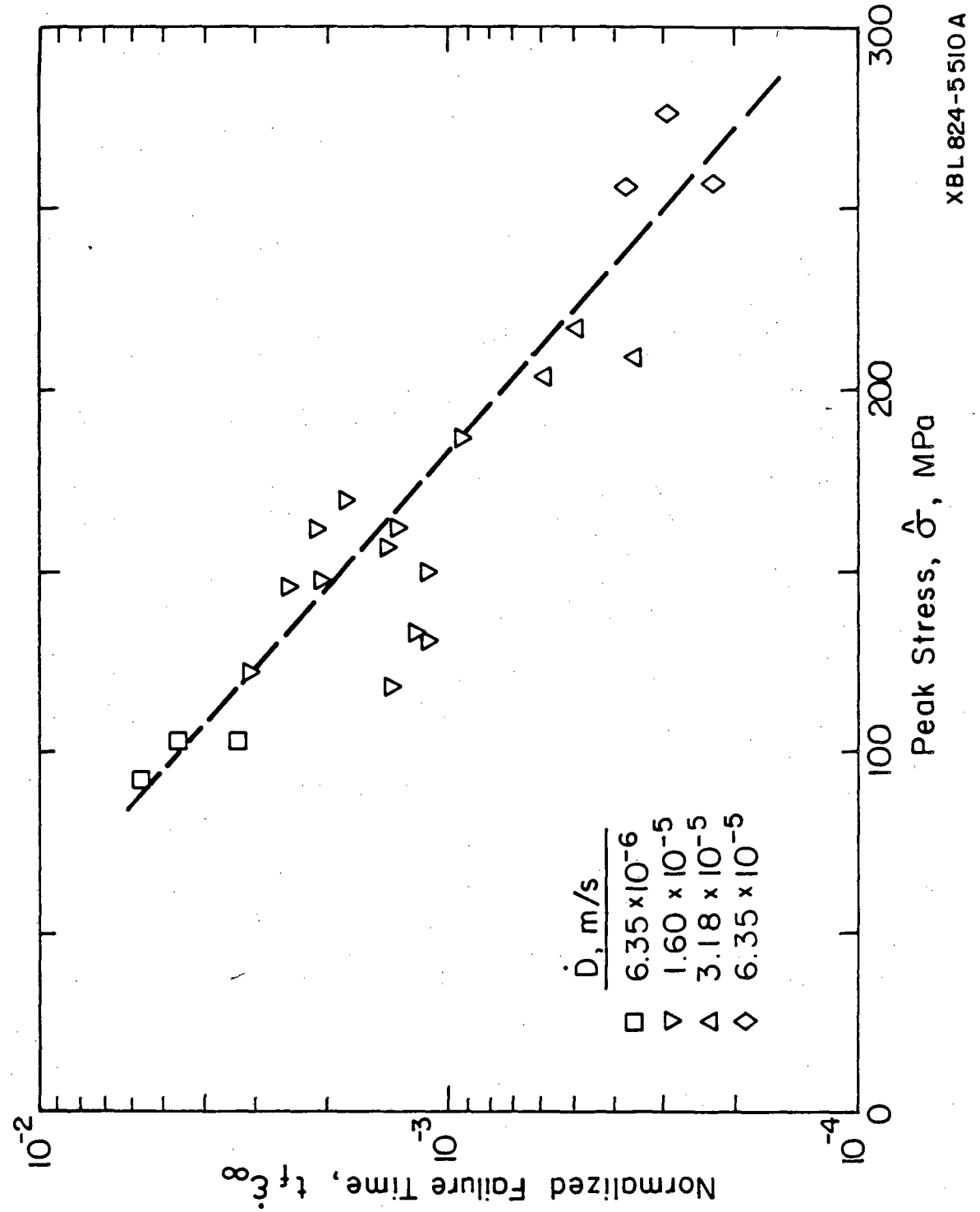
Normalized Failure Time, $t_f \dot{\varepsilon}_\infty$
10^{-2}
10^{-3}
10^{-4}
0
100
200
300
Peak Stress, $\hat{\sigma}$, MPa
$\dot{D}$, m/s
□ 6.35×10^{-6}
▽ 1.60×10^{-5}
△ 3.18×10^{-5}
◇ 6.35×10^{-5}
XBL 824-5510 A

Fig. 4.3

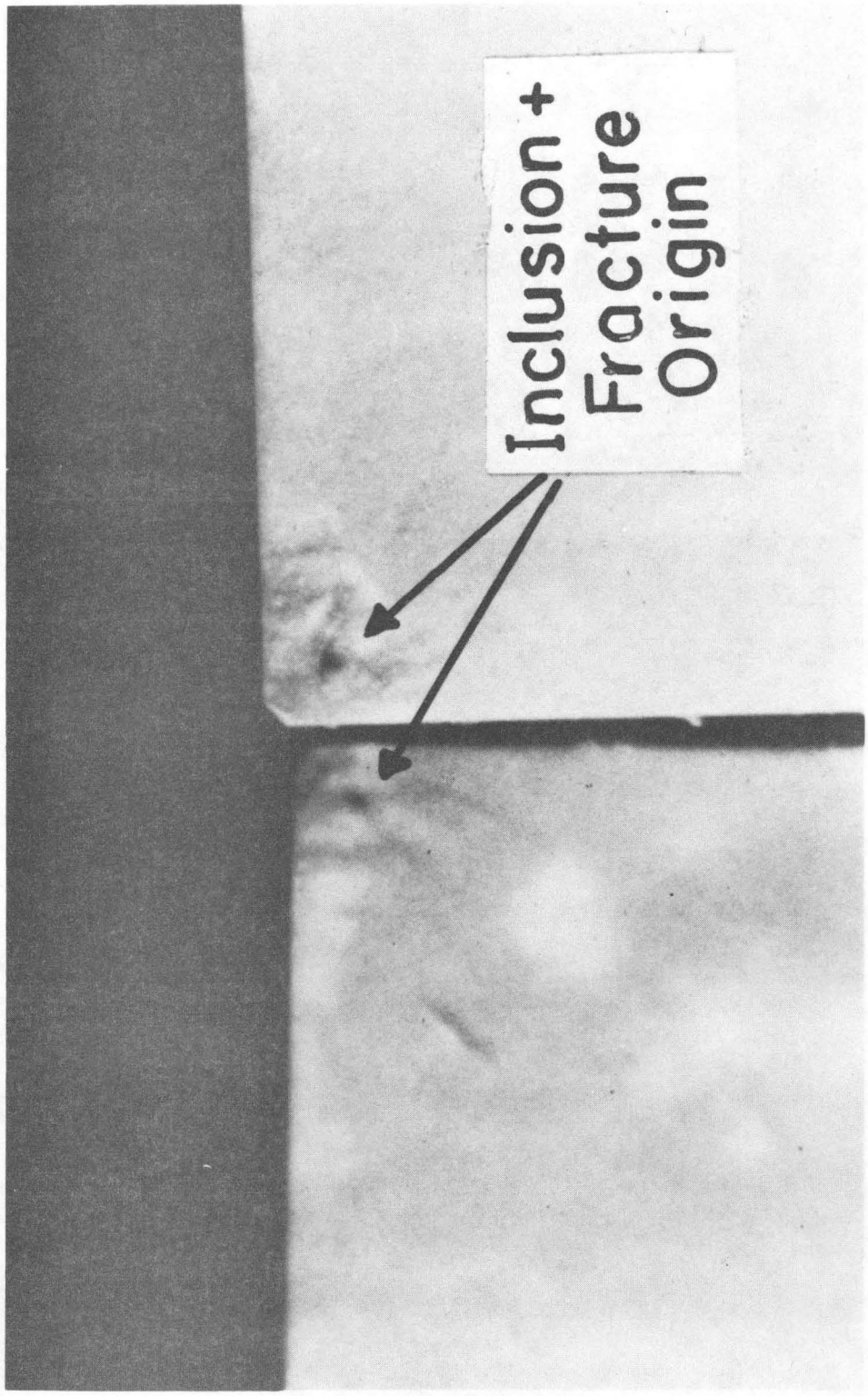

CBB-826-5405-A

Fig. 4.4

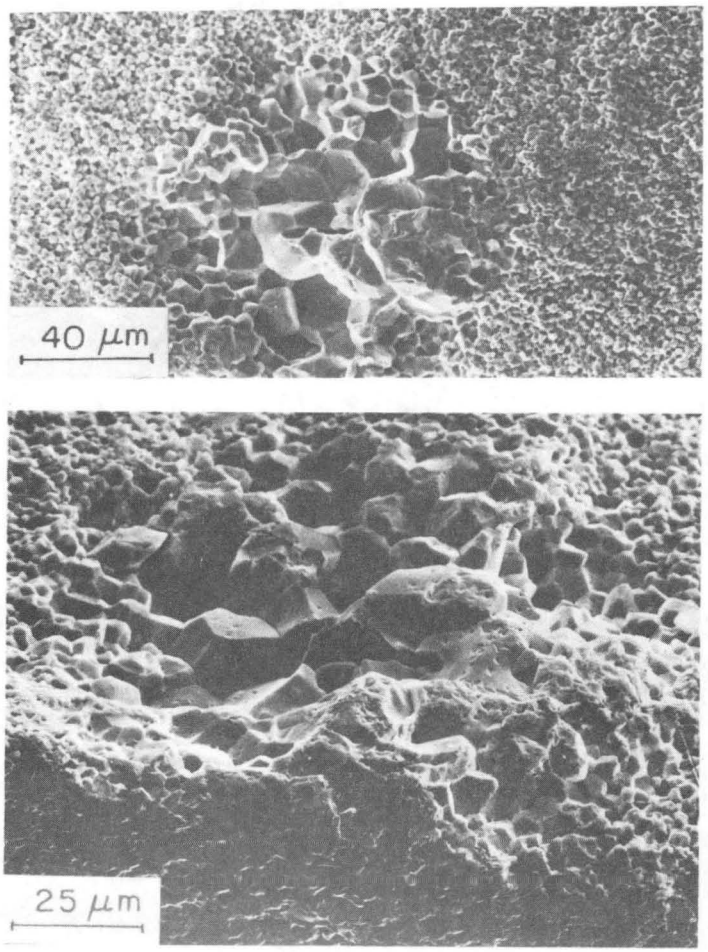

XBB-811-497

Fig. 4.5

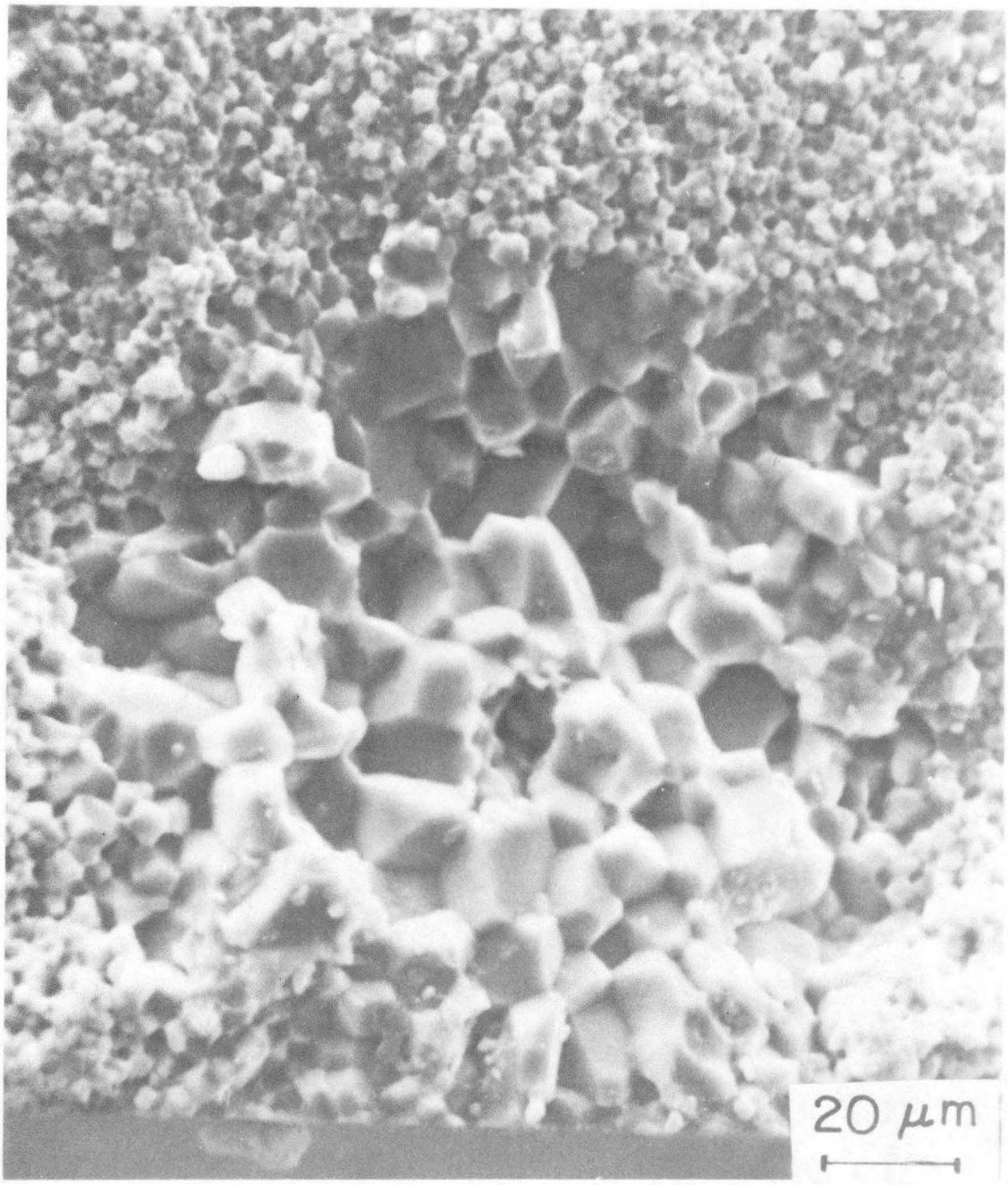

XBB 810-9885

Fig. 4.6

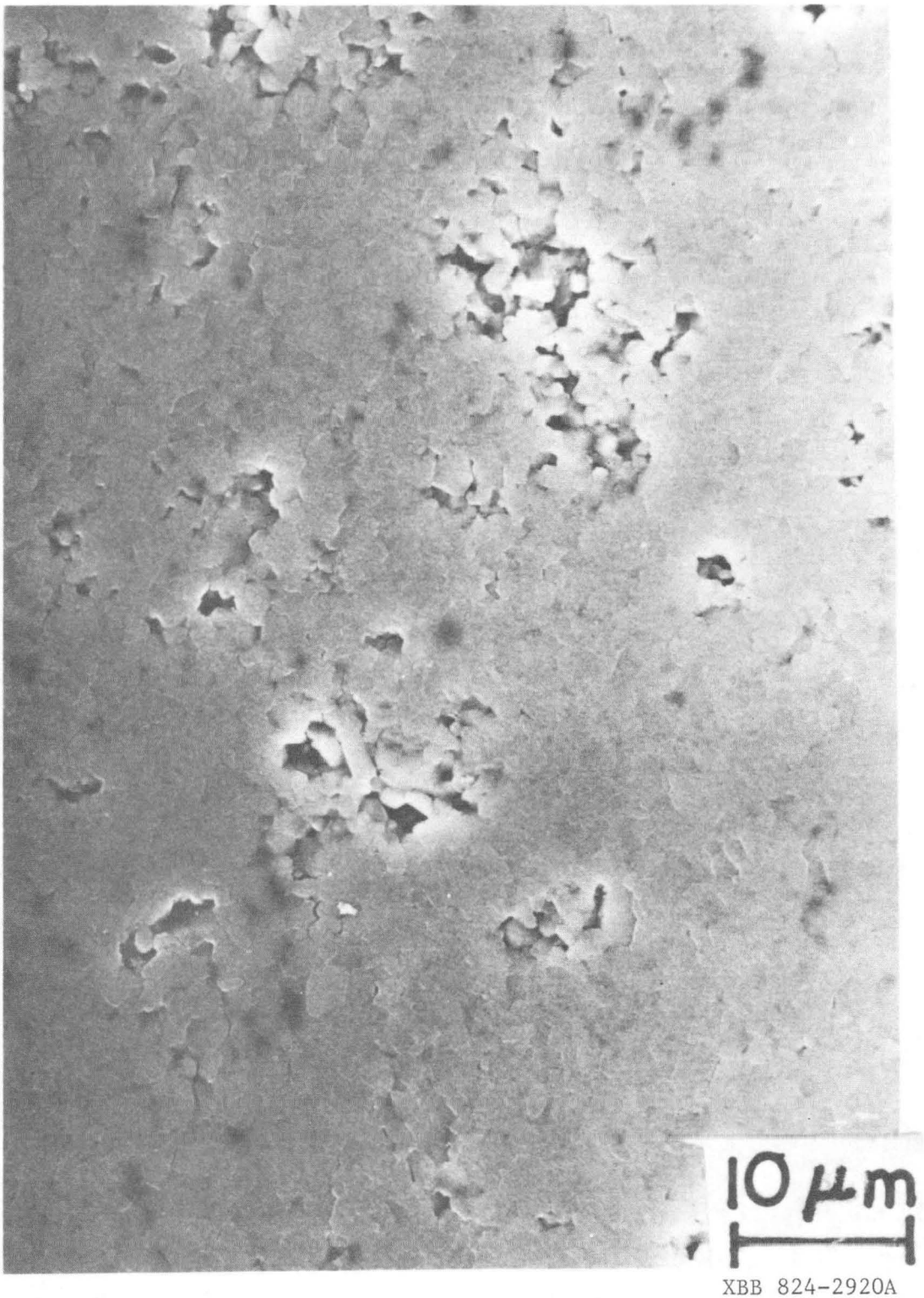

Fig. 4.7

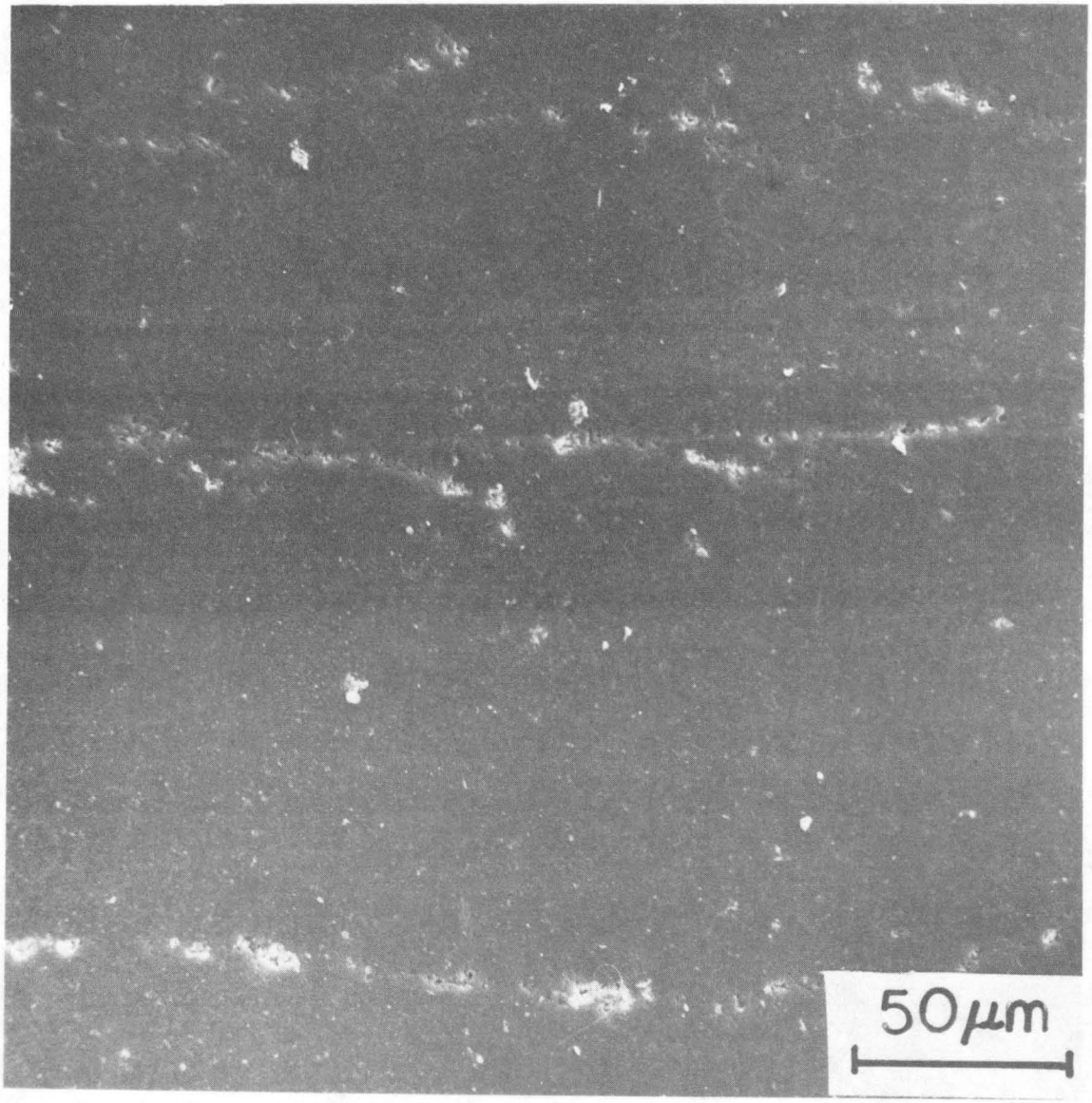

XBB 826-5401A

Fig. 4.8

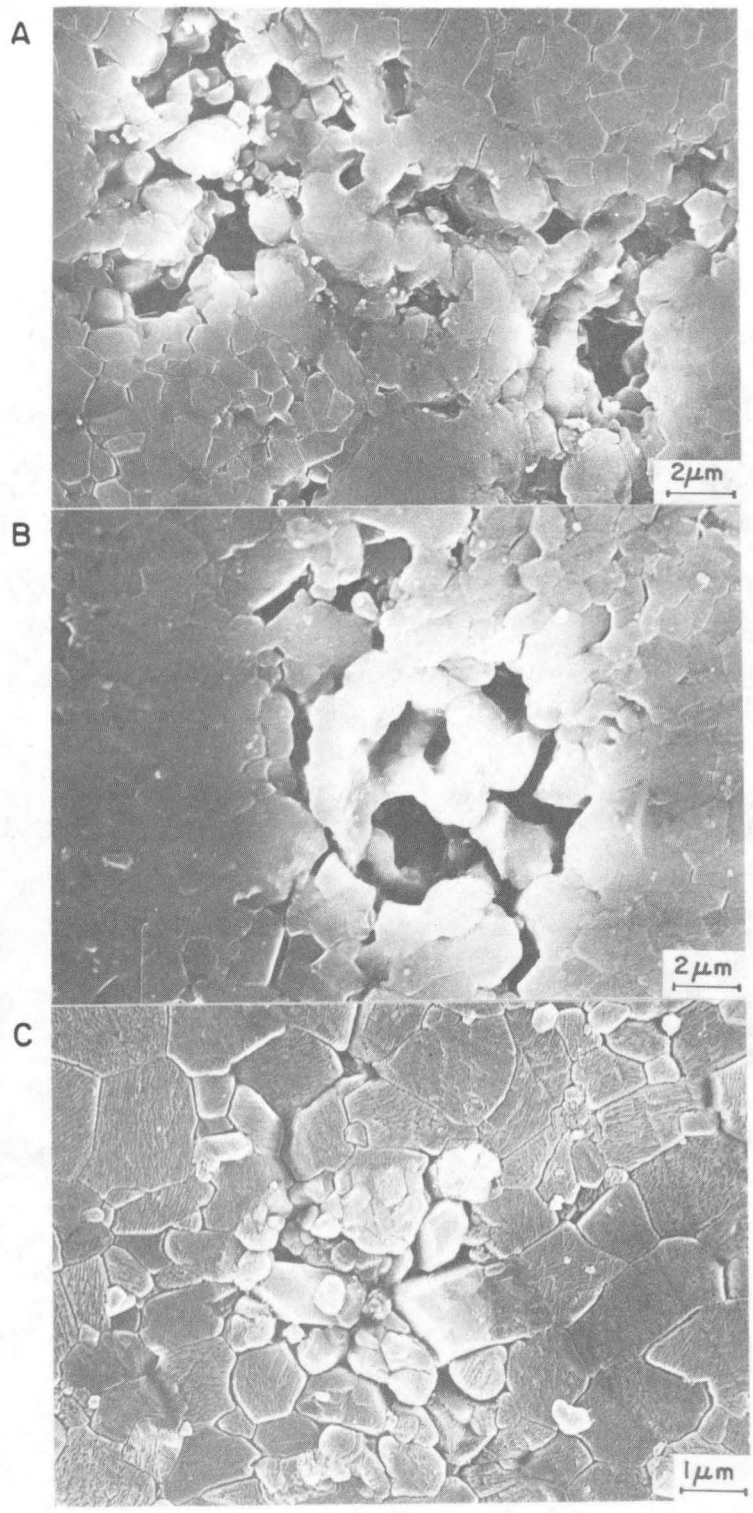

XBB 824-3299

Fig. 4.9

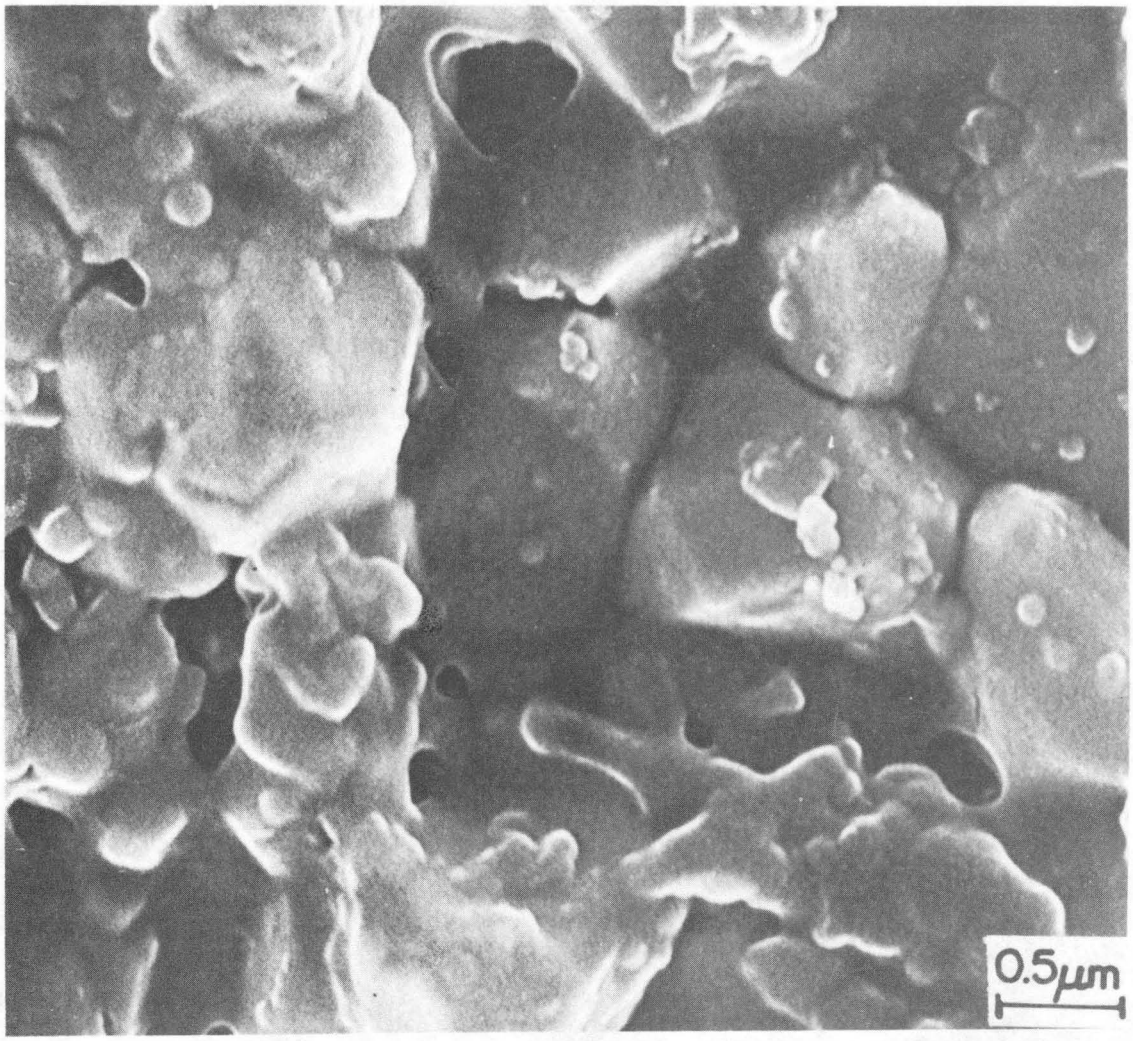

XBB 825-2936A

Fig. 4.10

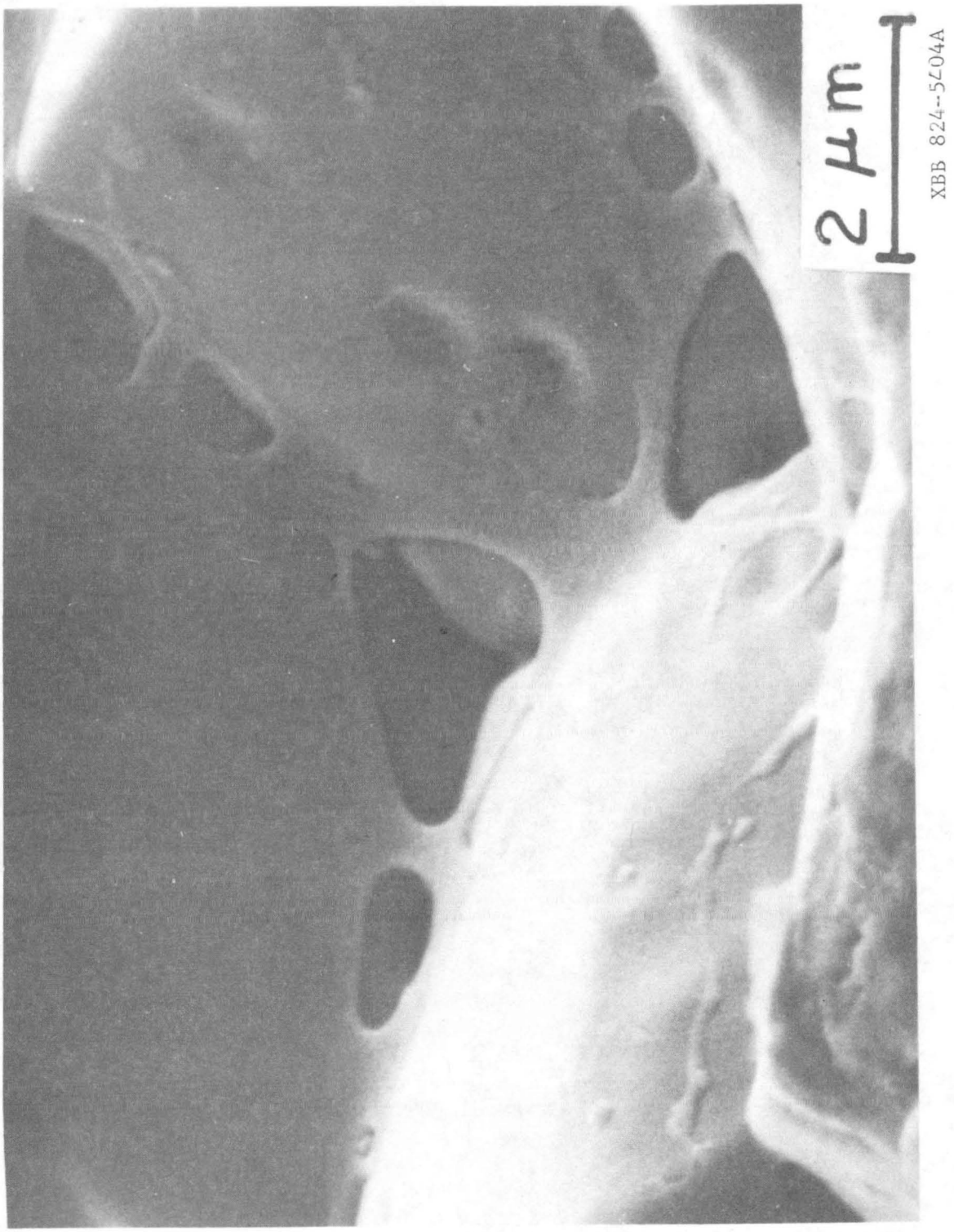

Fig. 4.11

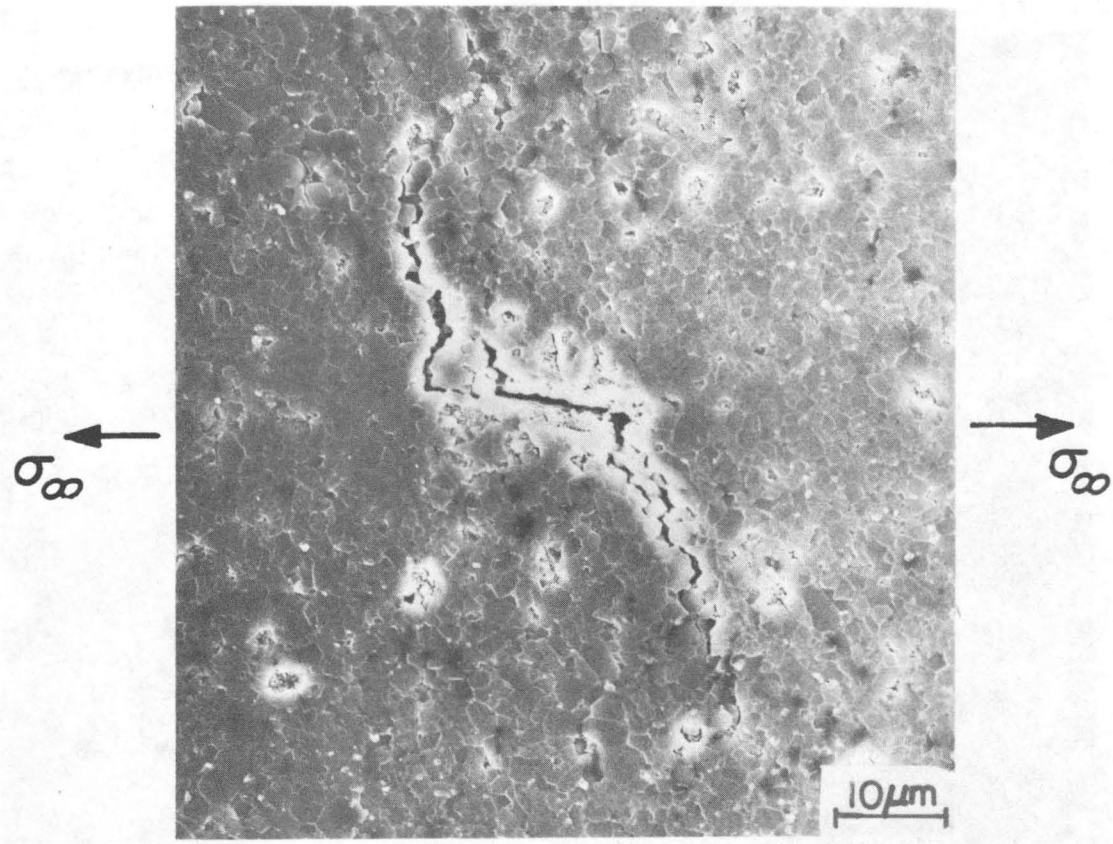

XBB 824-2962A

Fig. 4.12

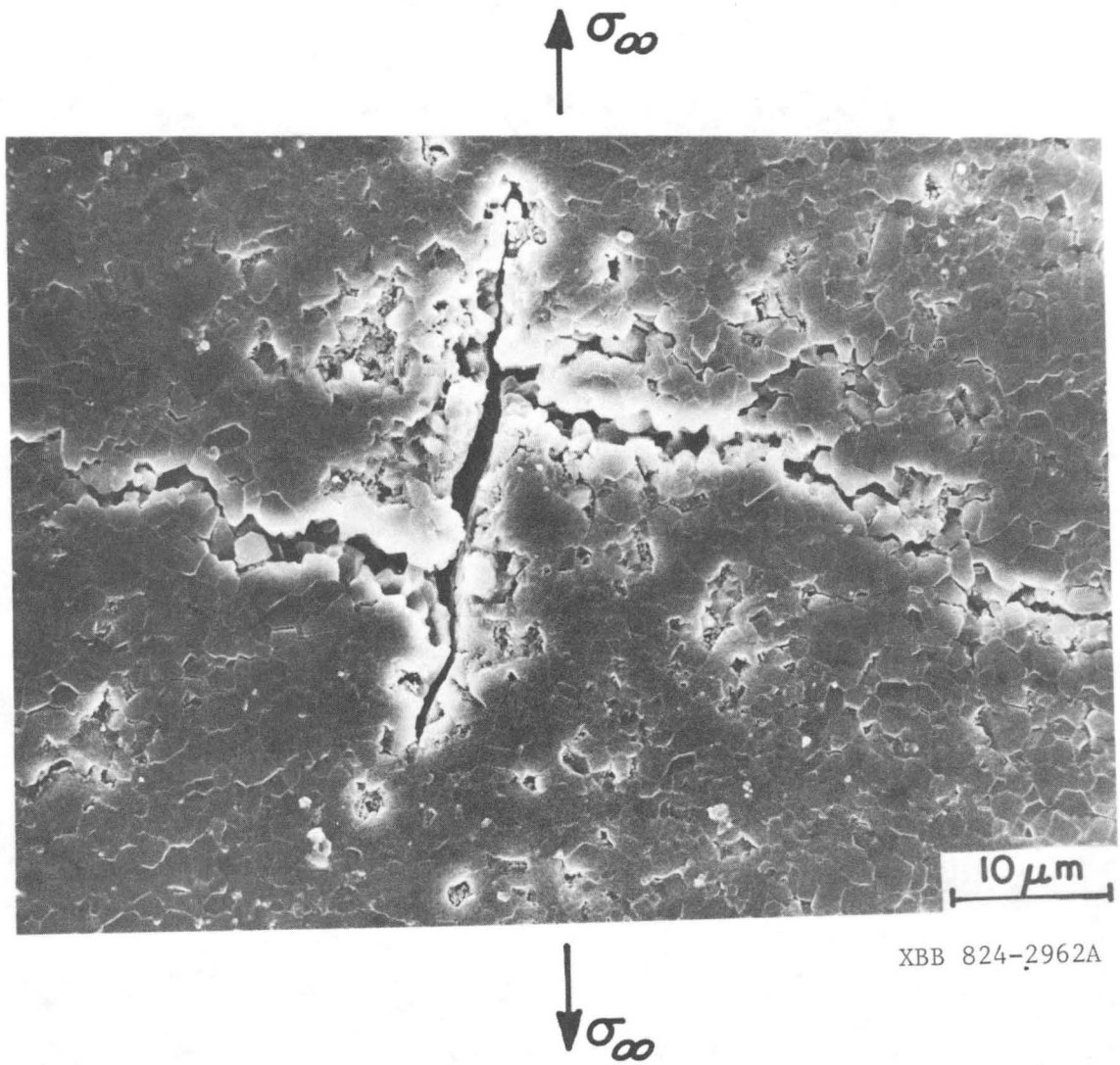

XBB 824-2962A

Fig. 4.13

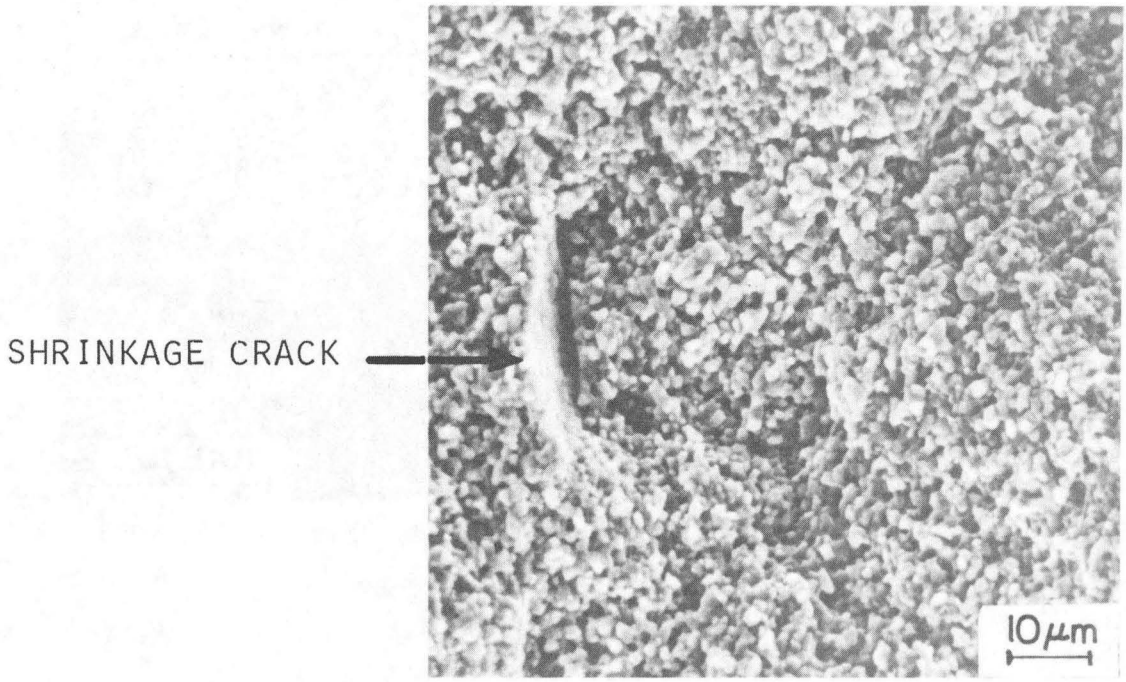

XBB 823-2181

Fig. 4.14

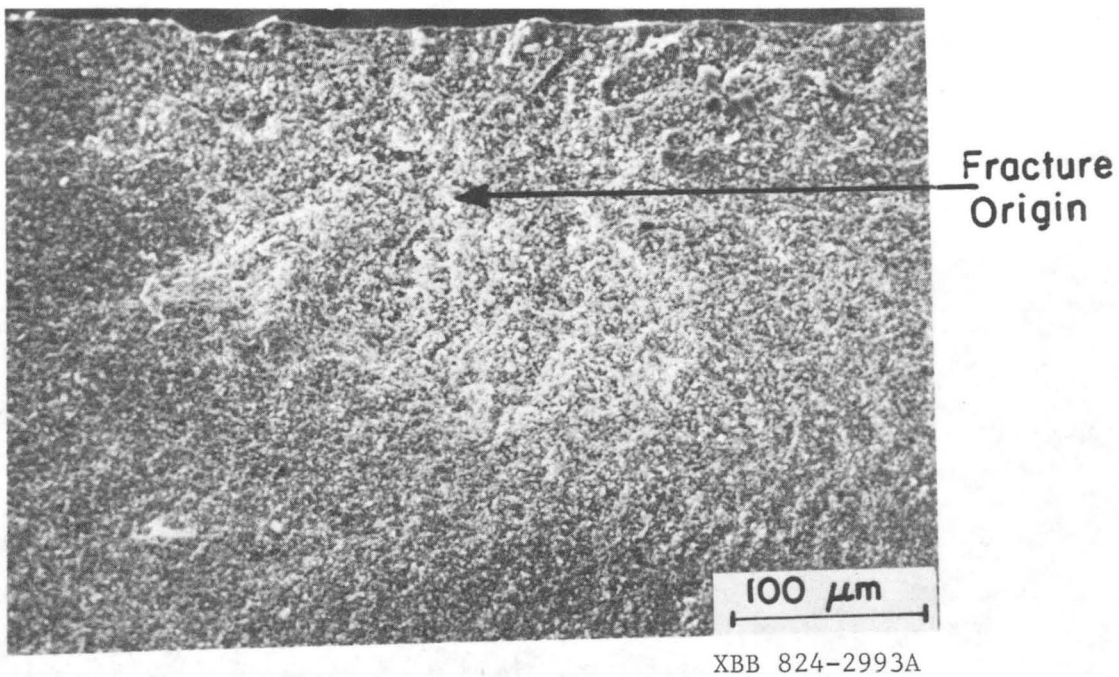

XBB 824-2993A

Fig. 4.15

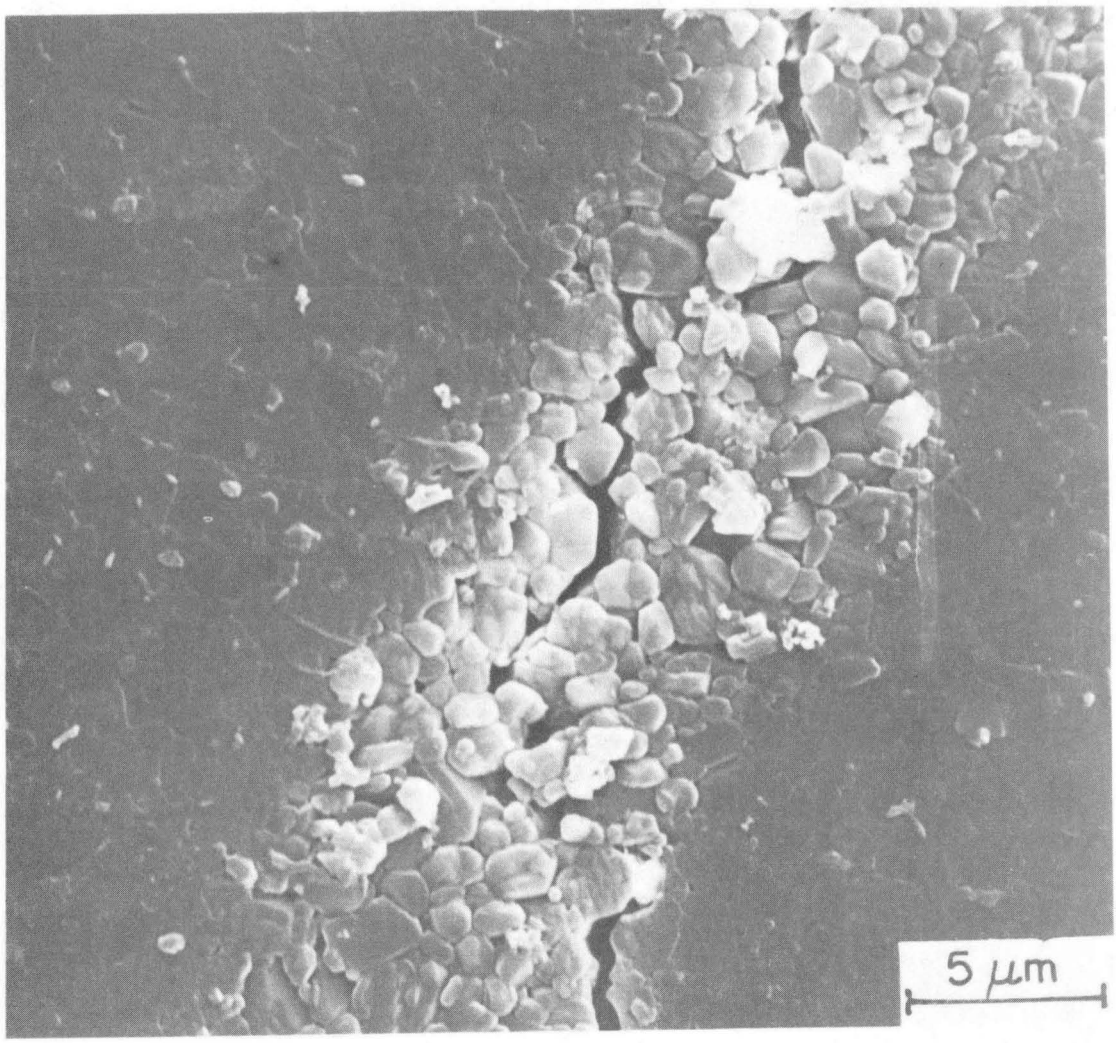

XBB 824-4015

Fig. 4.16

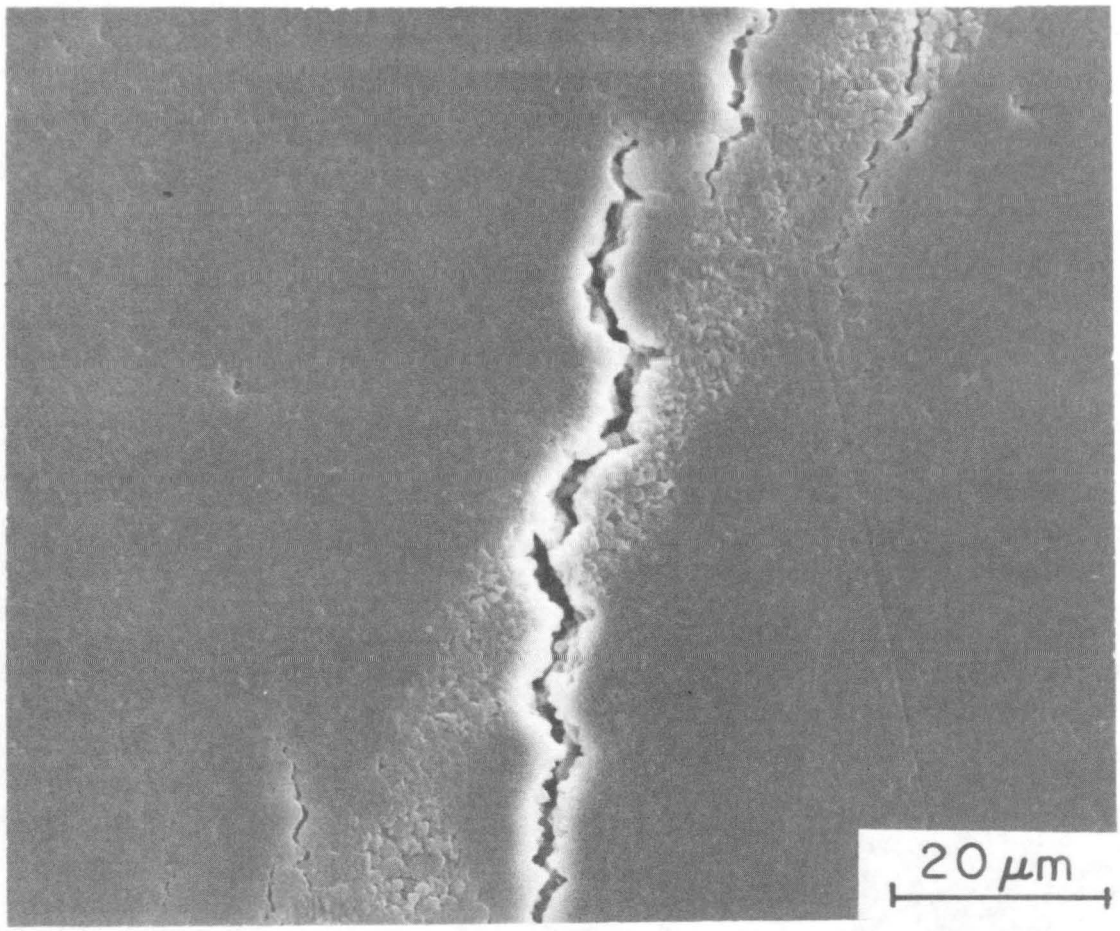

XBB 825-4191A

Fig. 4.17

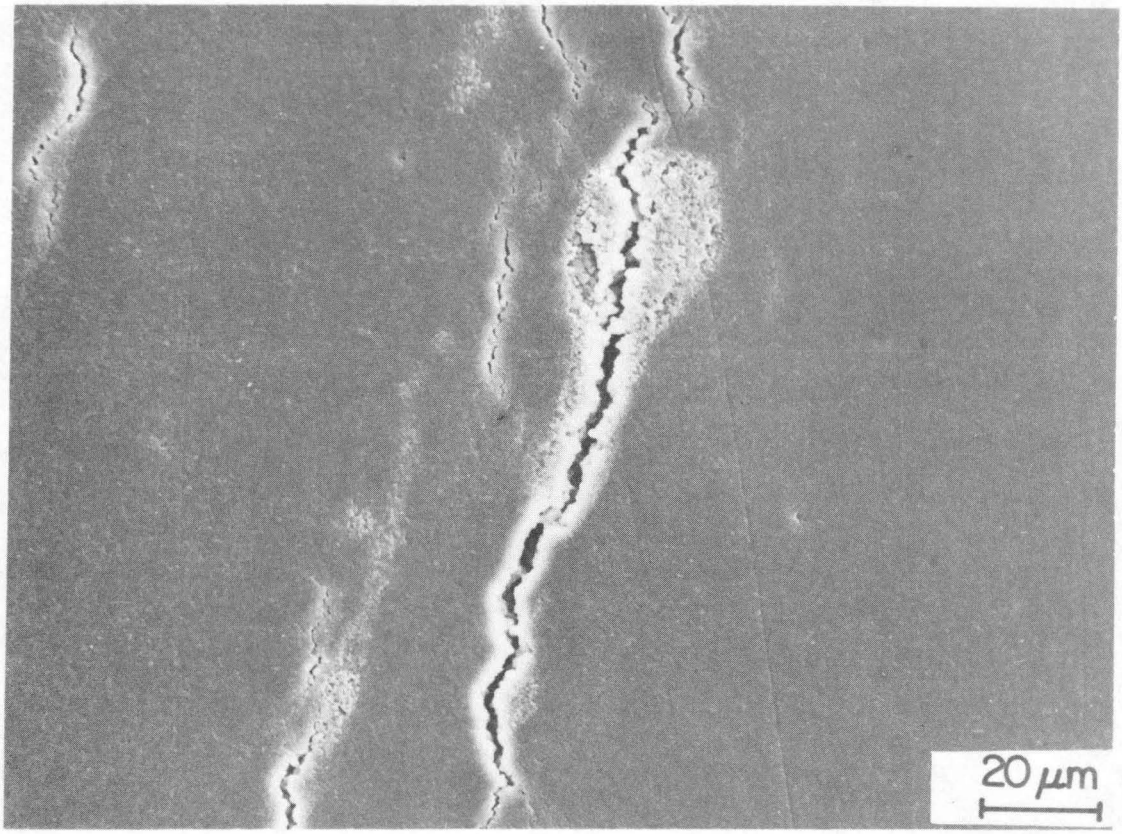

XBB 825-4694A

Fig. 4.18

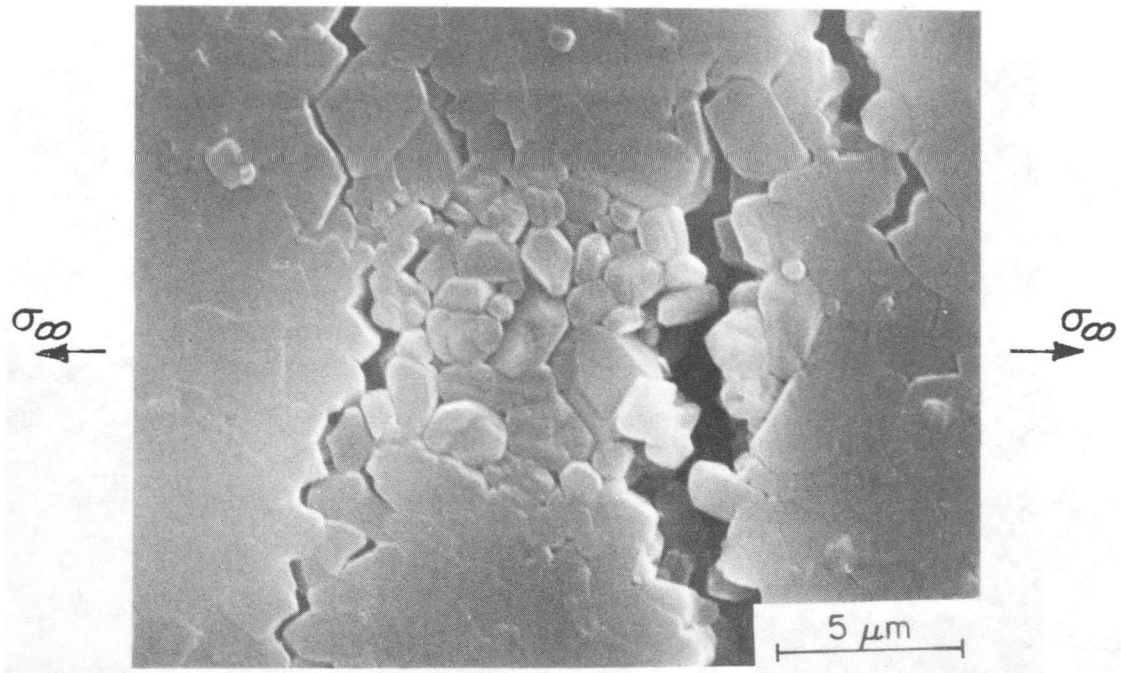

XBB 825-4694A

Fig. 4.19

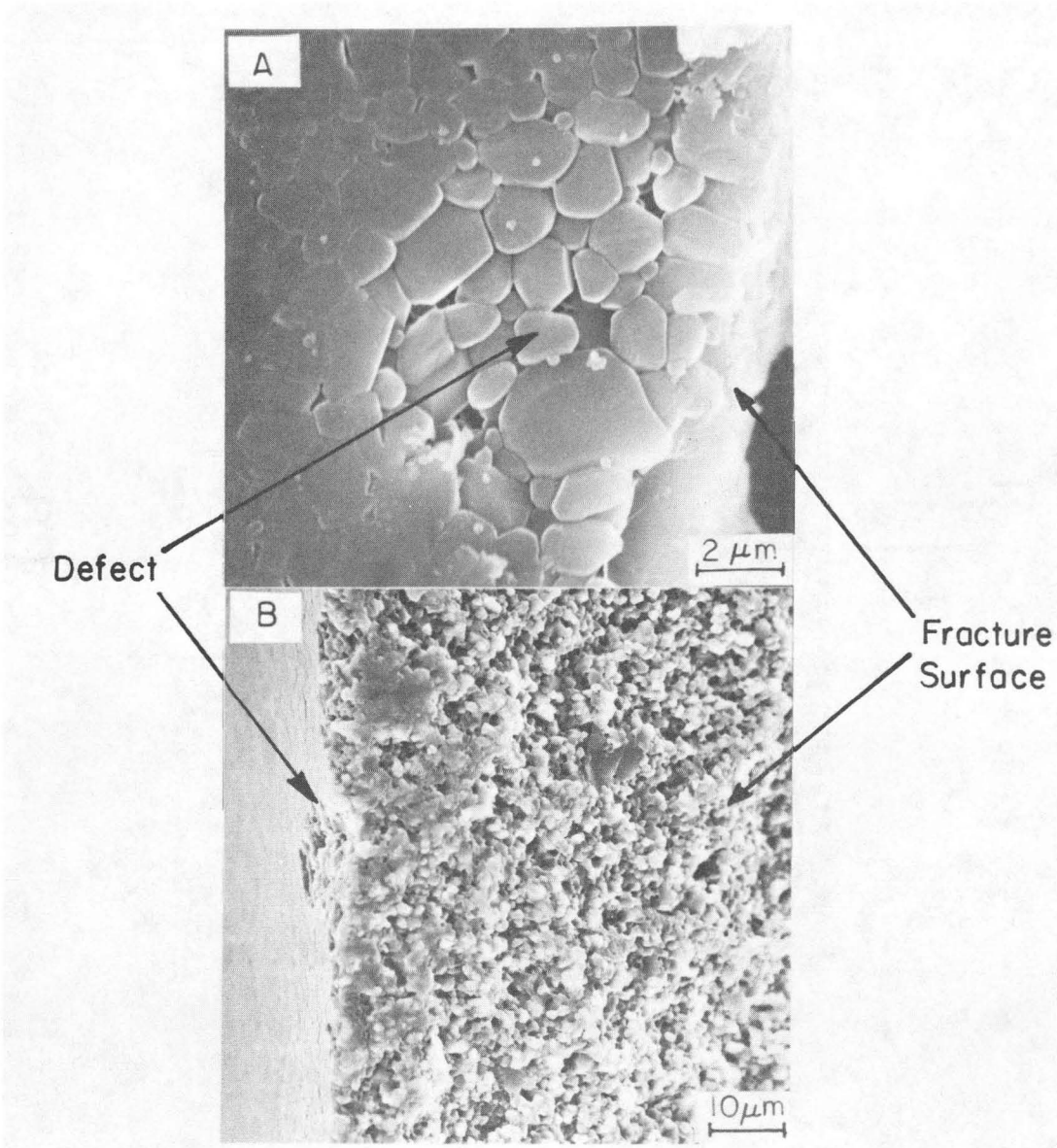

Fig. 4.20

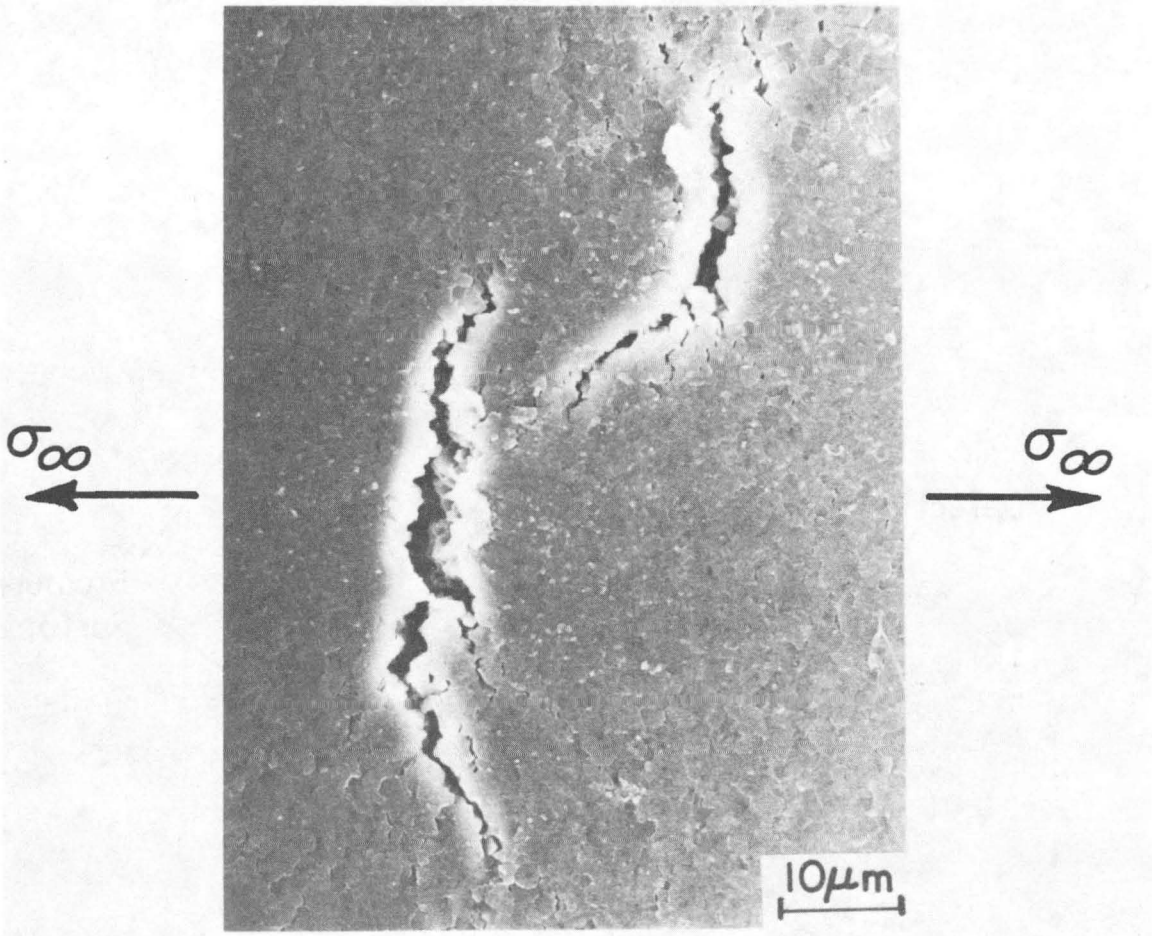

XBB 824-2981A

Fig. 4.21

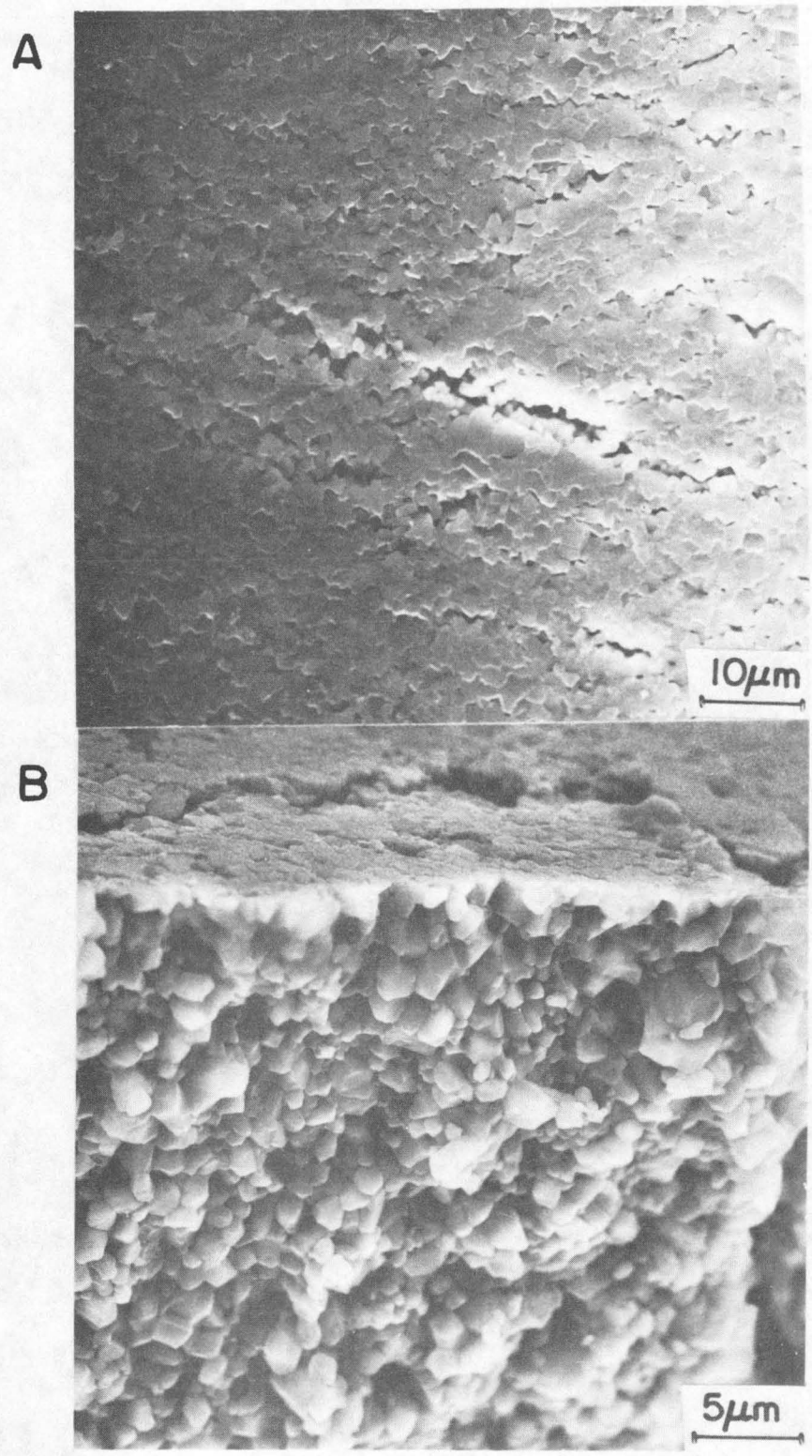

XBB 829-7715

Fig. 4.22

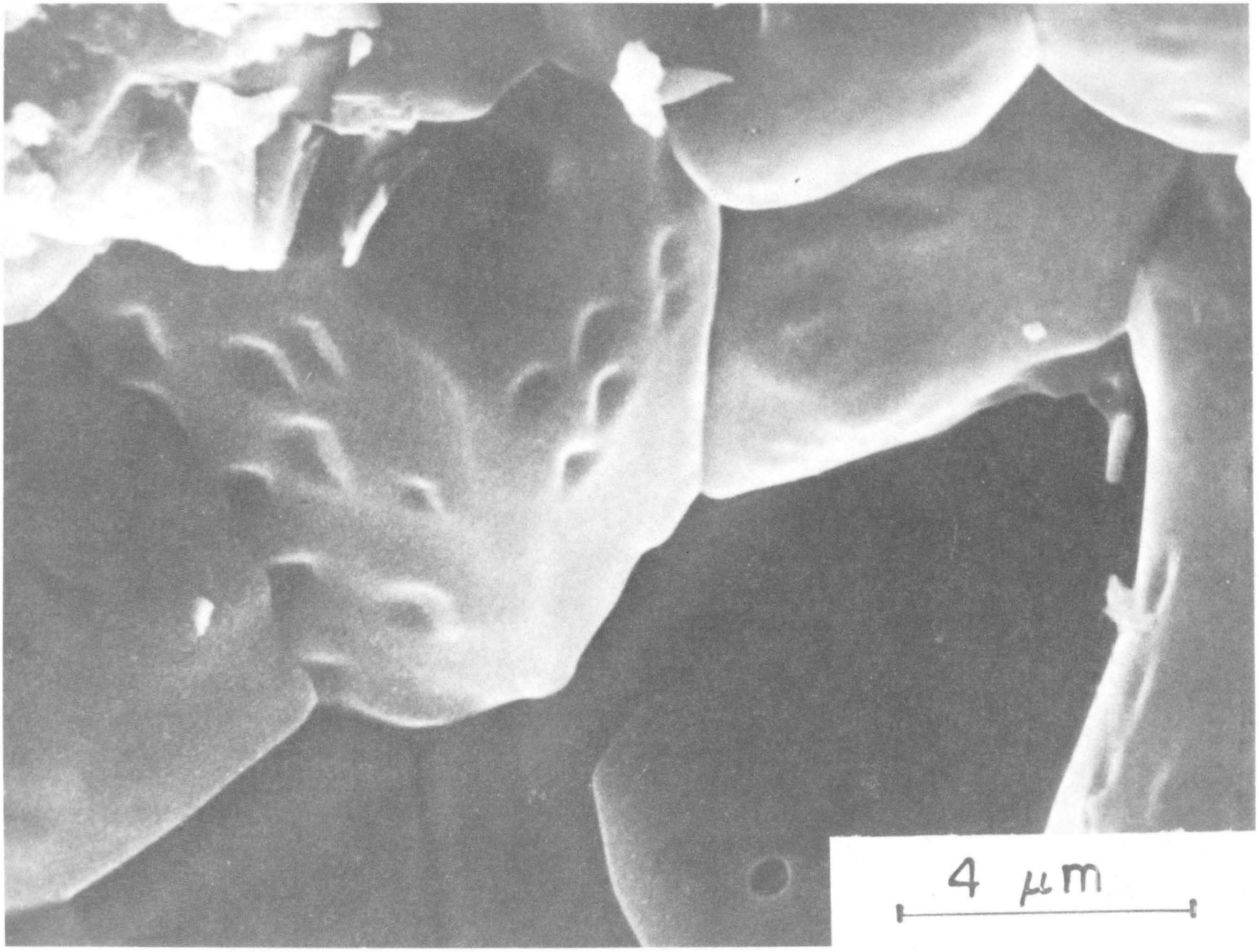

XBB813-2342

Fig. 4.23

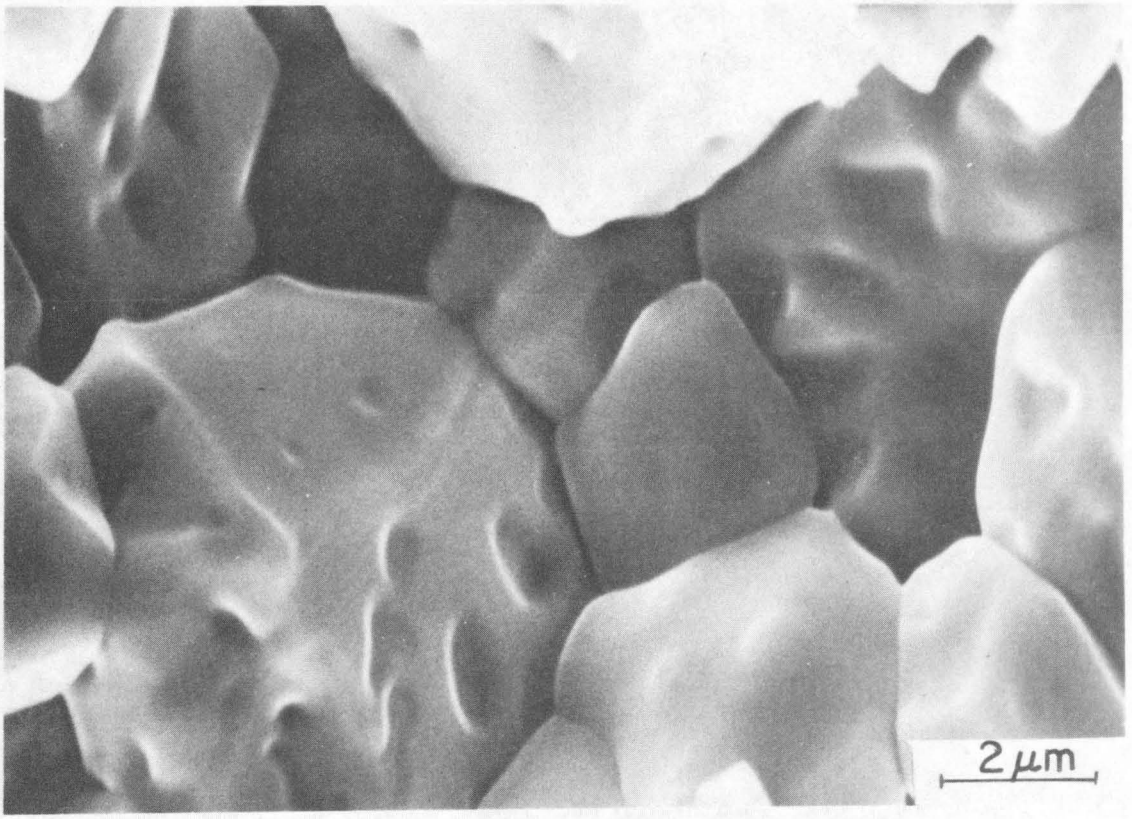

XBB 813-2548

Fig. 4.24

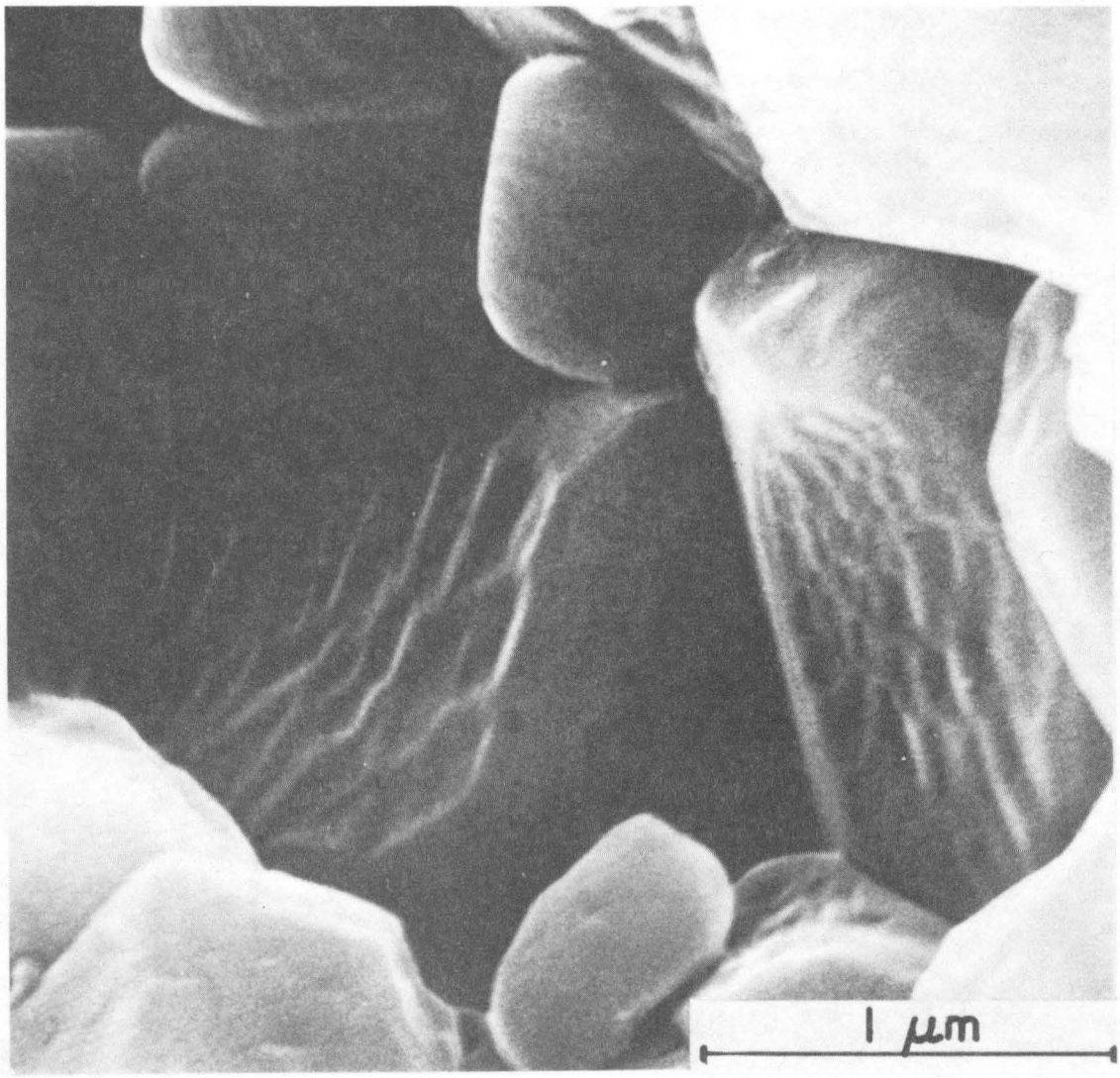

XBB 824-2934A

Fig. 4.25

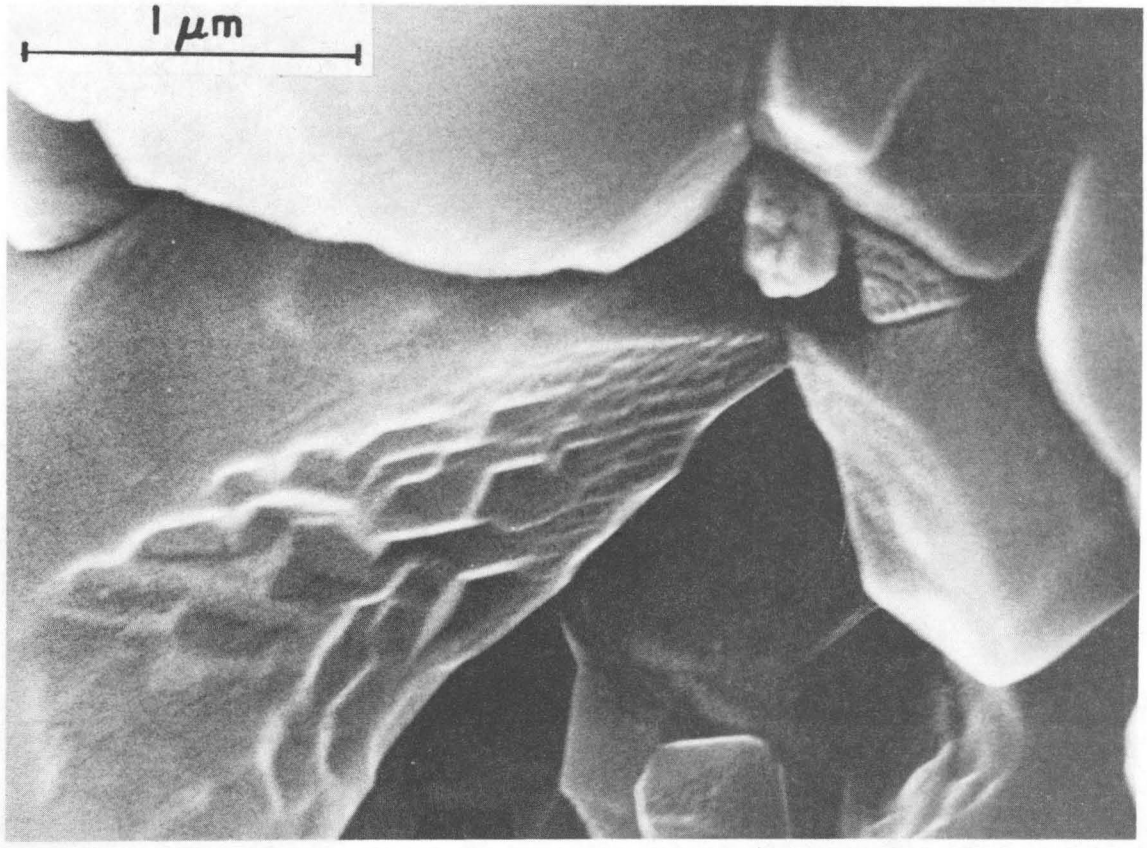

XBB 824-2932A

Fig. 4.26

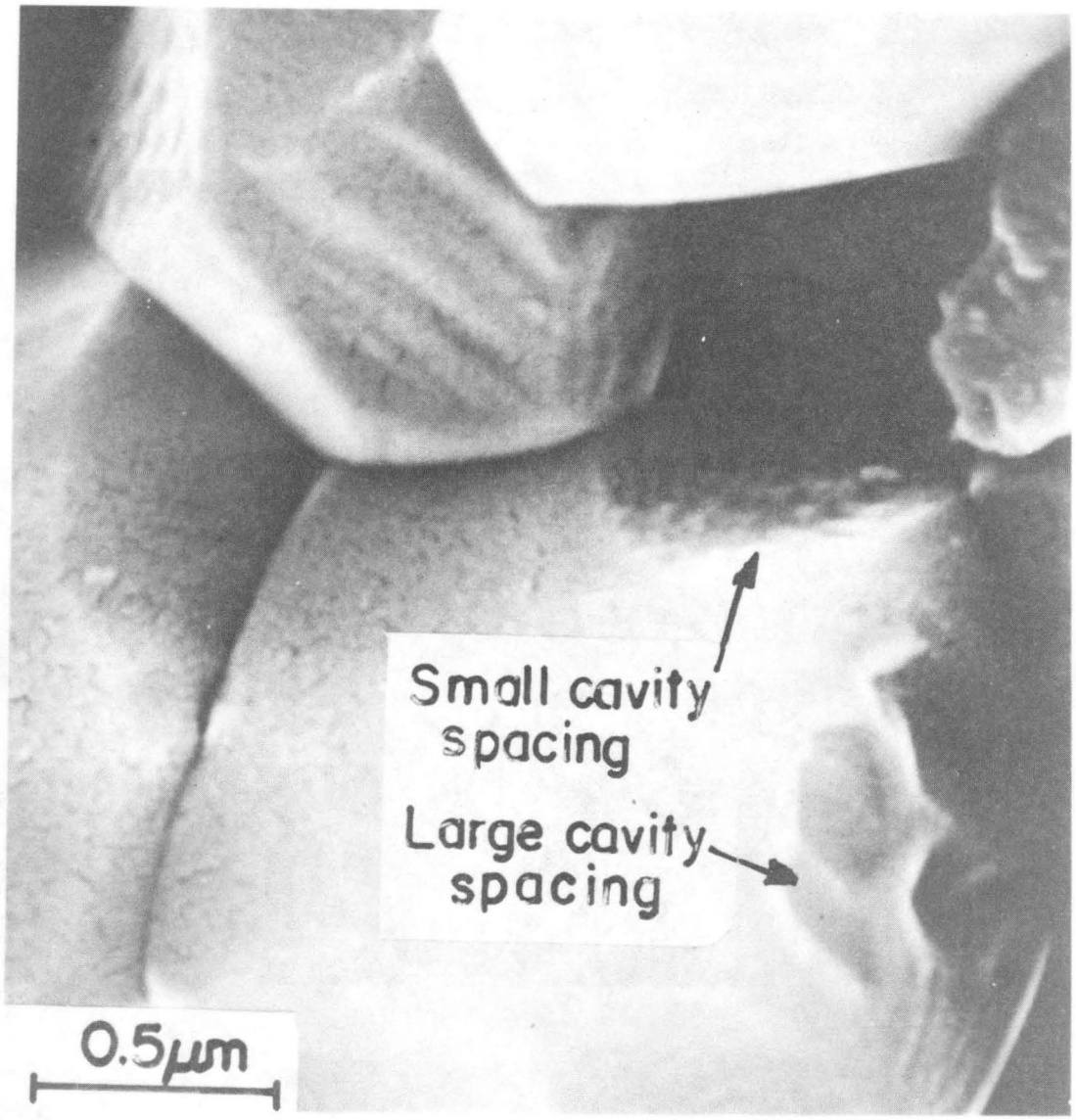

XBB 824-2989B

Fig. 4.27

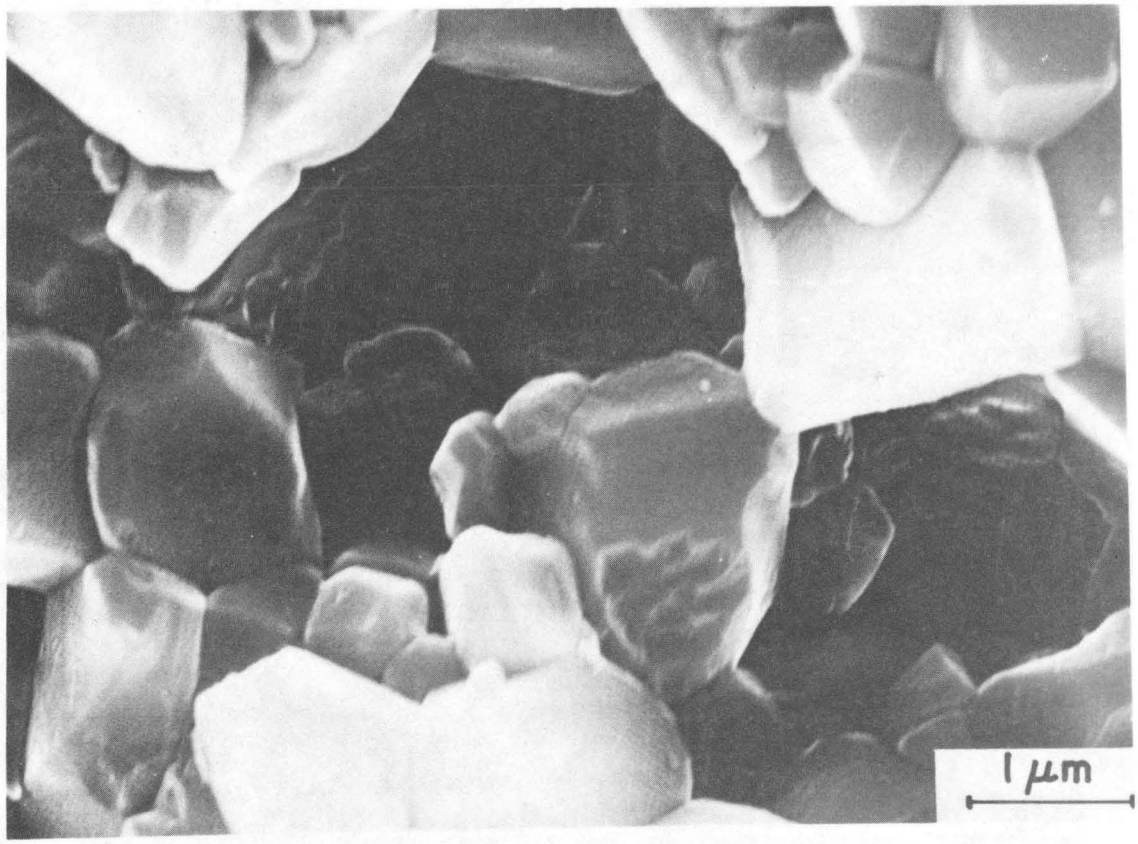

XBB 824-2922A

Fig. 4.28

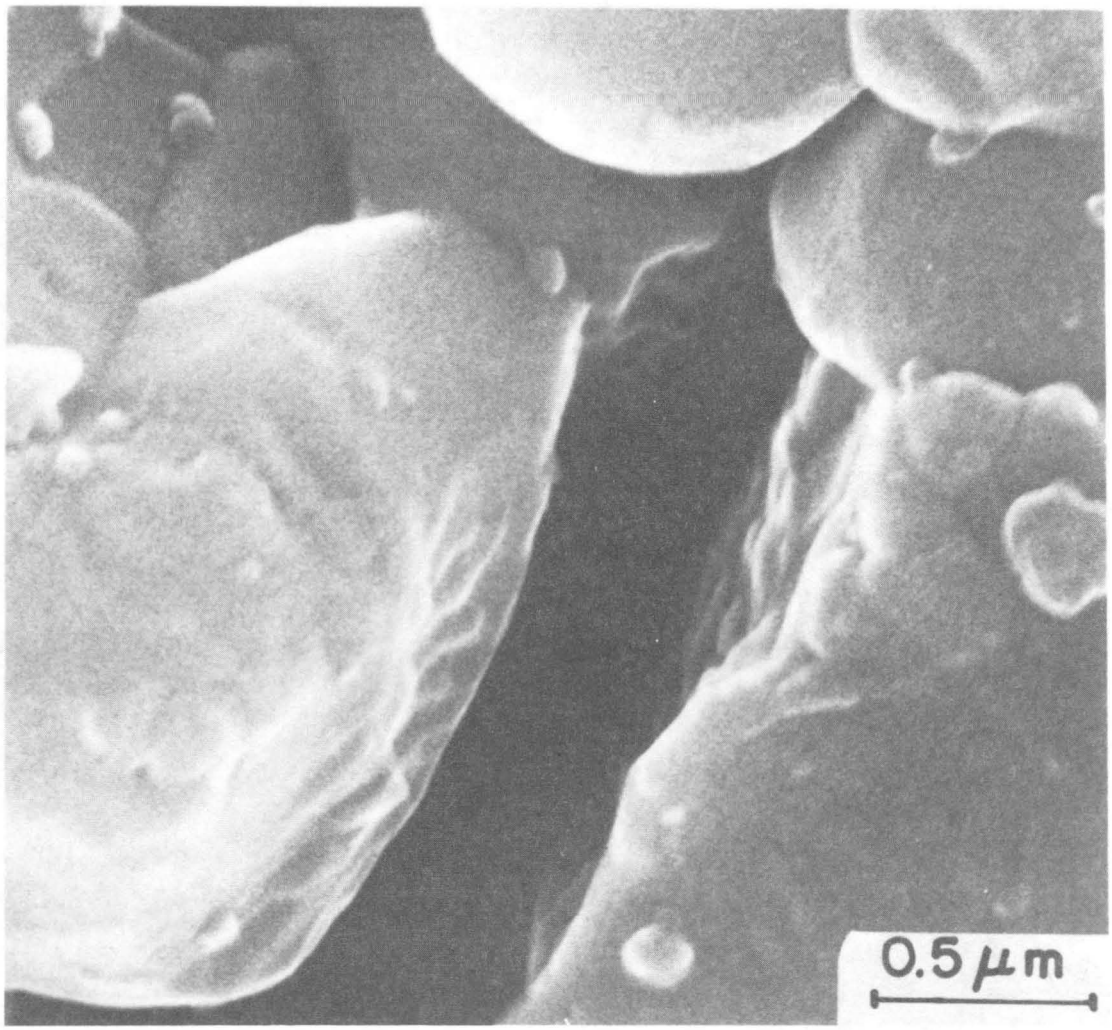

XBB 824-2950A

Fig. 4.29

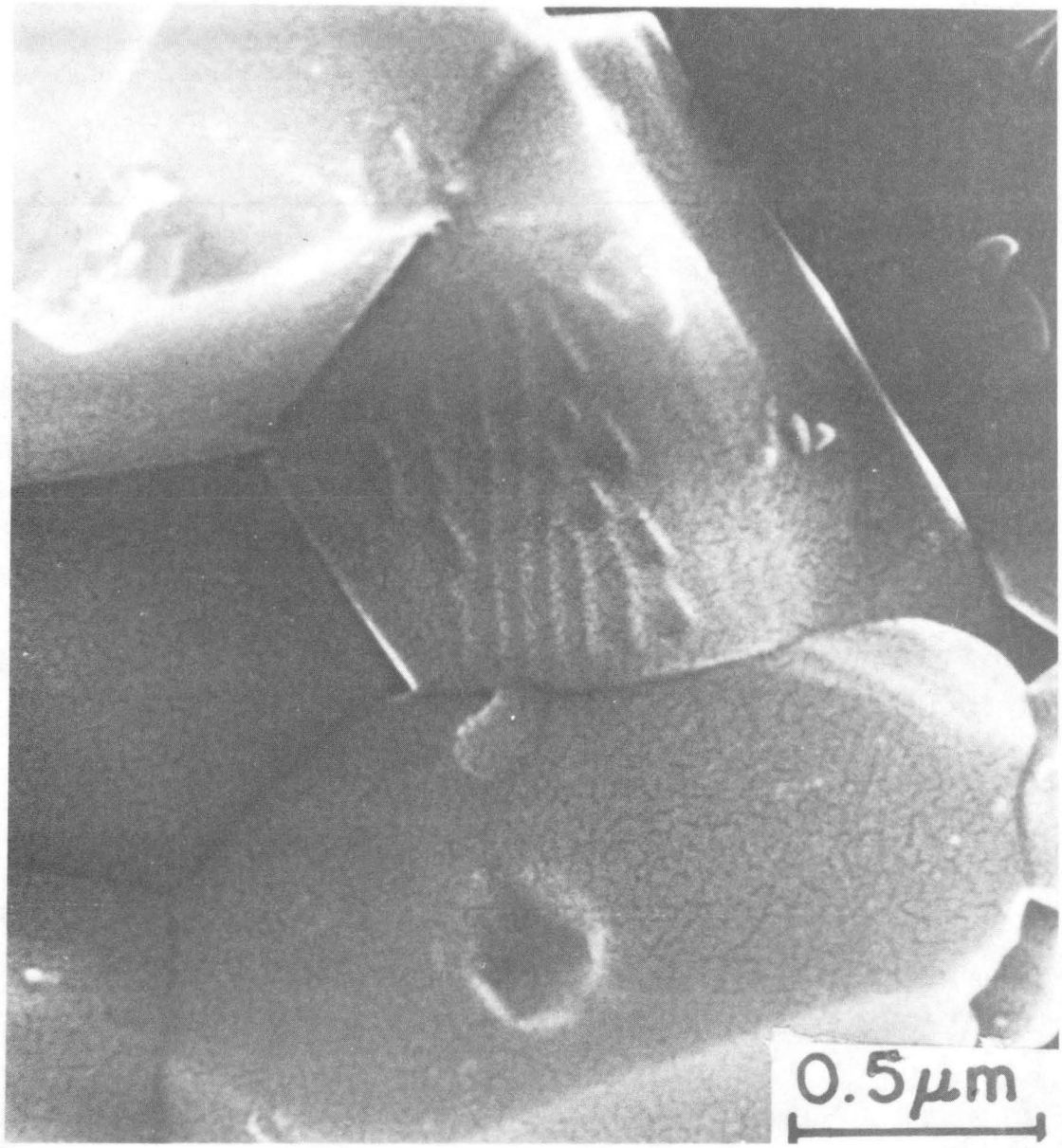

Fig. 4.30

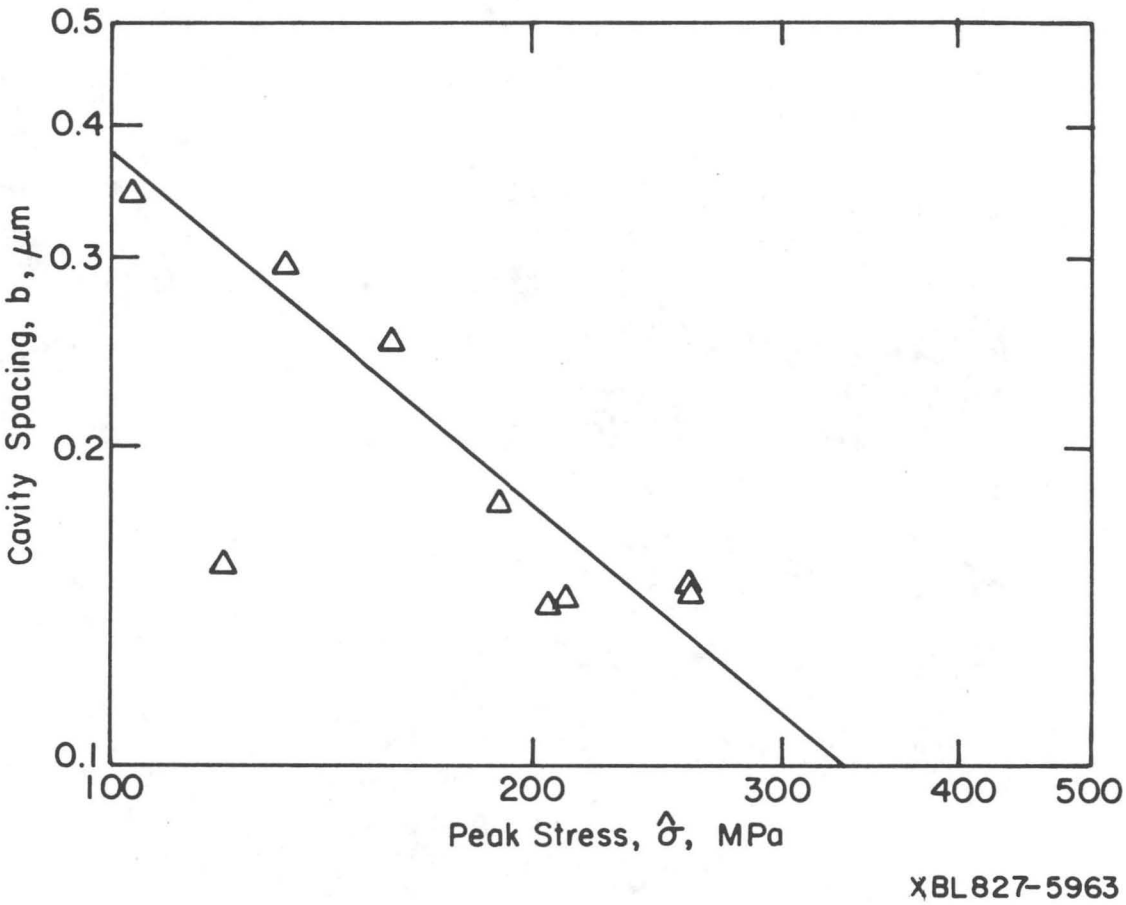
0.5
0.4
0.3
0.2
0.1
Cavity Spacing, b, μm
100
200
300
400
500
Peak Stress, σ̂, MPa
XBL827-5963

Fig. 4.31

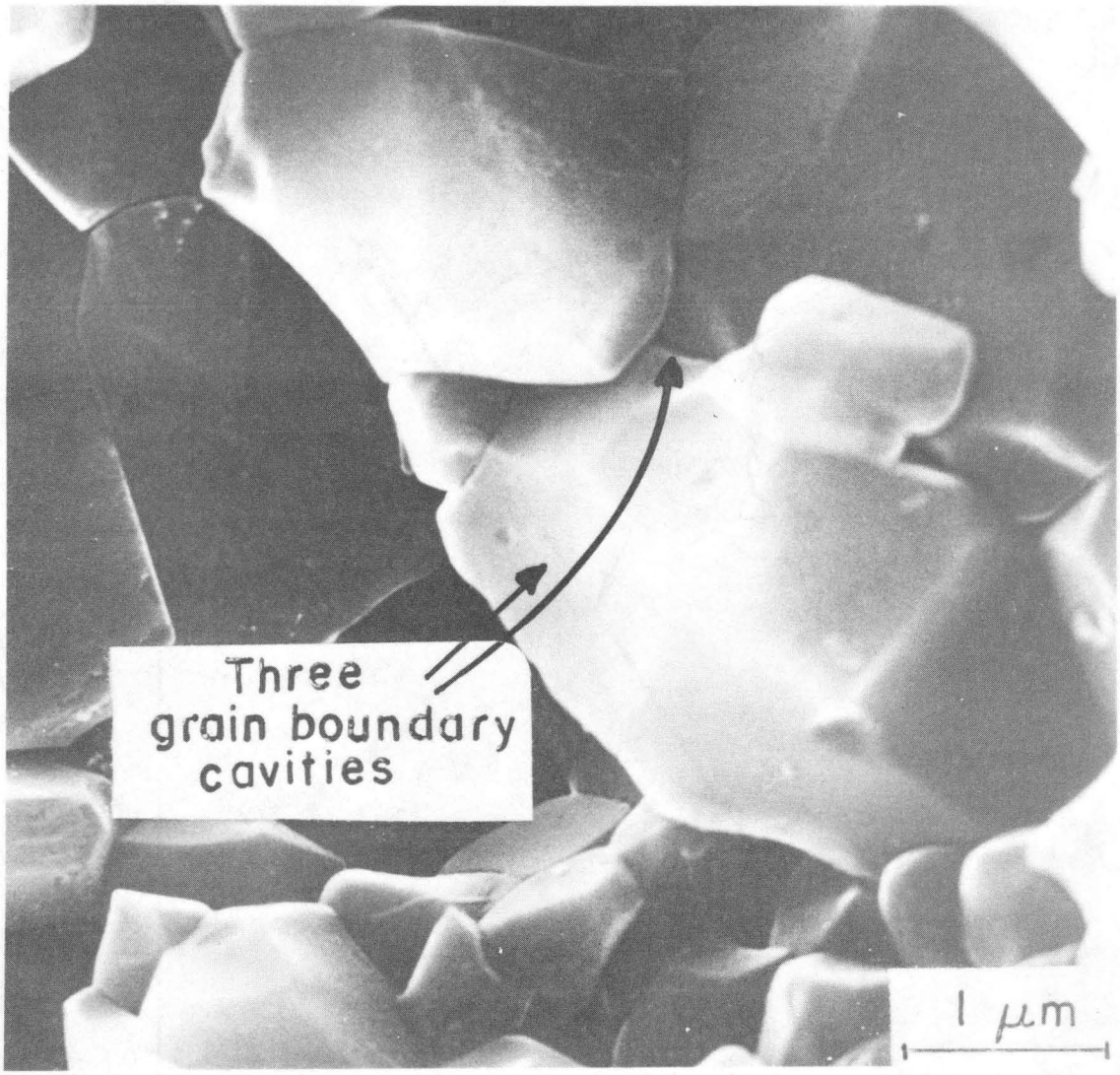

XBB 824-4020A

Fig. 4.32

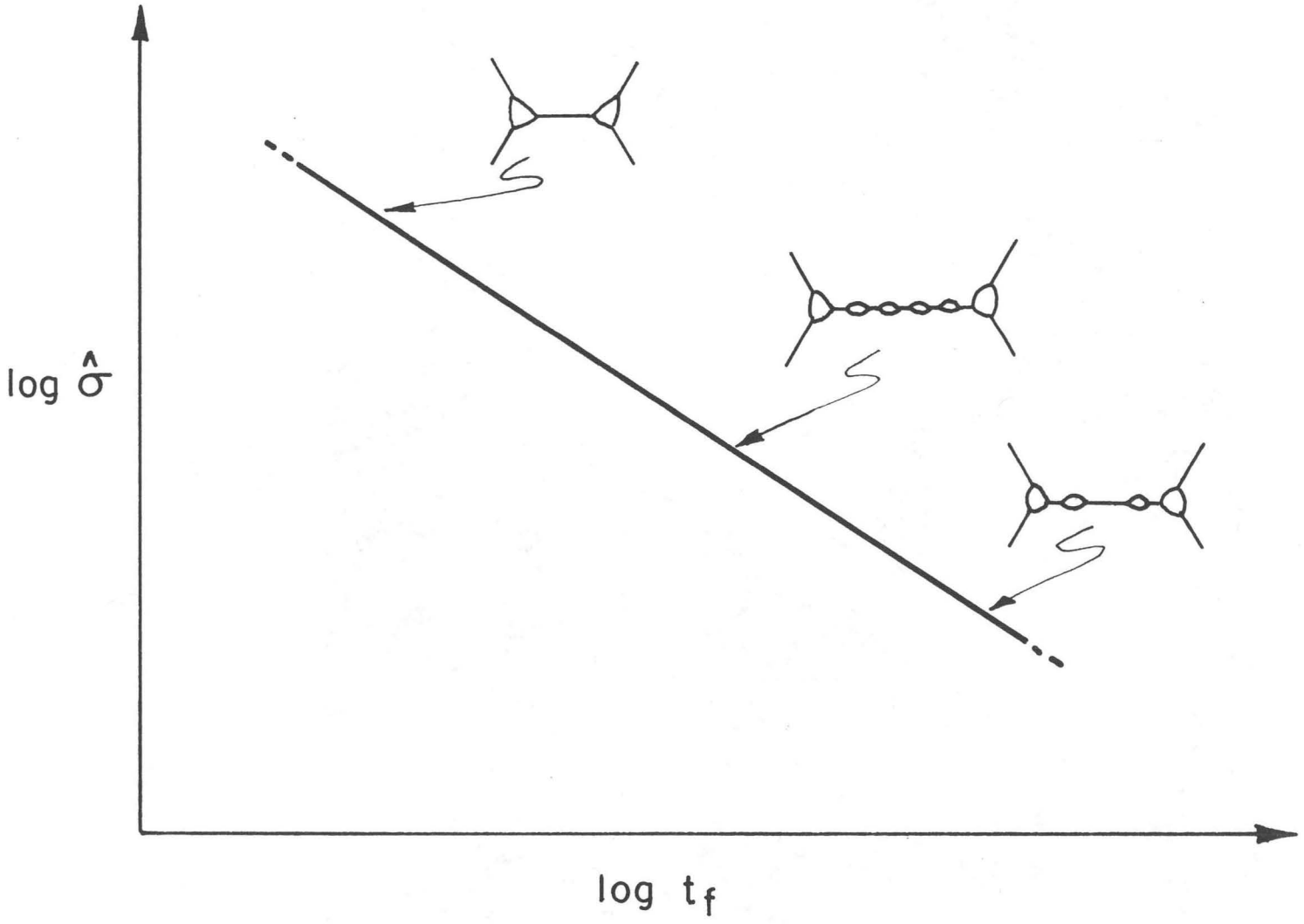

XBL824-5580

Fig. 4.33

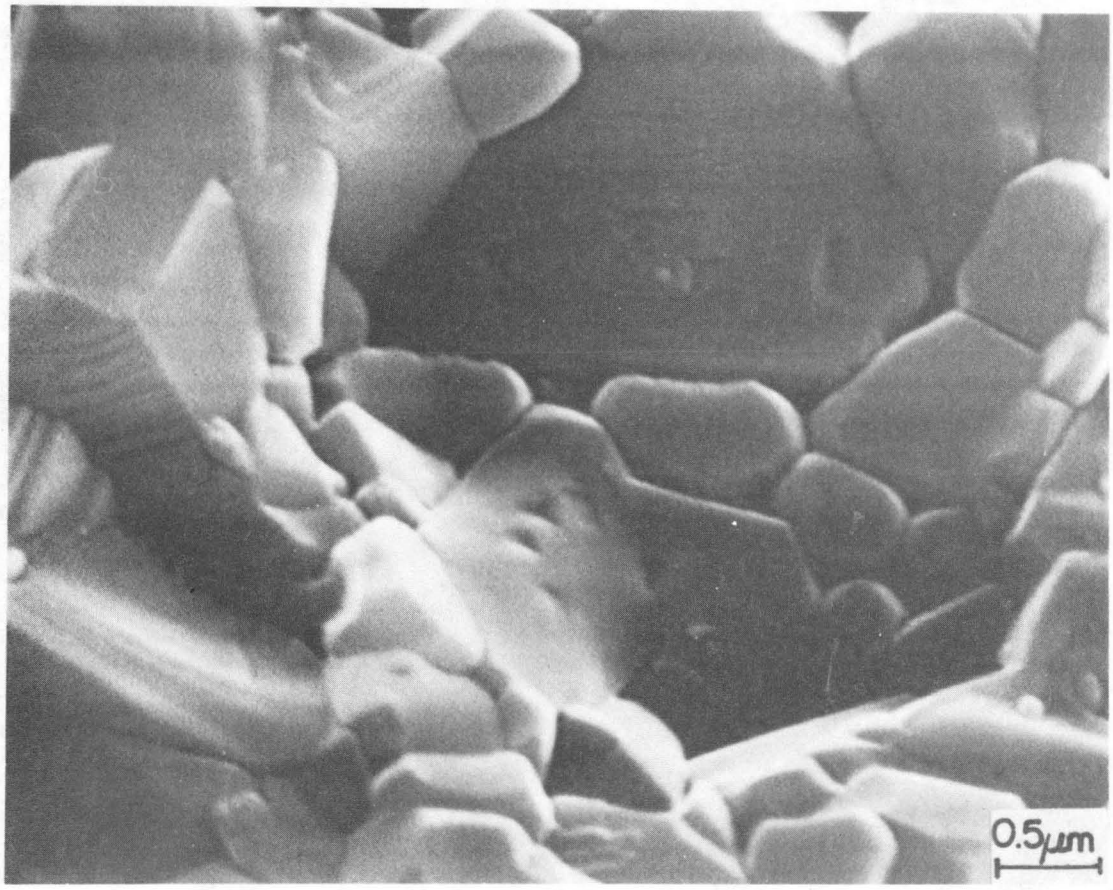

XBB 824-2959A

Fig. 4.34

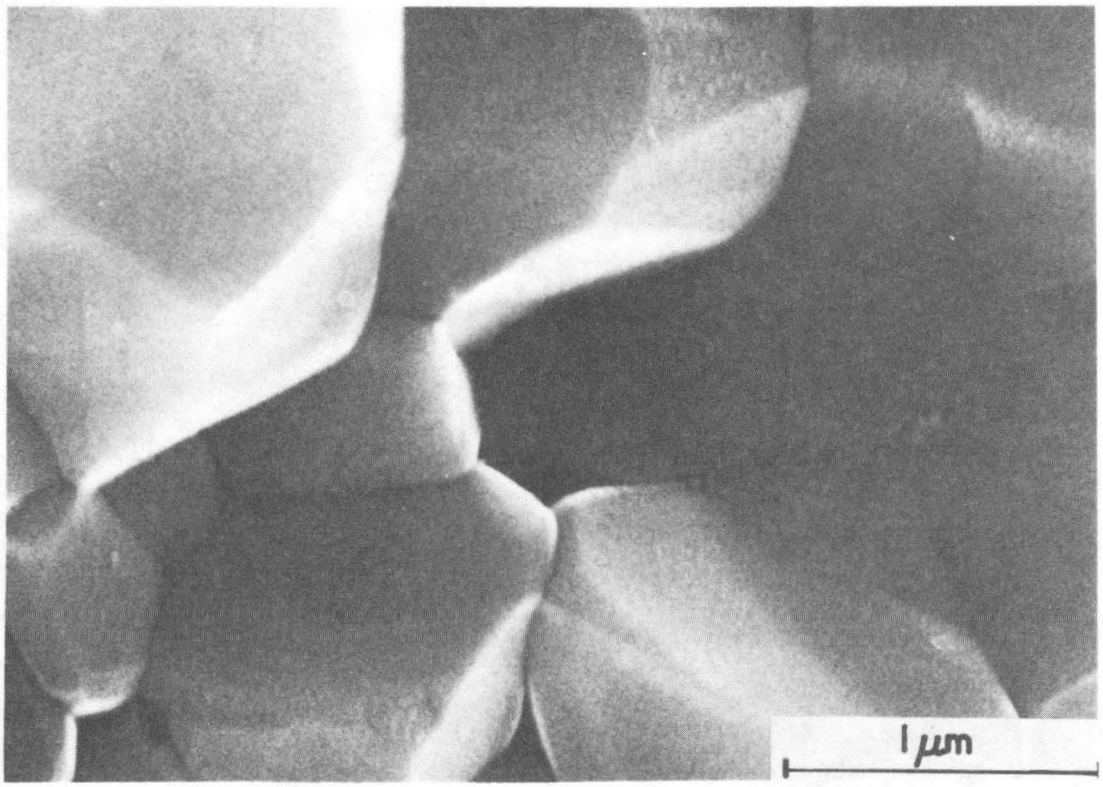

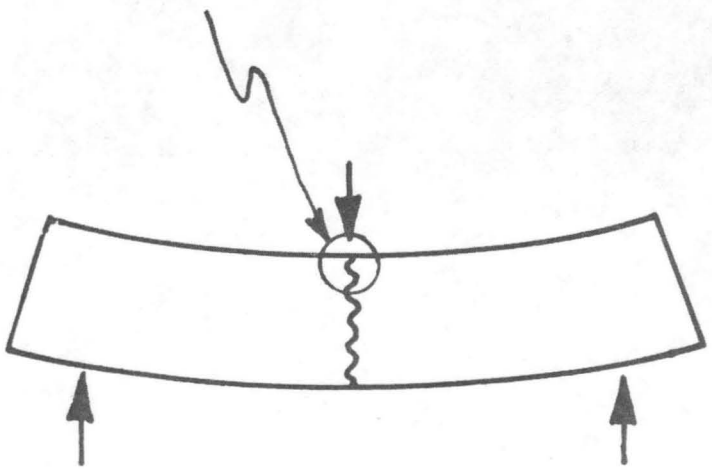

XBB 824-2966A

Fig. 4.35

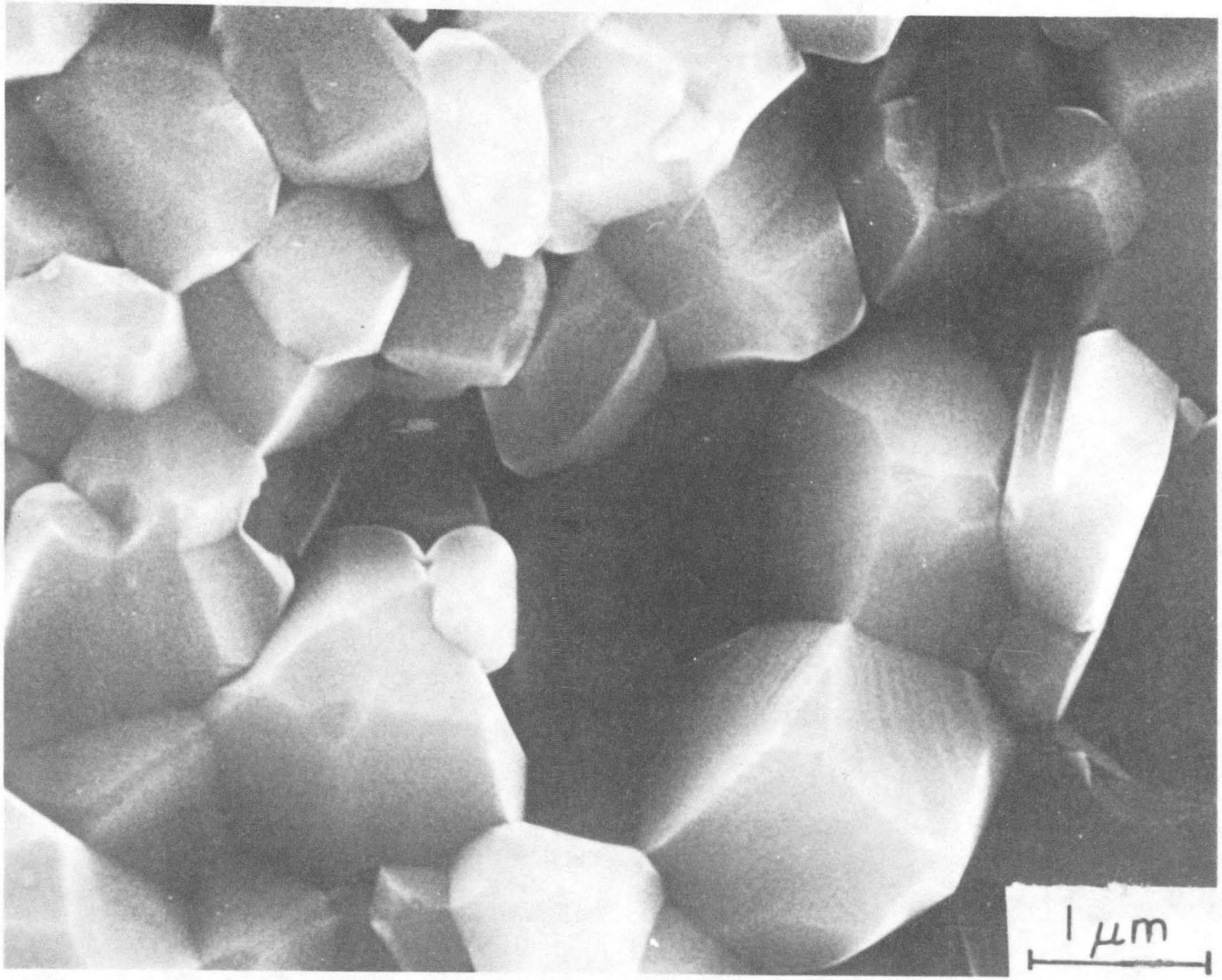

XBB 827-6046

Fig. 4.36

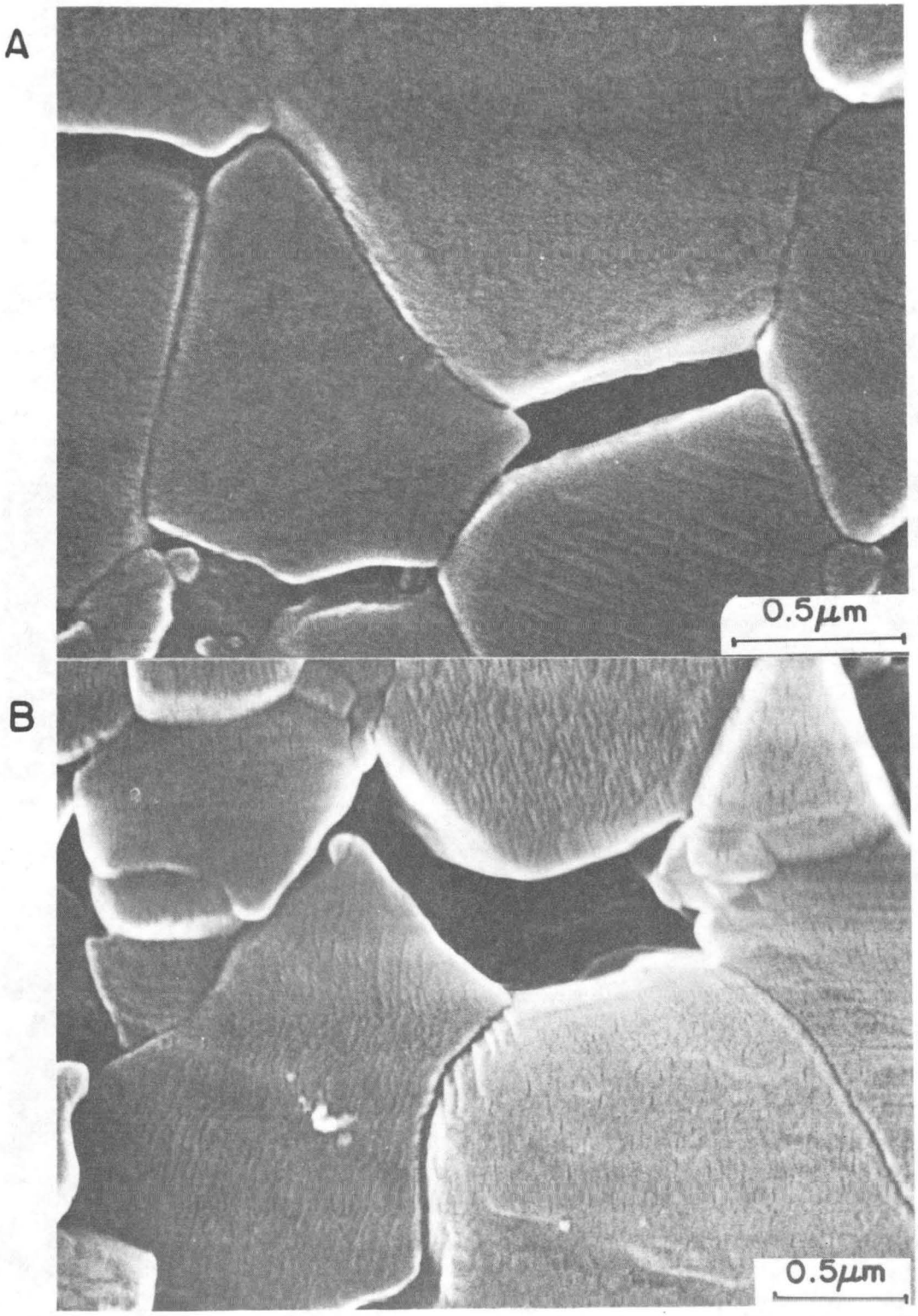

XBB 827-3300

Fig. 4.37

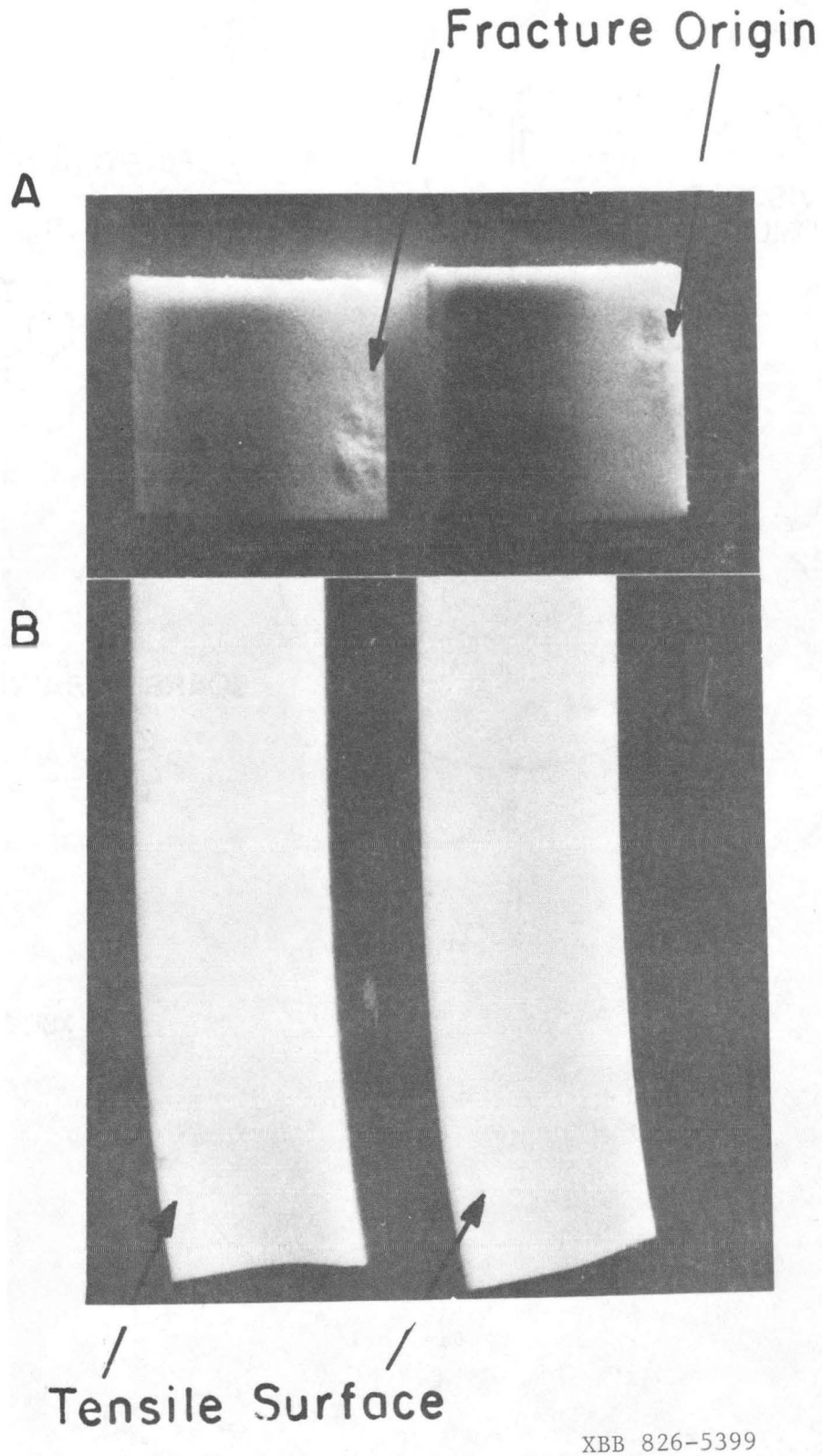

Fig. 4.38

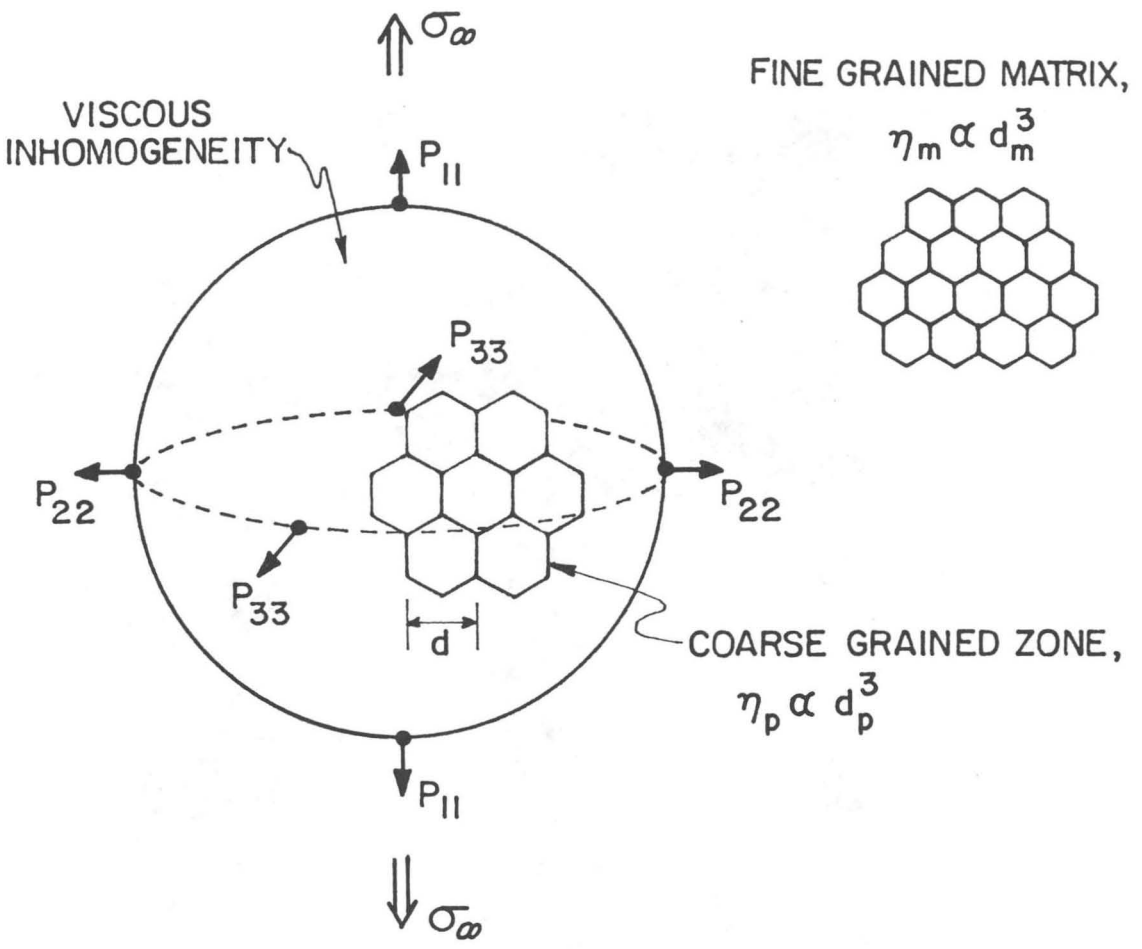
σ_∞
VISCOUS
INHOMOGENEITY
P_{11}
FINE GRAINED MATRIX,
$\eta_m \alpha d_m^3$
P_{33}
P_{22}
P_{22}
P_{33}
d
COARSE GRAINED ZONE,
$\eta_p \alpha d_p^3$
P_{11}
σ_∞
XBL 8112-12870

Fig. 5.1

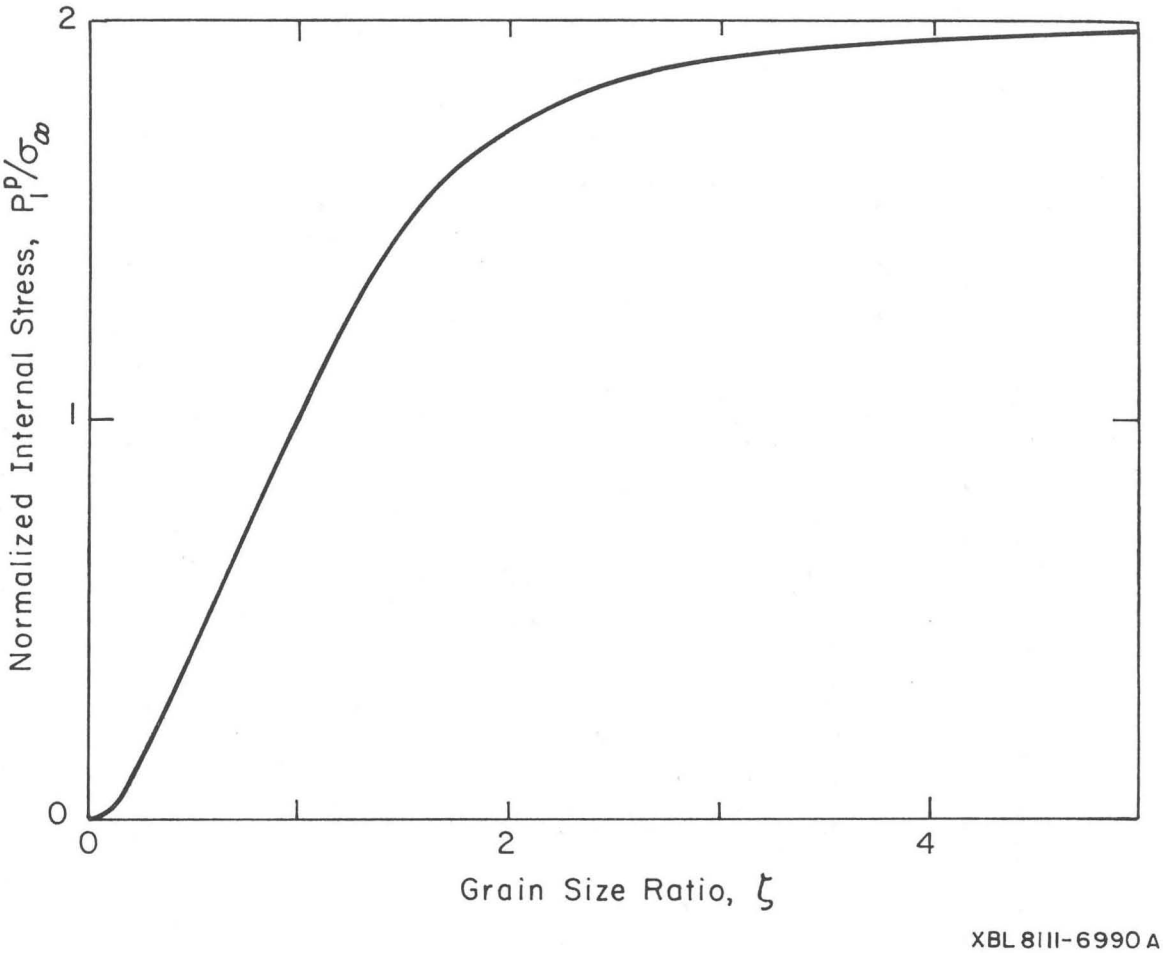
2
1
0
0
2
4
Normalized Internal Stress, P_1^p/σ_∞
Grain Size Ratio, ζ
XBL 8111-6990 A

Fig. 5.2

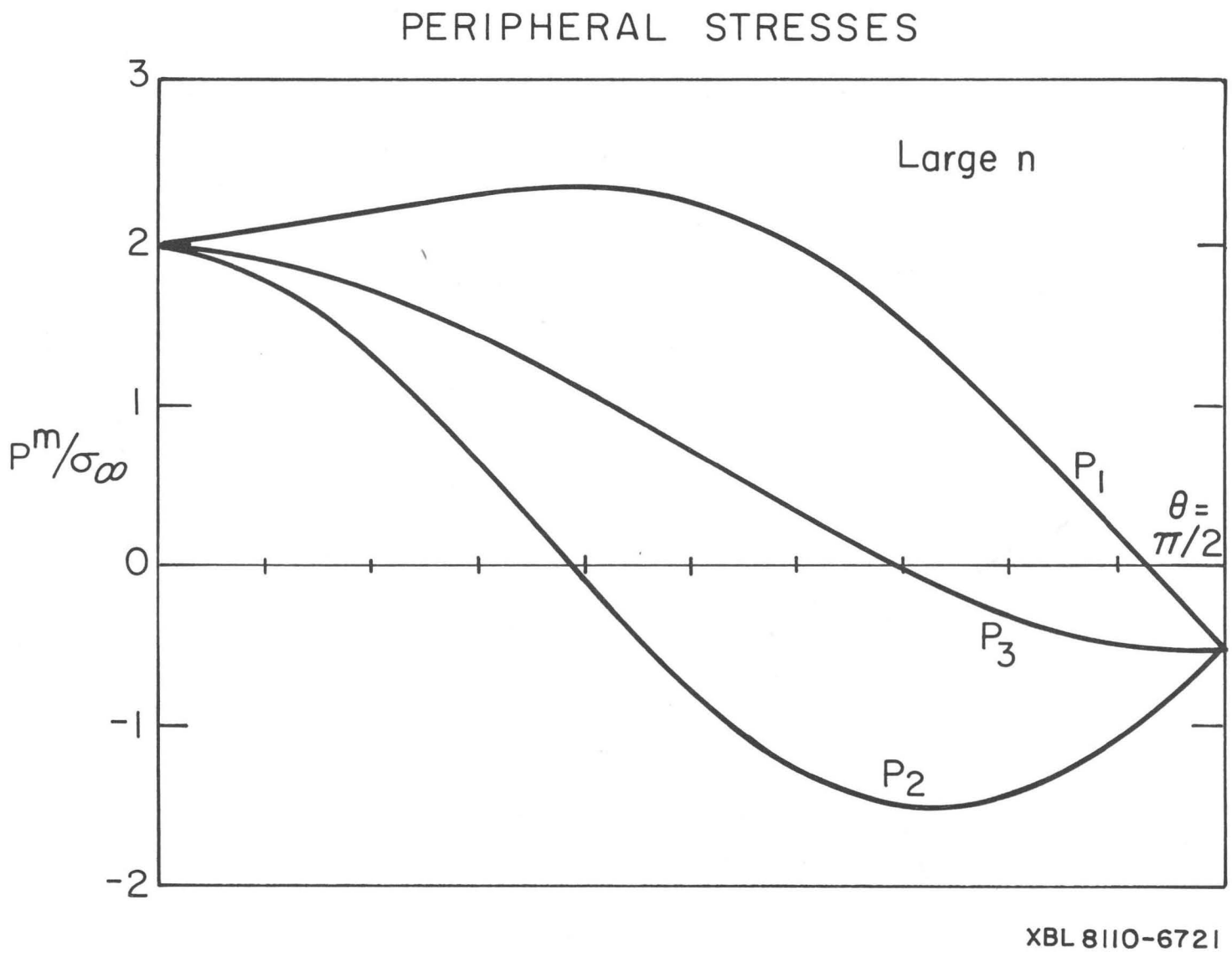
PERIPHERAL STRESSES
Large n
P^m/σ_∞
3
2
1
0
-1
-2
P_1
P_2
P_3
$\theta = \pi/2$
XBL 8110-6721

Fig. 5.3

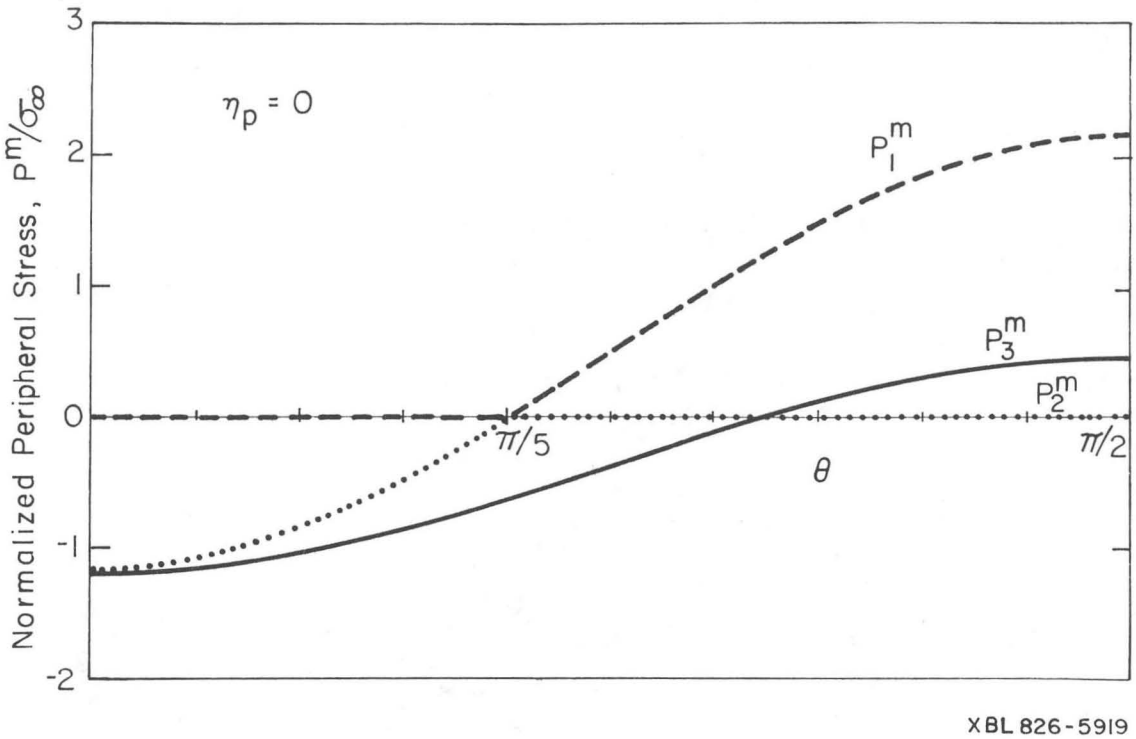
3
2
1
0
-1
-2
$\eta_p = 0$
P_1^m
P_3^m
P_2^m
$\pi/5$
$\pi/2$
θ
Normalized Peripheral Stress, P^m/σ_∞
XBL 826-5919

Fig. 5.4

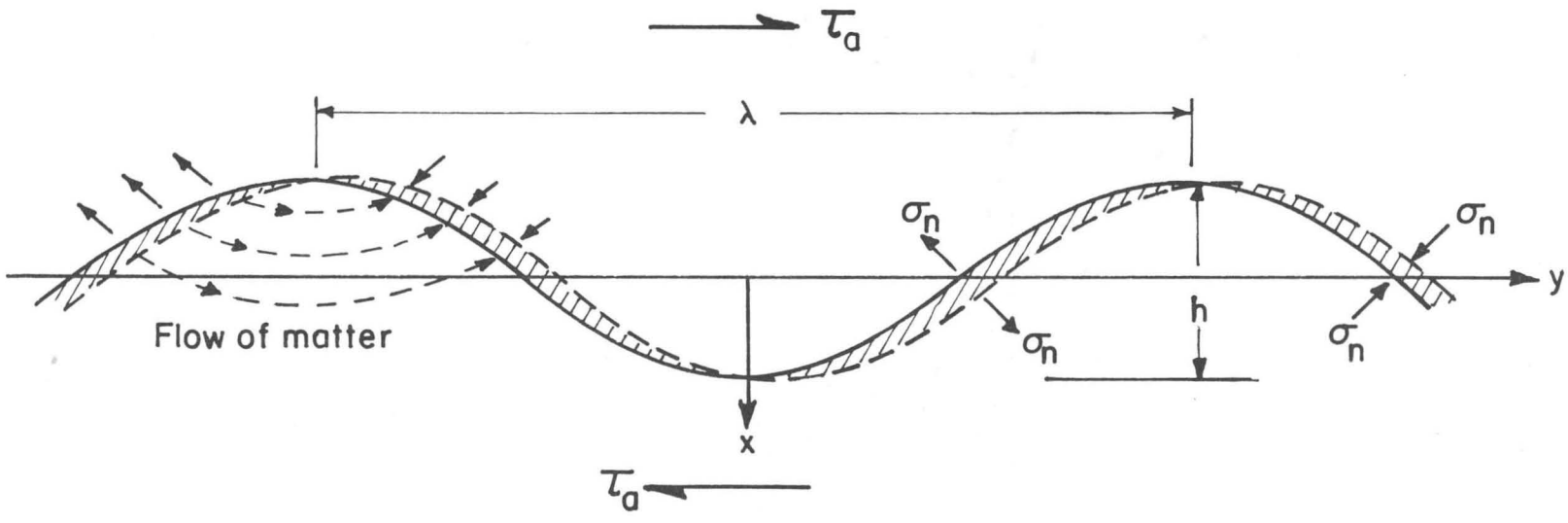

XBL 827-6045

Fig. 6.1

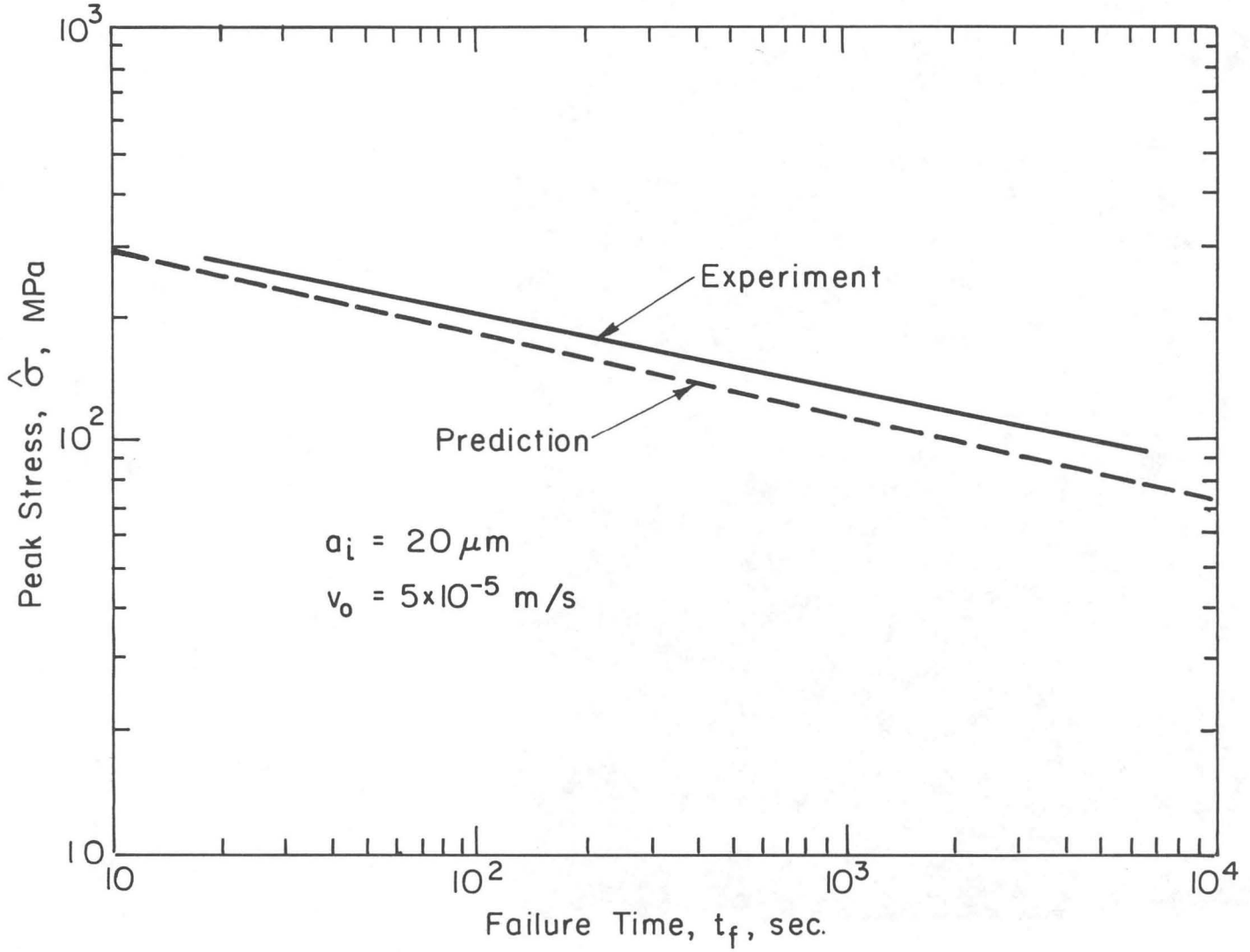

XBL 826-5957

Fig. 6.2

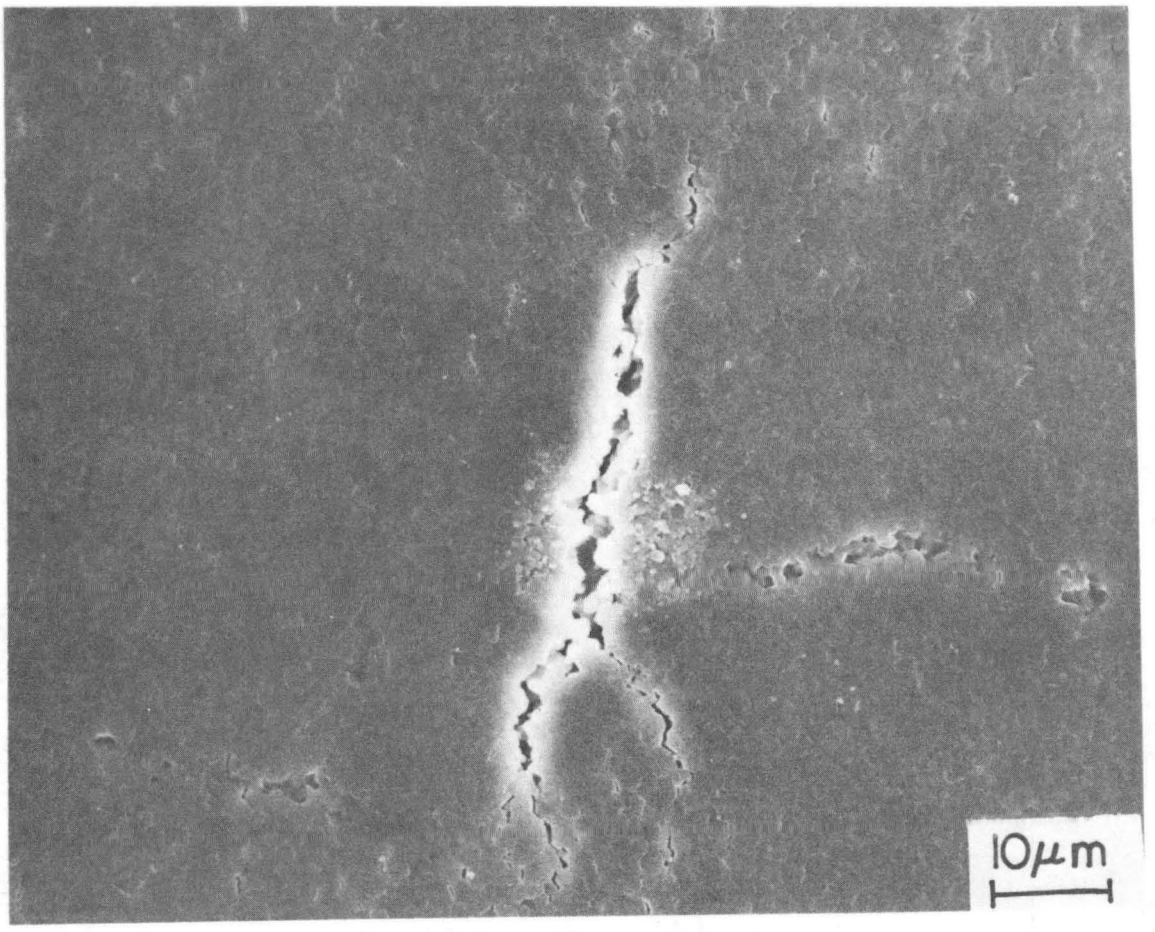

XBB 826-5402A

Fig. 6.3

This report was done with support from the Department of Energy. Any conclusions or opinions expressed in this report represent solely those of the author(s) and not necessarily those of The Regents of the University of California, the Lawrence Berkeley Laboratory or the Department of Energy.

Reference to a company or product name does not imply approval or recommendation of the product by the University of California or the U.S. Department of Energy to the exclusion of others that may be suitable.

TECHNICAL INFORMATION DEPARTMENT
LAWRENCE BERKELEY LABORATORY
UNIVERSITY OF CALIFORNIA
BERKELEY, CALIFORNIA 94720